Development and Application of Efficient Strategies for Parallel Magnetic Resonance Imaging

Dissertation zur Erlangung des

naturwissenschaftlichen Doktorgrades

der Bayerischen Julius-Maximilians-Universität Würzburg

vorgelegt von

Felix Breuer

aus Würzburg

Würzburg 2006

Contents

Chapter 1

Basics of MRI

1.1 Nuclear Magnetic Resonance

The phenomenon of Nuclear Magnetic Resonance (NMR) was first described by Bloch [1] and Purcell [2] in 1946. Simultaneously, but idependently they investigated the interaction between the non-zero magnetic moment of atomic nuclei and an external magnetic field. They found that whenever a nucleus with non-zero spin angular momentum is placed in a magnetic field, the energy level is forced to split into multiple levels. For spin 1/2- systems, such as ^1H, ^{13}C or ^{19}F the spin will seek to align itself either parallel or anti-parallel to the external field in accordance with the quantization of angular momentum, thereby creating two distinct energy levels. Spins precess around the main field with the so called Larmor frequency, which is given by:

$$\omega_0 = \gamma B_0 \tag{1.1}$$

B_0 is the field strength of the magnetic field, which in accordance to convention is applied in the z-direction, and the parameter γ is known as the gyromagnetic ratio, which has a characteristic value for each atomic nucleus. For protons the gyromagnetic ratio has value $\gamma/2\pi = 42.57\, MHz/T$ which corresponds to a resonance frequency of $\nu = \omega_0/2\pi = 63.86 MHz$ at $1.5\, T$. Because the spins parallel to the magnetic field have a slightly lower energy than those anti-parallel to the field, there will be slightly more parallel spins than anti-parallel. This difference in energy population leads to a net macroscopic magnetization. In order to achieve a detectable signal, the magnetization vector must be tipped from the static magnetic field direction, resulting in a changing flux in a nearby receiver coil. This can be accomplished by rotating the magnetization away from its alignment by applying an oscillating magnetic field B_1 perpendicular to the static magnetic field for a short time τ. This radio frequency (rf) pulse is produced by a transmit coil tuned to the Larmor frequency in order to match the resonance condition. The angle by which the magnetization is rotated away from the

z-direction by the rf-pulse is referred to as excitation angle or flip angle.

$$\alpha = \gamma \int_0^\tau |B_1(t)| \, dt \tag{1.2}$$

1.2 Relaxation

After the rf excitation pulse has been applied, part of the magnetization has been moved from the longitudinal axis to the transversal plane and therefore is no longer in thermal equilibrium. The time needed for the longitudinal magnetization to return to equilibrium is characterized by the relxation time constant T_1. This phenomenon is known as spin-lattice relaxation, because energy is transferred between the spin and the lattice to achieve equilibrium. Simultaneously, a second relaxation mechanism occurs. The transversal part of the magnetization decreases in time to zero, characterized by the relaxation time constant T_2. The reason for this phenomenon is that spins transfer energy among each other. Due to these interactions the phase coherence between the spins decreases in time resulting in a steady reduction of the net transversal magnetization. This relaxation process is known as transversal or spin-spin relaxation. In addition to the spin-spin interactions, further dephasing may occur due magnetic field inhomogeneties in the sample (T_2^* relaxation). The relaxation times T_1 and T_2 are characteristic for different tissues. Thus, signal from different tissues relax differently after rf excitation and in between subsequent rf excitations allowing one to influence image contrast.

1.3 Spatial Encoding

The precession frequency given in Eq. 1.1 can be modified by applying additional magnetic field gradients, thereby forcing the Larmor frequency to be spatially dependent. An additionally applied magnetic field gradient $\vec{G} = \nabla \vec{B} \approx \nabla B_z$[1] yields the following spatially dependent precession frequency ω:

$$\omega(\vec{r}, t) = \gamma \left(B_0 + \vec{G}(t) \cdot \vec{r} \right) \tag{1.3}$$

Thus, by exploiting magnetic field gradients in all three spatial dimensions, one is able to fully spatially encode the object under investigation. This procedure is known as Magnetic Resonance Imaging (MRI) and is described in more detail below.

1.3.1 Selective Excitation

At the beginning of every conventional 2D MRI experiment the slice to be imaged must be selected, normally in the z-direction. To this end, a selective rf excitation pulse is required,

---

[1]B_x and B_y can be neglected because $|\vec{B}_0| \gg |\vec{B}(\vec{r})|$

which excites only spins in a well defined frequency range. Such rf pulses have a well defined shape such as Gaussian or sinc with a finite frequency bandwidth $\Delta\omega_{rf}$ around the center frequency ω_{rf}. For small flip angles, the actual excitation profile of such pulses can roughly be approximated by a simple Fourier transformation of the temporal modulation function of the rf pulse (small tip angle approximation [3]). In this case, a sinc-type excitation pulse corresponds to a box-car-shaped excitation profile, a Gaussian rf pulse to a Gaussian excitation profile. By applying a frequency-selective rf pulse with frequency bandwidth $\Delta\omega_{rf}$ in combination with a constant magnetic field gradient $B_z = \frac{\partial B_z}{\partial z}$ only spins within a distinct slice with thickness Δz are excited.

$$\Delta z = \frac{\Delta\omega_{rf}}{\gamma \cdot G_z} \tag{1.4}$$

The slice position z_0 is adjusted by the carrier frequency ω_{rf} of the pulse, which can be chosen slightly off-resonant from the Larmor frequency given in Eq. 1.1. Exploiting again Eq. 1.3, the frequency offset corresponds to an offset in the slice position.

$$z_0 = \frac{\omega_{rf} - \omega_0}{\gamma \cdot G_z} \tag{1.5}$$

To compensate for spin dephasing caused by the slice gradient, an inverted gradient must be applied after slice-selection.

1.3.2 k-Space Formalism

According to Eq. 1.3 magnetic field gradients $\vec{G}(t)$ result in a spatially dependent Larmor frequency. In the presence of such a gradient, the signal $S(t)$ picked up by the receiver is composed of the sum of all spins in the object under investigation with spin density $\rho(\vec{r})$ (neglecting relaxation effects) at position $\vec{r}$:

$$\begin{aligned} S(t) &\propto \int \rho(\vec{r}) \cdot e^{i \int_0^t \omega(\vec{r},t')dt'} d^3\vec{r} \\ &\propto e^{i\omega_0 t} \int \rho(\vec{r}) \cdot e^{i\gamma \int_0^t \vec{G}(t')dt'\vec{r}} d^3\vec{r} \end{aligned} \tag{1.6}$$

By substituting $\vec{k} = \gamma \int_0^t \vec{G}(t')dt'$, where t denotes the time the magnetic field gradient is applied, and omitting the exponential term with spatially independent modulation frequency ω_0, the relation in Eq. 1.6 yields:

$$S(\vec{k}) \propto \int \rho(\vec{r}) \cdot e^{i\vec{k}\vec{r}} d^3\vec{r} \tag{1.7}$$

In this form, the received signal S can be recognized as the Fourier transformation of the spin density $\rho(\vec{r})$ at position $\vec{r}$. Therefore, the spin density (or the image) can be determined by

simply applying the inverse Fourier transformation to the received signal.

$$\rho(\vec{r}) \propto \int S(\vec{k}) \cdot e^{-i\vec{k}\vec{r}} d^3\vec{k} \tag{1.8}$$

By introducing the reciprocal space vector $\vec{k}$, the so-called k-space can be defined, which is spanned by three orthogonal k-vectors allowing a simple description of the spatial encoding used in MRI [4]. This concept, and how it is carried out in practice is described in the following sections and can be gleaned up in more detail for example in reference [5].

1.3.3 Frequency Encoding

After slice selection, one spatial dimension is encoded by a spatial frequency modulation, the so-called frequency encoding. Here, frequency encoding is carried out in the x-direction by applying a constant magnetic field gradient $G_x = \frac{\partial B_z}{\partial x}$, during data acquisition. The longer and stronger the gradient G_x is applied, the higher is the spatial frequency content in the received one-dimensional signal:

$$S(k_x) = \int \rho(x) \cdot e^{ik_x x} dx \qquad \text{with} \qquad k_x = \gamma G_x \cdot t_x \tag{1.9}$$

In practice, the signal is sampled at N_x discrete points in intervals of Δt_x while a constant gradient G_x is on. Thus, the discrete steps traversed in the k_x direction in k-space are $\Delta k_x = \gamma G_x \Delta t_x$. In most cases, frequency encoding is performed by starting at a maximum negative spatial frequency $-k_x^{max}$ and ending at a maximum positive spatial frequency $+k_x^{max}$. To obtain the echo maximum at $k_x = 0$, before the actual frequency encoding is carried out, the spins are dephased by applying a negative gradient in the x-direction (see Fig. 1.1).

1.3.4 Phase Encoding

The phase of the NMR signal can be used to encode a second spatial dimension, here the y-direction, within the excited slice. The so-called phase encoding is carried out between the slice excitation and the signal acquisition. To this end, a magnetic field gradient, the phase encoding gradient $G_y = \frac{\partial B_z}{\partial y}$, is applied in the y-direction (perpendicular to the x-direction) for a duration t_y, thereby generating sinusoidal modulations of the spin phases in the sample. Thereafter, all spins precess with the same frequency, but now with a spatially dependent phase:

$$\Phi(y) = \gamma G_y t_y y \tag{1.10}$$

This modulation persists throughout the following read-out procedure. In contrast to frequency encoding, the phase encoding process has to be repeated several times by changing either the gradient strength G_y or the phase encoding time t_y in order to cover the entire
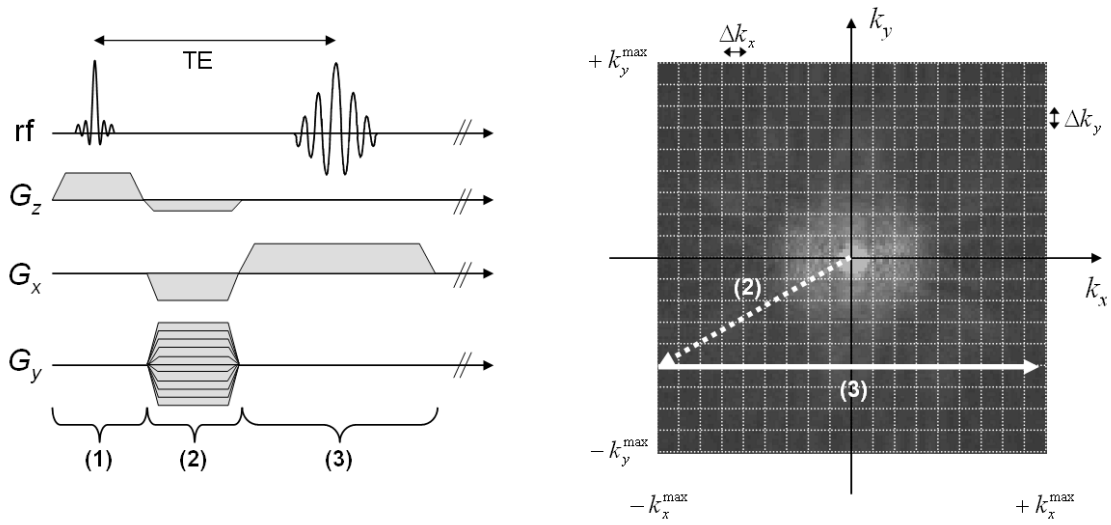
Figure 1.1: Schematic description of spatial encoding in MRI. On the left, a typical spin-warp gradient echo pulse sequence is displayed, and on the right, the corresponding k-space trajectory. In step (1), the slice selection is carried out by an rf excitation applied during a normally constant gradient in z-direction. In step (2), the rephase lobe of the slice select gradient is applied. Normally at the same time, a negative gradient lobe in x is switched, moving the trajectory in k-space to $-k_x^{max}$. Simultaneously, a phase encoding gradient applied in the y-direction moves the trajectory to a specific k_y-value. The actual read-out procedure (3) follows, which corresponds to travelling in the k_x-direction in k-space from left to right.

two dimensional k-space. With $k_y = \gamma G_y t_y$, the two-dimensional signal originating from the excited slice can be written as

$$S(k_x, k_y) = \int \rho(x, y) \cdot e^{i(k_x x + k_y y)} dx dy \qquad (1.11)$$

In Fig. 1.1 (left), the sequence of rf and gradient pulses are shown for a simple gradient echo experiment using a conventional spin-warp trajectory for phase encoding [6]. After slice selection (1) the starting point for the read-out procedure is set by applying a negative gradient in the x-direction and (normally at the same time) a phase encoding gradient in the y-direction (2), followed by the actual read-out procedure (3). This corresponds to moving at a certain k_y position in k-space in the k_x-direction from left $(-k_x^{max})$ to right $(+k_x^{max})$. This procedure must be repeated with multiple phase encoding gradients running from $-G_y^{max}$ to $+G_y^{max}$ in N_y equidistant steps to cover the entire k-space in the k_y-direction.

$$\Delta k_x = \gamma \frac{G_x t_x}{N_x} = \gamma G_x \Delta t_x \qquad \Delta k_y = \gamma \frac{2G_y^{max} t_y}{N_y} = \gamma \Delta G_y t_y \qquad (1.12)$$

The concept of phase encoding can be extended to the remaining third dimension instead of using slice selection. By applying an additional phase encoding gradient G_z in the z-direction, the signal originating from the excited slab can be spatially encoded in the slice direction. To

this end, a relatively thick slab is excited and encoded in multiple thin partitions.

$$
\begin{aligned}
S(k_x, k_y, k_z) &= \int \rho(x, y, z) \cdot e^{i(k_x x + k_y y + k_z z)} dx dy dz \\
\rho(x, y, z) &= \int S(k_x, k_y, k_z) \cdot e^{-i(k_x x + k_y y + k_z z)} dk_x dk_y dk_z
\end{aligned}
\tag{1.13}
$$

1.4 Sampling k-Space

Although there are alternative strategies which cover k-space in non-uniform steps such as spiral [7] or radial [8] trajectories, the focus in this work is aimed at trajectories with equidistant k-space steps as already depicted in Fig. 1.1. In these cases, the continuous Fourier transform given in Eq. 1.7 and Eq. 1.8 must be replaced by the discrete Fourier transform. Although it is not possible to collect an infinite amount of data points, it is instructive to first discuss the effect of infinite discrete sampling before, in a subsequent action, the impact of finite sampling is addressed.

1.4.1 Infinite Sampling

The MRI spectrometer collects the signal in descrete steps and not contineously. Instead, a finite number of data points are collected to cover the k-space. Such sampling is achieved by taking data at equidistant k- intervals Δk. Considering for the time being only one dimension, the measured signal is $S(m\Delta k)$ at the m'th step in discrete k-space. The discrete, but infinite, sampled signal $S_\infty(k)$ can be expressed mathematically by a multiplication of the continuous signal $S(k)$ with the infinite sampling function $f_\infty(k) = \Delta k \sum_{m=-\infty}^{+\infty} \delta(k - m\Delta k)$, representing an infinite series of evenly spaced Dirac delta functions.

$$
S_\infty(k) = S(k) \cdot f_\infty(k) = \Delta k \sum_{m=-\infty}^{+\infty} S(k) \cdot \delta(k - m\Delta k)
\tag{1.14}
$$

The inverse Fourier transformation of the infinitely sampled signal $S_\infty(k)$ gives only an approximation of the physical spin density $\rho(r)$, where r denotes an arbitrary spatial dimension.

$$
\hat{\rho}_\infty(r) = \int_{-\infty}^{+\infty} S_\infty(k) \cdot e^{ikr} dk = \Delta k \sum_{m=-\infty}^{+\infty} S(m\Delta k) \cdot e^{im\Delta k r}
\tag{1.15}
$$

An examination of equation Eq. 1.15 leads to the conclusion that $\hat{\rho}_\infty(r) = \hat{\rho}_\infty(x - l\frac{2\pi}{\Delta k})$ for any negative and positive integer l, because the exponential term $exp(im\Delta k r)$ remains unchanged if $r \to r - l\frac{2\pi}{\Delta k}$. This property of discrete sampling can also be achieved by exploiting the well-known convolution theorem. The reconstructed image $\hat{\rho}_\infty(r)$ can be expressed as the convolution of the spin density $\rho(r)$ with a function $F_\infty(r)$, which is the inverse Fourier

transformation of the infinite sampling function $f_\infty(k)$

$$S_\infty(k) = S(k) \cdot f_\infty(k) \qquad \hat{\rho}_\infty(r) = \rho(r) \otimes F_\infty(r) \qquad (1.16)$$

The Fourier transformation of an infinite series of Dirac delta functions evenly spaced by Δk results likewise in an infinite series of delta functions, but evenly spaced at intervals of $\frac{2\pi}{\Delta k}$.

$$F_\infty(r) = \sum_{l=-\infty}^{+\infty} \delta(r - l\frac{2\pi}{\Delta k}) \qquad (1.17)$$

Thus, the approximated spin density $\hat{\rho}_\infty$ becomes

$$\hat{\rho}_\infty = \sum_{l=-\infty}^{+\infty} \rho(r - l\frac{2\pi}{\Delta k}). \qquad (1.18)$$

Accordingly, by sampling the data at discrete points, the approximated spin density is the periodic repetition of the actual spin density, evenly spaced at intervals of the so-called Field Of View $FOV = \frac{2\pi}{\Delta k}$. As long as

$$FOV > A \qquad \text{or} \qquad \Delta k < \frac{2\pi}{A} \qquad (1.19)$$

where A denotes the object size in one dimension, the replicates of ρ do not overlap (see Fig. 1.2). However, if the value of Δk is chosen to be too large, in other words, the FOV too small, the replications overlap to some extent, resulting in an image which differs significantly from the physical spin density. Eq. 1.19 is referred to as the Nyquist sampling criterion. Data sampled at a rate that lies below the Nyquist criterion result in folding or aliasing artifacts in the image domain.

1.4.2   Finite Sampling

Since the MRI signal must be acquired in a finite amount of time, the data set must be truncated in addition to being discrete. Thus, the actual sampling function $f(k)$ can be seen mathematically as a multiplication of the infinite sampling function $f_\infty(k)$ with a rectangular window function $w(k)$, which maintains only a total number of $N = 2n$ data points.

$$\hat{S}(k) = S(k) \cdot f_\infty(k) \cdot w(k) = \Delta k \sum_{m=-n}^{n-1} S(m\Delta k)\delta(k - m\Delta k) \qquad (1.20)$$
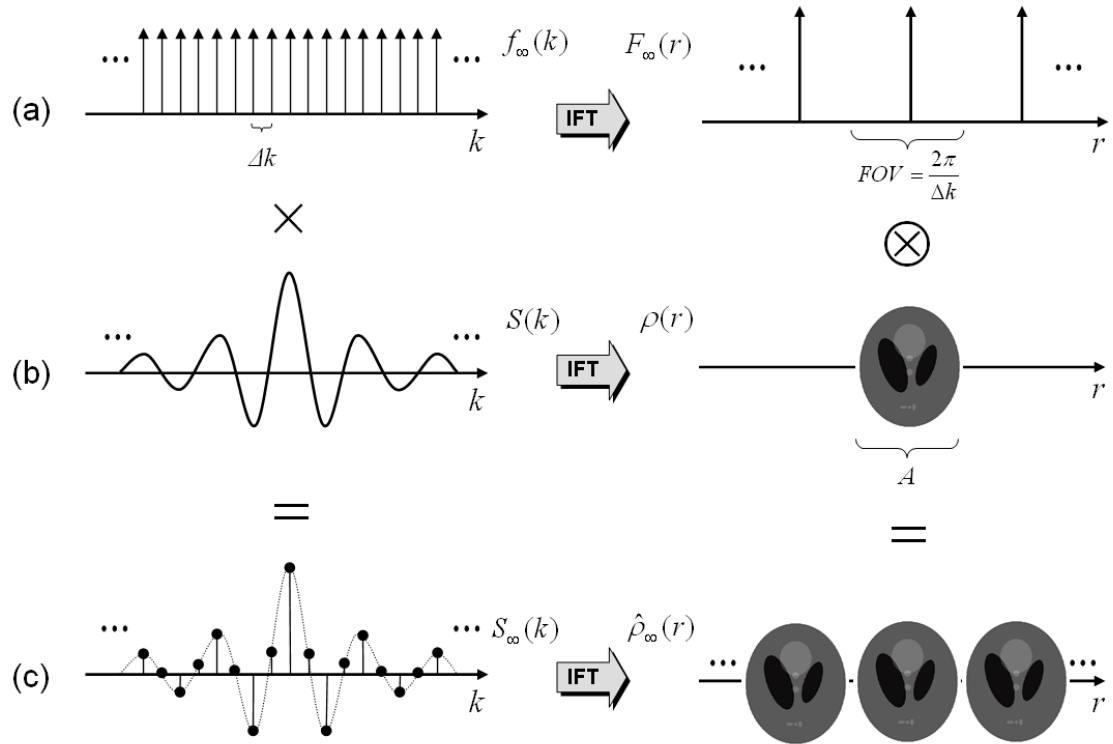
Figure 1.2: The infinitely and discritely sampled signal $S_\infty(k)$ can be expressed mathematically by a multiplication of the continuous signal $S(k)$ with the infinite sampling function $f_\infty(k)$ (left column). The reconstructed image $\hat{\rho}_\infty$ can be directly calculated by applying the inverse Fourier transformation to the infinite sampled signal $S_\infty(k)$ (c). Similarily, exploiting the convolution theorem, the image $\hat{\rho}_\infty$ can be found by a convolution of the physical spin density $\rho(r)$ with $F_\infty(r)$ (right column). $F_\infty(r)$ is connected with the sampling function $f_\infty(k)$ by the inverse Fourier transformation (a). Both functions are infinite series of dirac delta functions, but provided with different spacing ($f_\infty(k) \rightarrow \Delta k$, $F_\infty(r) \rightarrow FOV = \frac{2\pi}{\Delta k}$). Thus, discrete sampling results in uniformly-spaced replications of the physical spin density separated by FOV. As long as the Nyquist sampling criterion (see Eq. 1.19) is fulfilled, the physical spin density can be extracted by cropping out one replication from the reconstructed image series.

The approximated spin density $\hat{\rho}(r)$ for finite sampling can be calculated by the inverse Fourier transformation of the measured signal $\hat{S}(k)$.

$$\hat{\rho}(r) = \int_{-\infty}^{+\infty} \hat{S}(k) \cdot e^{ikx} dk = \Delta k \sum_{m=-n}^{n-1} S(m\Delta k) \cdot e^{im\Delta kx} \tag{1.21}$$

It is obvious that in the case of finite sampling, as in infinite sampling, the periodicity $\hat{\rho}(r) = \hat{\rho}(r - l\frac{2\pi}{\Delta k})$ is preserved for all positive and negative integers l. Exploiting again the convolution theorem, the reconstructed image $\hat{\rho}$ can be found by convolving the reconstructed image $\hat{\rho}_\infty$ obtained by infinitely sampling signal with a sinc-function, which is the inverse Fourier transformation of the rectangular window function. Thus, even in the case of finite sampling, the Nyquist criterion from Eq. 1.19 holds and has to be considered to avoid aliasing artifacts. Truncation of the data results in an additional blurring artifact due to the convolution with the sinc-function. A wide rectangular window function produces a narrowly peaked sinc-function, approaching a delta function in the limit of infinite sampling. Since the measurement of image-space is likewise discretized in steps of Δr and truncated to the finite $FOV = N\Delta r$, $S(m\Delta k)$ and $\hat{\rho}(q\Delta r)$ form a discrete Fourier transformation pair and are related by

$$
\begin{aligned}
S(m\Delta k) &= \Delta x \sum_{q=-n}^{n-1} \hat{\rho}(q\Delta r) \cdot e^{-im\Delta k \cdot q\Delta r} \\
\hat{\rho}(q\Delta r) &= \Delta k \sum_{m=-n}^{n-1} S(m\Delta k) \cdot e^{im\Delta k \cdot q\Delta r}
\end{aligned}
\tag{1.22}
$$

Thus, the image can be obtained directly from the discretely and finitely sampled signal simply by a discrete inverse Fourier transformation.

1.4.3   The Fourier Shift Theorem

An important property of Fourier theory is the Fourier Shift Theorem, which states that a shift of the sampling positions in k-space by $\alpha\Delta k$ results in a phase modulation of the replicates in the image space. This property can easily be proven by applying the inverse Fourier transform to the shifted sampling function.

$$
\begin{aligned}
f_\infty(k) &= \Delta k \sum_{m=-\infty}^{+\infty} \delta\left(k - (m+\alpha)\Delta k\right) \\
F_\infty(r) &= \sum_{l=-\infty}^{+\infty} \delta\left(r - l\frac{2\pi}{\Delta k}\right) \cdot e^{i2\pi l\alpha}
\end{aligned}
$$
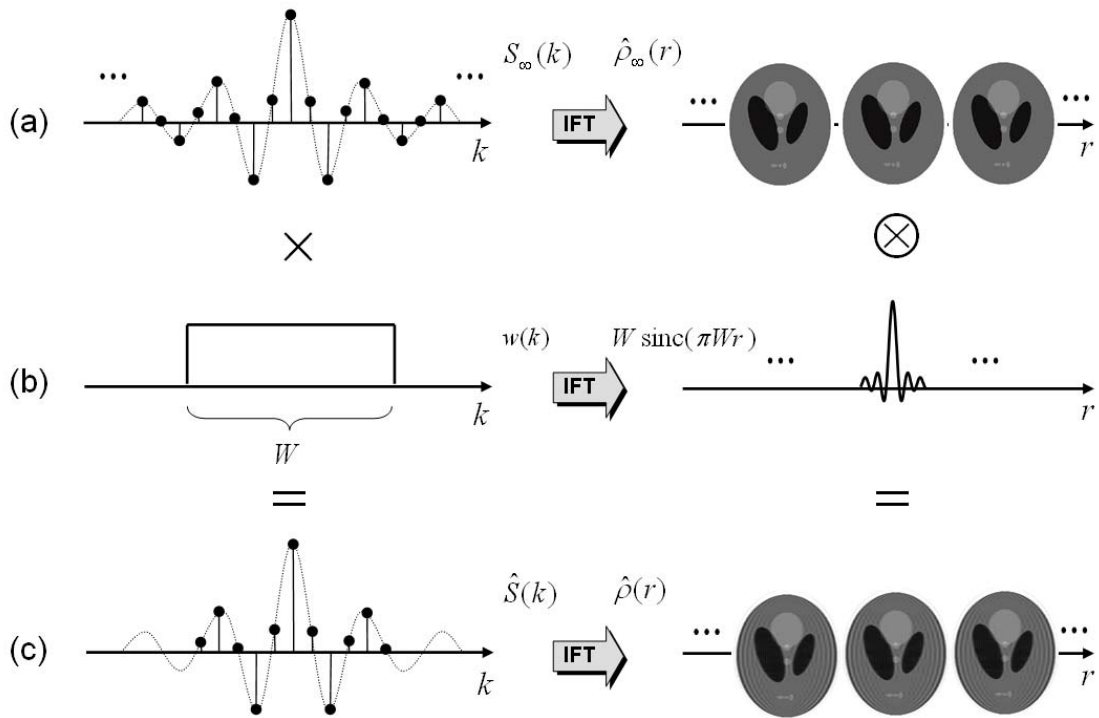
Figure 1.3: In addition to discrete sampling (see Fig. 1.2), the data are truncated to a finite number of data points. This can be expressed mathematically by a multiplication of the infinite sampled signal $S_\infty(k)$ with a rectangular window function $w(k)$ with width W (left column). Exploiting the convolution theorem, the final image can be calculated by an additional convolution of the reconstructed image after infinite sampling $\hat{\rho}_\infty(r)$ with a continuous sinc function $W \cdot \mathrm{sinc}(\pi W r)$, which is the inverse Fourier transformation of the truncation function $w(k)$ (right column). Thus, finite sampling results in so-called Gibbs-ringing and an additional blurring artifact; the Nyquist criterion, however, holds even when the data are truncated.

On the other hand, in order to shift the replicated images by $\beta \cdot FOV = \beta \frac{2\pi}{\Delta k}$ in the image space, the sampled signal has to be provided with a linearly decreasing phase.

$$
\begin{aligned}
F_\infty(r) &= \sum_{l=-\infty}^{+\infty} \delta\left(r - (l+\beta)\frac{2\pi}{\Delta k}\right) \\
f_\infty(k) &= \sum_{m=-\infty}^{+\infty} \delta\left(k - m\Delta k\right) \cdot e^{-i2\pi m\beta}
\end{aligned}
$$

These properties have essentially no impact on images sampled at the Nyquist rate. In the first case the center image ($l = 0$), which usally is cropped out, is not affected by the phase modulation and in the latter case the image is only shifted in the FOV and can be shifted back easily in a post processing step. However, it will be shown later in this work, that these properties have impact as soon as the Nyquist criterion is violated.

1.4.4 Aliasing

As mentioned above, aliasing occurs whenever the k-space is sampled at a rate which lies below the Nyquist criterion (Eq. 1.19) and is independent from the idea of finite sampling. Thus, it is sufficient to investigate the effect of aliasing on infinitely sampled data. In Fig. 1.4, the immediate consequence of sampling at a rate which lies below the Nyquist criterion is displayed ($FOV < A$). The infinite replicates overlap to a certain extent, thereby tempering the object information significantly. The greater the distance of sampling points in k-space is chosen, the smaller is the FOV and the more replicates are forced to merge together. For example, if the data are sampled at a rate which lies 4 times below the Nyquist criterion, 4 shifted replicates are overlapped on top of each other in the FOV.

In the frequency encoding direction, this type of aliasing artifact can be avoided by sampling k-space at a rate which lies beyond the Nyquist criterion (oversampling), followed by a low-pass filtering procedure to crop out the desired FOV, which can be chosen to be smaller than the object size. However, in the phase encoding direction, this strategy is not applicable because oversampling in the phase encoding direction requires increased number of phase encoding steps, demanding additional scan-time. Thus, to avoid aliasing in the phase encoding direction, the distance of subsequent phase encoding steps Δk is exactly determined by the Nyquist criterion.

1.5 Imaging Speed and SNR

MRI is generally considered to be limited by the signal-to-noise-ratio (SNR). Therefore, in the following, a brief overview of the most prominent limitations in MRI with regard to SNR and imaging speed are given. The SNR is defined as the signal level divided by the

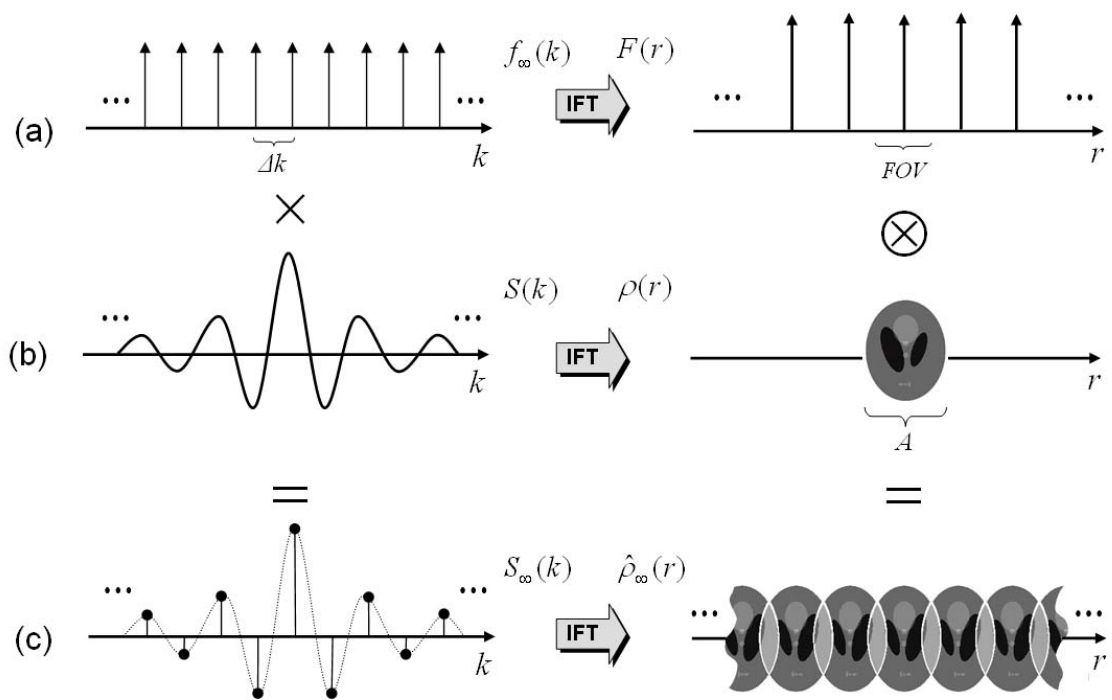**Figure 1.4:** Schematic description of the formation of aliasing artifacts in MRI. Sampling at a rate which lies below the Nyquist criterion $\Delta k > 2\pi/A$ results in a FOV smaller than the object size A causing the replicates to overlap.

standard deviation of the background noise. The signal intensity received in the receiver coil is proportional to the desired voxel size $\Delta V = \Delta x \Delta y \Delta z$ and increases linearly with the number of acquired data points $N = N_x N_y N_z$ ($N_z = 1$ for 2D imaging). Besides noise mechanisms which cannot be influenced by the MRI experiment, such as noise contributions originating from the sample or the receiver coil, or further losses in the receiver chain, the received noise contribution is basically proportional to the square root of the aquisition bandwidth $\sqrt{BW} = 1/\sqrt{\Delta t_x}$ at which the signal has been sampled. The noise distribution received has a gaussian shape and therefore noise increases only with the square root of the number of acquired data points $\sqrt{N}$. Thus, the SNR as a function of the basic imaging parameters is given by

$$SNR \propto \Delta x \Delta y \Delta z \cdot \sqrt{N_y N_z} \cdot \sqrt{ACQ} \tag{1.23}$$

where $ACQ = N_x \cdot \Delta t_x$. This is neglecting relaxation due to increased echo times. Because the SNR can always be increased by averaging the signal N_{rep} times at the cost of N_{rep}-fold increased imaging time, a metric is needed to determine how effectively an MRI experiment utilizes the available magnetization in a given amount of time. Since the SNR improves linearly with $\sqrt{N_{rep}}$, the SNR must be given per square root of the total imaging time T_{tot}. This value is known as the SNR efficiency or sensitivity Ψ. The total imaging time needed to form an image in MRI is given by the number of required rf excitations (number of phase encoding steps and number of repetitions) times the repetition time TR.

$$T_{tot} = N_y N_z N_{rep} \cdot TR \tag{1.24}$$

The repetition time TR is defined as time interval between subsequent rf excitations and is a fundamental limiting factor in terms of sensitivity and imaging speed in MRI. In most cases, the TR must be chosen to be significantly longer than the acquisition time ACQ, thereby inevitably implicating undesired dead-times during TR. Besides the finite gradient switching times, the reason for long repetition times are predominantly the effects of relaxation and the desired image contrast. Long repetition times significantly decrease SNR efficiency.

$$\Psi = \frac{SNR}{\sqrt{T_{tot}}} \propto \Delta x \Delta y \Delta z \cdot \frac{\sqrt{ACQ}}{\sqrt{TR}} \tag{1.25}$$

A further limitation in terms of imaging speed is the number of phase encoding steps required to form an image. This is especially true in cases where high resolution images are required and the repetition times are long because of the specific image contrast needed. In the past, a multitude of different strategies has been developed to reduce the dead-times significantly. For example rapid spin-warp imaging sequences such as FLASH [9] allow for very short repetition times by employing low flip angle excitation pulses. Single-shot or multi-shot sequences, such as echo planar imaging (EPI) [10] or turbo spin echo imaging (TSE) [11], minimize dead-times

by performing all or multiple phase encoding steps after one excitation during one TR. These rapid imaging sequences are distinguished by a high SNR efficiency. In some cases, however, these techniques operate at the SNR limit.

The advent of phased arrays [12] and the availability of multiple independent receiver channels has led to a further improvement in acquisition efficiency. These arrays of surface coils, if non-interacting, allow one to look at different or overlapping regions in the same slice. In phased arrays, the signals from all coil elements are detected simultaneously with seperate receivers, resulting in multiple independent single coil images. These images can be combined in order to form one image with improved SNR compared to single surface coil or volume coil images. The most prominent combination procedures are the *sum-of-squares* algorithm [12], providing maximum SNR or adaptive reconstruction [13] providing a homogenous sensitivity distribution in the final image.

Chapter 2

Basics of Parallel Imaging

2.1 Introduction

Besides the image contrast, imaging speed is probably the most important consideration in clinical magnetic resonance imaging (MRI). Unfortunately, current MRI scanners already operate at the limits of potential imaging speed, due to the technical and physiological limitations associated with rapidly switched magnetic field gradients. With the appearance of parallel MRI, a decrease in acquisition time can be achieved without the need to further increase gradient performance.

Parallel imaging works by taking advantage of spatial sensitivity information inherent in an array of multiple receiver surface coils positioned around the object under investigation (see Fig. 2.1) to partially replace time consuming spatial encoding, which normally is performed by switching magnetic field gradients. In this way, only a fraction of the phase encoding steps have to be acquired, directly resulting in an accelerated image acquisition while maintaining full spatial resolution and image contrast. Besides increased temporal resolution at a given spatial resolution, the time savings due to parallel MRI can also be utilized to improve the spatial resolution in a given imaging time. Furthermore, parallel MRI can diminish susceptibility-related artifacts by reducing the echo train length of single and multi-shot pulse sequences [14, 15].

Currently, the latest generation of MRI scanners provide up to 32 independent receiver channels, which theoretically allow a 32-fold increased image acquisition speed compared to traditional MR systems without a parallel MRI environment. At the moment, however, routine clinical experiments can only be accelerated by a factor of 2-4 and still maintain good image quality [16, 17]. Higher scan time reductions can be achieved in 3D experiments (acceleration factors 5-8) where the number of phase encoding steps can be reduced in two spatial dimensions. Even further scan time reductions have been obtained at research sites using specialized hardware (acceleration factors 9-12). These new generation MRI scanners with parallel MRI have provided the greatest incremental gain in imaging speed since the develop-
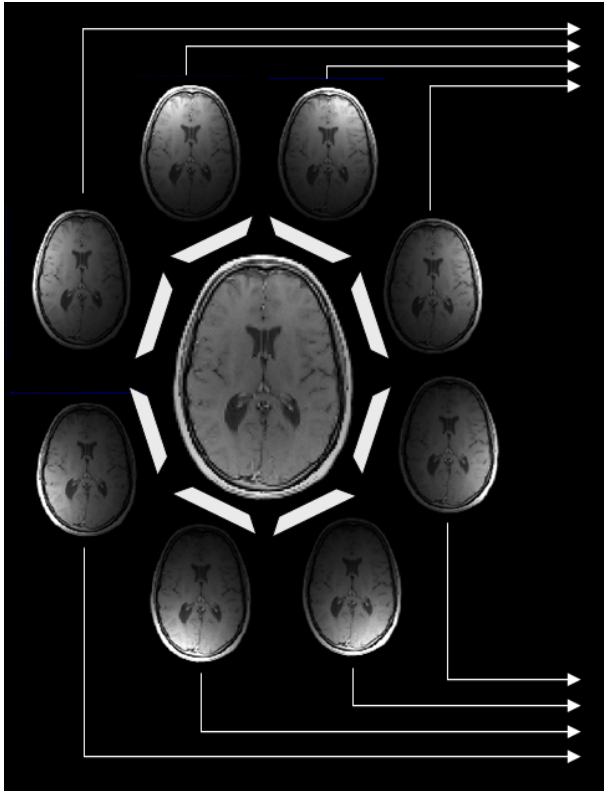
Figure 2.1: Fully encoded single coil images acquired with an eight channel head array. For a successful parallel imaging reconstruction multiple receiver coils are required, each provided with its own receiver pathway (indicated by the arrows). The coils are positioned in such a way that the entire object is covered. To partially accomplish spatial encoding the parallel image reconstruction procedure utilizes the fact that the coils are provided with different spatial sensitivity information.

ment of fast MRI methods in the 1980s.

2.2   Historical Overview

The idea of using rf receiver coils to encode an image, thereby dramatically increasing imaging speed, was introduced in the late 80ies. It is clear that many rf coils would be required to encode an image entirely by this method. At that time, however, neither the huge number of required independent receiver channels nor the huge number of decoupled rf coils were available, and still are not today. Around this time, Kelton *et al.* [18] proposed a combination of both encoding with magnetic field gradients and rf receiver coils. The reconstruction algorithm operates in image space using a matrix inversion to unfold the undersampled accelerated image. Although their implementation did not result in acceptable image quality and no *in vivo* results were presented, the concept of partially parallel acquisitions (PPA) was born. Only a few years later, Ra and Rim [19] presented a similar proposal with good results, but again no *in vivo* data were presented. A completely different approach was made in 1993 by Carlson and Minemura [20] who presented a k-space method capable of generating missing k-space lines from a series expansion of reduced k-space raw data in two distinct coils. Although this technique never worked robustly, it pioneered a new method in 1997, namely

SMASH (Simultaneous Acquisition of Spatial Harmonics), proposed by Sodickson et al. [21], which uses linear combinations of coil sensitivity profiles to generate spatial harmonics acting like additional phase encoding gradients. Sodickson and Griswold then presented a successful *in vivo* implementation of PPA using the SMASH technique, thereby starting the rapidly growing field of parallel imaging [22]. Only one year later, Pruessmann and Weiger proposed the concept of sensitivity encoding (SENSE) [23] which is strongly related to the early proposals of Kelton and Ra and Rim. The difference between the two is that SENSE uses an SNR optimized matrix inversion in combination with an initial coil sensitivity mapping. Since then, great progress in the development and improvement of parallel imaging reconstruction methods has taken place, thereby producing a multitude of different and somewhat related techniques and strategies [21, 23, 24, 25, 26, 27, 28]. Currently, the best-known are SMASH [21], SENSE [23] and GRAPPA [27]. However, various other techniques, such as AUTO-SMASH [25], VD-AUTO-SMASH [26], GENERALIZED SMASH [24], mSENSE [29], PILS [30] and SPACERIP [28] have also been proposed.

2.3 Basic Concepts

In parallel MRI, image acceleration is performed by skipping some phase encoding lines normally required to fully encode an image. This is usually done by increasing the distance of subsequent phase encoding steps, thereby sampling the k-space at a rate which is below the Nyquist criterion. As described earlier, this type of undersampled k-space yields aliasing artifacts in the image after inverse Fourier transformation. Parallel imaging methods make use of spatial sensitivity information provided by a receiver array in order to remove the aliasing artifacts in the image space, or to directly reconstruct the missing phase encoding lines in k-space. Therefore, current parallel MRI reconstruction methods can roughly be classified into two groups: those where reconstruction takes place in image space (e.g. SENSE [23], PILS [30]), consisting of an unfolding or inverse procedure (Fig. 2.2 right), and those, where the reconstruction procedure is performed in k-space (e.g. SMASH [21], GRAPPA [27]), consisting in a calculation of missing k-space data (Fig. 2.2 left). However, hybrid techniques, like SPACERIP, are also used. All PPA techniques require additional coil sensitivity information to eliminate the effect of undersampling in k-space. This sensitivity information can either be derived once during the patient setup by means of a pre-scan or by means of a few additionally acquired k-space lines for every subsequent parallel imaging experiment (auto-calibration) [25], or some combination of the two.
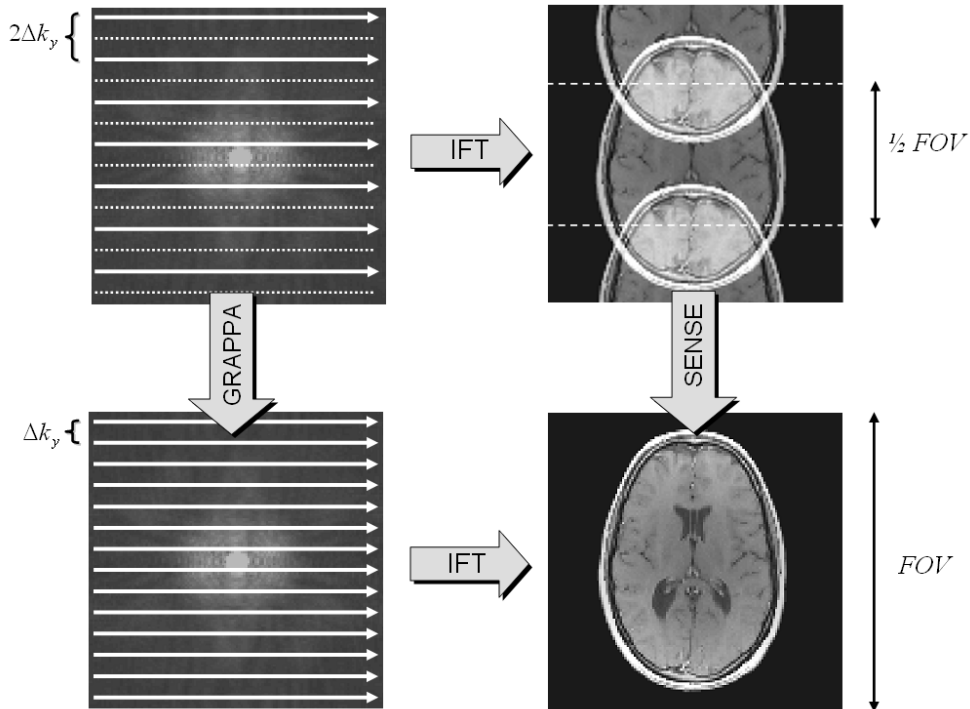
Figure 2.2: Description of the basic parallel imaging reconstruction concepts. The k-space is sampled at a rate which lies below the Nyquist criterion thereby reducing the number of required phase encoding steps. In this example, a two-times reduced acquisition is displayed, where solid lines represent acquired lines and dotted lines not acquired lines (upper left). Inverse Fourier transformation of this undersampled k-space results in aliasing artifacts in the image space (upper right). The parallel imaging reconstruction procedure can be performed either in k-space by directly solving for the missing k-space lines (lower left) or in image space by solving for the un-aliased full *FOV* image (lower right). The most prominent PPA techniques are GRAPPA, operating in k-space and SENSE, operating in the image domain.

The most important property, and limitation, of the parallel imaging approach is, that the signal to noise ratio (SNR) of an R-fold accelerated acquisition is reduced by a factor $\sqrt{R}$. The reason for this reduction is that the number of acquired phase encoding steps is reduced by a factor of R (see Eq. 1.23). This property limits the PPA concept to applications which do not already operate at the SNR limit. The most important requirements and properties of parallel MRI are recapitulated below:

- Multiple receiver coils with different coil sensitivities over the FOV are required.

- Each coil must be provided with its own receiver pathway.

- For parallel imaging reconstruction, an accurate knowledge of the coil sensitivity information is required.

- The SNR of the accelerated image is reduced at least by a factor $\sqrt{R}$ (see Eq. 1.23).

2.4 Technical Overview

In this section, a brief technical overview of today's most important parallel MRI reconstruction methods, namely SENSE (Sensitivity Encoding) [23] and GRAPPA (GeneRalized Autocalibrating Partially Parallel Acquisitions) [27], is given. While SENSE can be seen as an unfolding procedure in image space, GRAPPA operates in k-space and directly reconstructs the missing data in k-space for each coil. In the latter case, the component coil images are combined to form the final image after Fourier transformation.

Starting with a detailed description of the SENSE method, the basic SMASH [21] theory is discussed. Thereafter, the SMASH-related auto-calibrating methods AUTO-SMASH [25] and VD-AUTO-SMASH [26] are introduced, followed by a description of the most basic GRAPPA implementation. Finally, a more generalized implementation of GRAPPA is derived, which is, like SENSE, given in matrix notation.

In the last years, the GRAPPA method has been subject of continuous development, thereby steadily improving reconstruction speed and quality. Therefore, the GRAPPA algorithm presented here represents an up-to-date implementation and is based on the recently released open-source implementation by Mark Griswold, which differs significantly from the implementation described in the original GRAPPA [27] paper. To simplify matters, only Cartesian-type undersampled k-space is discussed. However, as mentioned earlier, there are other, non-Cartesian sampling strategies available where k-space is sampled using for example multiple spiral or radial trajectories. In the Cartesian case, however, the number of phase encoding steps is reduced by the reduction factor R by increasing the distance of equidistantly sampled k-space lines. To maintain resolution, the maximum k-values are left unchanged. In image space this type of undersampling of k-space yields in a reduced FOV in the phase encoding direction, which is associated with fold-over artifacts in the coil images as depicted in Fig. 2.2.

2.4.1 SENSE

The SENSE (SENSitivity Encoding) [23] parallel MRI reconstruction method can be briefly characterized as an image domain unfolding algorithm. In the Cartesian-type sampled k-space, the location of and distance between periodic repetitions in the image domain is well-known (see previous chapter). An accelerated acquisition (reduction factor R) results in a reduced FOV in every component coil image. Each pixel in the individual reduced FOV coil image will contain information from multiple (R), equidistantly distributed pixels in the desired full FOV image ρ. Additionally, these pixels are weighted with their sensitivities C at the corresponding locations l in the full FOV. Thus, the signal in one pixel at a certain location

received in the k-th component coil image I_k can be written as

$$I_k = \sum_{l=1}^{R} C_{kl} \cdot \rho_l \tag{2.1}$$

where the index k counts from 1 to N_c and the index l counts from 1 to R, specifying the locations of the pixels involved. By including all N_c coils, a set of N_c linear equations with R unknowns can be established and written in matrix notation:

$$\vec{I} = \hat{C} \cdot \vec{\rho} \tag{2.2}$$

As shown in Fig. 2.3, the vector $\vec{I}$ represents the complex coil image values at the chosen pixel and has length N_c. The matrix $\hat{C}$ denotes the sensitivities for each coil at the R superimposed positions and therefore has dimensions $N_c \times R$. The vector $\vec{\rho}$ lists the R pixels in the full FOV image. Using proper knowledge of the complex sensitivities at the corresponding positions, $\vec{\rho}$ can be calculated using a generalized inverse of the sensitivity matrix $\hat{C}$, the so-called pseudo inverse $\mathrm{pinv}(\hat{C})$

$$\mathrm{pinv}(\hat{C}) = (\hat{C}^H \cdot \hat{C})^{-1} \cdot \hat{C}^H$$

where the superscript H denotes the complex conjugate transposed of a matrix. Thus, the desired image pixels $\vec{\rho}$ can be derived by

$$\vec{\rho} = \mathrm{pinv}(\hat{C}) \cdot \vec{I} \tag{2.3}$$

To simplify matters, the issue of noise correlation is not addressed in Eq. 2.3. However, to account for levels and correlations of stochastic noise in the receiver channels, this issue may be included, which is important especially when the receiver coils are not completely decoupled. A detailed description is given in reference [23].

The unfolding process in Eq. 2.3 is possible as long the matrix inversion can be performed. Therefore, the number of pixels to be separated (R) must not exceed the number of coils (N_c) in the receiver array. The SENSE algorithm (Eq. 2.3) must be repeated for every pixel location in the reduced FOV image to finally reconstruct the full FOV image. SENSE provides parallel MRI with arbitrary coil configurations, however, at the expense of some additional SNR loss which depends on the underlying geometry of the coil array. The encoding efficiency at any position in the FOV with a given coil configuration can be analytically described by the geometry factor (g-factor), which is a measure of how easily the matrix inversion in Eq. 2.3 can be performed. The geometry factor g_l can be calculated according to

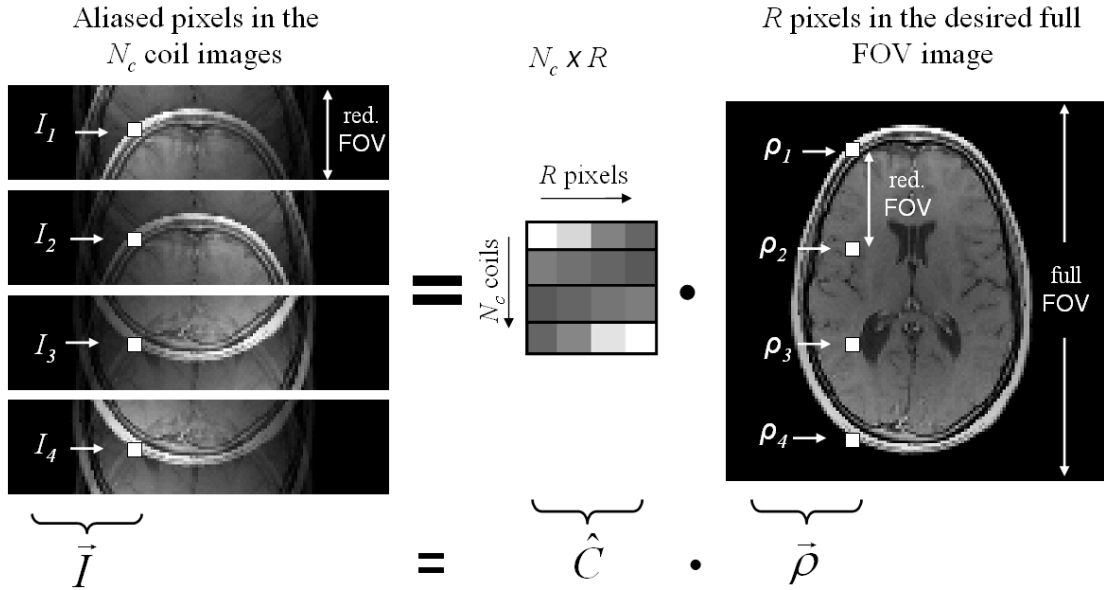$$g_l = \sqrt{[(C^H C)^{-1}]_{l,l} \cdot [C^H C]_{l,l}} \geq 1 \tag{2.4}$$

Figure 2.3: Illustration of the basic SENSE relation using an accelerated ($R = 4$) parallel MRI acquisition with $N_c = 4$ receiver coils. $\vec{I}$ contains the aliased pixels at a certain position in the reduced FOV coil images. The $N_c \times R$ sensitivity matrix $\hat{C}$ assembles the corresponding sensitivity values of the component coils at the locations of the involved ($R = 4$) pixels in the full FOV image $\vec{\rho}$.

and describes analytically the local noise enhancement at the positions of the R involved pixel locations $l = 1, ...R$ and can take values greater than one. The term $[...]_{l,l}$ represents the diagonal matrix elements. Thus, the SNR in the final SENSE image is additionally reduced by the g-factor.

$$SNR_l^{SENSE} = \frac{SNR_l^{full}}{g \cdot \sqrt{R}} \tag{2.5}$$

A more detailed description of the g-factor calculation accounting for potential noise correlations is given in the original SENSE paper [23].

2.4.2   SMASH

Like SENSE, pure SMASH (SiMultaneous Acquisition of Spatial Harmonics) at its basic level requires a prior estimation of the individual coil sensitivities of the receiver array. The basic concept of SMASH is that a linear combination of these estimated coil sensitivities can directly generate missing phase-encoding steps, which would normally be performed by using phase encoding magnetic field gradients. In this case, the sensitivity values $C_k(x, y)$ are linearly combined with appropriate weighting factors in such a way that composite sensitivity profiles C_m^{cmp} with sinusoidal spatial sensitivity variations of the order m are generated, which are

intended to replace the modulations normally generated by phase encoding gradients:

$$C_m^{cmp}(x,y) = \sum_{k=1}^{N_c} w_k^{(m)} C_k(x,y) \approx e^{im\Delta k_y y} \tag{2.6}$$

Here, $k_y = \frac{2\pi}{FOV}$ and the index k counts from 1 to N_c for an N_c-element array coil, while m is an integer specifying the order of the generated spatial harmonic. Within this linear equation, the only unknowns are the weighting factors or coil weights $w_k^{(m)}$, which can be estimated by fitting (eg, least squares fit [31]) the coil sensitivity profiles $C_k(y)$ to the spatial harmonic $e^{im\Delta k_y y}$ of order m. The component coil signal $S_k(k_y)$ in one dimension (phase encoding direction) which is received in coil k is the Fourier transformation of the spin density $\rho(y)$ weighted with the corresponding coil sensitivity profile $C_k(y)$:

$$S_k(k_y) = \int C_k(y)\rho(y) \cdot e^{ik_y y} dy \tag{2.7}$$

Using Eq. 2.6 and 2.7, an expression may be derived to generate shifted k-space lines $S^{cmp}(k_y + m\Delta k)$ from weighted combinations of measured component coil signals $S_k(k_y)$.

$$
\begin{aligned}
\sum_{k}^{N_c} w_k^{(m)} S_k(k_y) &= \int \sum_{k}^{N_c} w_k^{(m)} C_k(y)\rho(y) \cdot e^{ik_y y} dy \\
&\approx \int \rho(y) \cdot e^{ik_y y} \cdot e^{im\Delta k_y y} dy = S^{cmp}(k_y + m\Delta k_y)
\end{aligned} \tag{2.8}
$$

Eq. 2.8 represents the basic SMASH relation and indicates that linear combinations of component coils can actually be used to generate k-space shifts in almost the same manner as magnetic field gradients in conventional phase-encoding. In general, SMASH is strongly restricted to coil configurations that are able to generate the desired spatial harmonics in phase encoding direction with adequate accuracy.

2.4.3 AUTO-SMASH and VD-AUTO-SMASH

Unlike SMASH, which uses a prior estimation of component coil sensitivities, AUTO-SMASH uses $R - 1$ additionally acquired auto-calibration signal (ACS) lines in the center of k-space during the actual scan to estimate the sensitivities. In contrast to normal SMASH, these additionally acquired ACS lines S_k^{acs} are used to automatically derive the set of linear weights $w_k^{(m)}$. In the absence of noise, the linear combination of adequately weighted signals $S_k(k_y)$ received in the individual component coils can generate a composite Signal S^{cmp} which is shifted in k-space by $m\Delta k_y$. In other words, if auto-calibration signals are acquired at positions $k_y + m\Delta k_y$ in k-space and linearly combined to form the composite signal S^{cmp} at $k_y + m\Delta k_y$ the SMASH equation yields the AUTO-SMASH equation:

$$S^{cmp}(k_y + m\Delta k_y) = \sum_{k=1}^{N_c} S_k^{acs}(k_y + m\Delta k_y) \approx \sum_{k=1}^{N_c} w_k^{(m)} S_k(k_y) \qquad (2.9)$$

By fitting the component coil signals to the composite signal S^{cmp}, which is composed of ACSs $S_k^{acs}(k_y + m\Delta k_y)$, a set of coil weights $w_k^{(m)}$ can be derived which shift measured lines by $m\Delta k_y$ in k-space. In this way, missing k-space data can be calculated from measured k-space data to form a complete, fully-encoded k-space, resulting in a full FOV image after inverse Fourier transformation.

In order to further improve the reconstruction procedure of the AUTO-SMASH approach, the concept of variable-density (VD)-AUTO-SMASH was introduced. In this method, a fully encoded low resolution data block of ACS lines is acquired in the center of k-space. It has been shown that the number of available fitting procedures with which one can derive the weights for the desired k-space shifts (m) is significantly increased just by adding a few extra ACS lines to the acquisition [26]. Furthermore, these reference lines can be integrated into the k-space in a final reconstruction step to further improve image quality. The VD-AUTO-SMASH approach provides the best suppression of residual artifact power at a given total acceleration factor R, using the maximum possible undersampling in the outer k-space in combination with the highest possible number of ACS lines in the center of k-space. This strategy results in a more accurate determination of the reconstruction coefficients, especially in the presence of noise and a more robust image reconstruction in the presence of imperfect coil performance.

2.4.4 GRAPPA

GRAPPA (GeneRalized Autocalibrating Partially Parallel Acquisitions) [27] represents a more generalized implementation of the VD-AUTO-SMASH approach. Although both techniques share the same acquisition scheme, they differ significantly in the way the reconstruction of missing k-space lines is performed. One basic difference is that the component coil signals $S_k(k_y)$ are fit to just a single component coil ACS signal $S_l^{acs}(k_y + m\Delta k_y)$, thereby deriving a set of weights $w_{lk}^{(m)}$ to reconstruct missing k-space lines in each component coil:

$$S_l^{acs}(k_y + m\Delta k_y) \approx \sum_{k=1}^{N_c} w_{lk}^{(m)} S_k(k_y) \qquad (2.10)$$

The GRAPPA reconstruction algorithm described here in this work differs in part from the implementation proposed by Mark Griswold *et al.* in the original GRAPPA paper four years ago [27]. The early GRAPPA uses a block of multiple k-space lines acquired in each coil to fit an ACS k-space line in one single coil in order to derive the reconstruction weights for the missing k-space line in that coil. This procedure is then repeated for each coil. The up-to-date GRAPPA implementation presented here is more general and more intuitive and has shown to provide a better and more robust parallel image reconstruction. A detailed description of
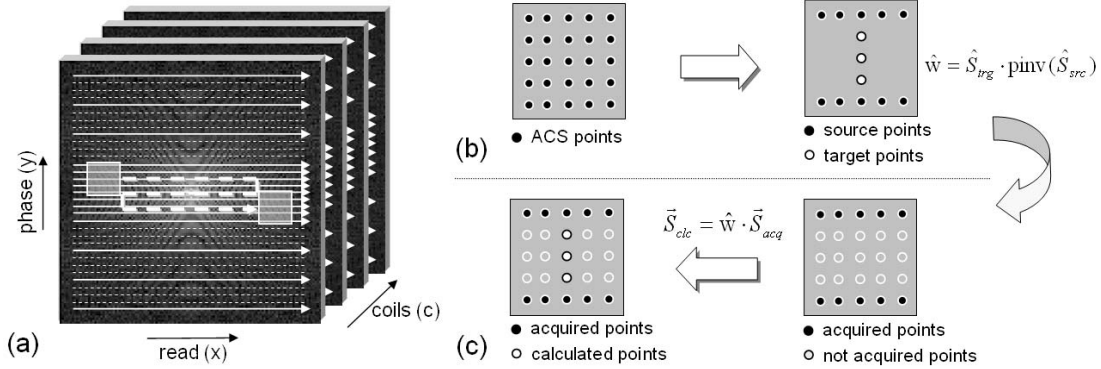
Figure 2.4: Schematic description of the GRAPPA reconstruction procedure. On the left (a), schematically, the k-space of a $R = 4$-fold undersampled PPA acquisition for all ($N_c = 4$) coils is depicted, including the fully-encoded low-resolution ACS block in the center of k-space. In order to calculate the weights, a small reconstruction kernel is chosen in which source and target points are selected (b) for each coil (coil dimension is omitted for simplicity). In this case, a 2×5 source kernel was used matching the $R = 4$-fold undersampled data pattern. The target points are selected to the $R - 1 = 3$ missing data points in the center of the reconstruction kernel. The source points from all coils may then be assembled in a vector $\vec{S}_{src}$, the target points in a different vector $\vec{S}_{trg}$. Using a sliding block implementation, multiple repetitions of the reconstruction kernel can be found in the ACS data and accumulated in a source $\hat{S}_{src}$ and target matrix $\hat{S}_{trg}$. By fitting $\hat{S}_{src}$ to $\hat{S}_{trg}$, the appropriate weights w can be derived. When applied to the undersampled data (c), the weights generate the missing data points at the corresponding k-space position in all component coils simultaneously.

the novel GRAPPA procedure is given below.

The GRAPPA reconstruction formalism given in Eq. 2.10 can also be written in matrix form. The vector $\vec{S}$ represents the collected signal in each element coil at some position k_y and therefore has length N_c. Using GRAPPA in its simplest form, a set of weights $\hat{w}^{(m)}$ may be derived by fitting the signal $\vec{S}$ to the ACS $\vec{S}_{acs}^{(m)}$ at the position $(k_y + m\Delta k_y)$ in each coil. Therefore, the coil-weighting matrix $\hat{w}^{(m)}$ has dimension $N_c \times N_c$ and shifts the k-space data in each coil by $m\Delta k_y$.

$$\vec{S}_{acs}^{(m)} \approx \hat{w}^{(m)} \vec{S} \qquad (2.11)$$

In a more generalized implementation, multiple source data points (according to the acquired points) can be collected in $\vec{S}_{src}$ and fitted directly to multiple target data points (according to the missing points) assembled in $\vec{S}_{trg}$ to derive the appropriate coil weights $\hat{w}$ from the ACS data.

In Fig. 2.4, a schematic description of the GRAPPA reconstruction procedure is given. On the left (a) the sampling scheme of an $R = 4$ accelerated acquisition for each component coil is shown. Additionally, the fully encoded low resolution ACS data in the center of k-space is

displayed. A small reconstruction kernel is chosen (b) in which source data points and target data points are selected. The source points must be picked so that they match the reduced sampling pattern, while the target points are chosen according to the $(R-1)$ missing data points. A $N_y^{src} \times N_x^{src}$ source-kernel is fitted to the $(R-1)$ target points simultaneously for all coils, resulting in a total number of source points of $N_{src} = N_c \cdot N_y^{src} \cdot N_x^{src}$ and a total number of target points $N_{trg} = N_c \cdot (R-1)$. The reconstruction can be greatly improved by sliding the reconstruction kernel through the ACS data in the read (k_x) and the phase (k_y) encoding direction. The sliding block implementation results in a further increased accuracy of the fit procedure (ie, over determined system) and therefore in better artifact suppression. Using a $N_y^{acs} \times N_x^{acs}$ ACS data block for coil calibration, the kernel can be found several (N_{rep}) times within the ACS data. All the source data can then be assembled in an $N_{src} \times N_{rep}$ -source matrix $\hat{S}_{src}$ and an $N_{trg} \times N_{rep}$ -target matrix $\hat{S}_{trg}$. Similar to Eq. 2.11 a weighting matrix $\hat{w}$ is needed which ensures the following condition:

$$\hat{S}_{trg} \approx \hat{w} \cdot \hat{S}_{src} \tag{2.12}$$

The $N_{trg} \times N_{src}$ weighting matrix $\hat{w}$ can then easily be calculated by multiplying $\hat{S}_{trg}$ with the generalized inversion matrix of $\hat{S}_{src}$.

$$\hat{w} \approx \hat{S}_{trg} \cdot \mathrm{pinv}(\hat{S}_{src}) \tag{2.13}$$

Finally, in the actual reconstruction step (Fig. 2.4 (c), the missing data can be calculated by applying the weights $\hat{w}$ to a vector $\vec{S}_{acq}$ containing a set of acquired data points according to the source data kernel. The resulting vector $\vec{S}_{clc} = \hat{w} \cdot \vec{S}_{acq}$ contains the calculated $R-1$ missing points for each coil according to the position of the target points. Using a sliding block reconstruction for each k_x and k_y position in the undersampled data set, all the missing points at position $(k_x, k_y + m\Delta k_y)$ can be calculated for all coils simultaneously, where m runs from $m = 1, ..., (R-1)$.

In contrast to a SMASH or (VD)-AUTO-SMASH complex sum image reconstruction, the GRAPPA algorithm results in uncombined single coil images, which can be combined using a magnitude reconstruction procedure (eg, sum of squares). This provides a significantly improved SNR performance, especially at low reduction factors. Furthermore, signal losses due to phase cancellations are essentially eliminated using a magnitude reconstruction procedure. Thus, previous drawbacks of k-space-based techniques, namely phase cancellation problems, low SNR, and poor reconstruction quality due to a suboptimal fit procedure, are essentially eliminated. Furthermore, similar to SENSE, the GRAPPA algorithm works with essentially arbitrary coil configurations. Finally, as an additional benefit, the ACS lines used to derive the reconstruction coefficients can in many cases be integrated into the final image reconstruction, in the same manner as in VD-AUTO-SMASH.

2.5 Sensitivity Assessment

A successful SENSE reconstruction is strongly dependent on an accurate knowledge of the coil sensitivities. Since the sensitivity varies with coil loading, the sensitivities must be assessed by an additional reference acquisition integrated into the actual imaging setup. This can be performed, for example, by acquiring a low-resolution fully Fourier-encoded 3D data set received in each component coil, which allows arbitrary slice positioning and slice angulations. Thus, sensitivity maps can be derived by any of these methods described in literature:

- dividing each component coil image by an additional body coil image [23].

- dividing each component coil image by a sum of square image including phase modulation [32].

- dividing each component coil image by one component coil image (relative sensitivity maps) [33].

- an adaptive sensitivity assessment based on the correlation between the component coil images [13].

In an additional numerical process, these raw-sensitivity maps must be refined using smoothing (ie, minimizing the propagation of additional noise from the calibration scan into the reconstructed image) and extrapolation algorithms (ie, to provide coils sensitivity information from regions where MR signal is hard to obtain). In this work, coil sensitivity maps were derived using the adaptive sensitivity assessment proposed by Walsh et al. [13].

2.6 Auto-Calibration

The concept of auto-calibration was first presented by Jakob et al. in 1998 [25], who proposed the AUTO-SMASH technique. The philosophy of auto-calibration differs significantly from other approaches in which the sensitivity information is derived only once during the patient setup (eg, pre-scan). Auto-calibration may imply acquisition of reference signals directly in front of, during, or after the actual accelerated MRI experiment. This is beneficial because the accurate knowledge of the spatial sensitivity information of the underlying coil array is a crucial element in PPAs and it is difficult to ensure that the patient and coil positions remain unchanged during the entire clinical protocol, especially when using flexible array coils or when patient motion is inevitable (eg, respiratory motion, uncooperative patients). In general, an inaccurate estimation of coil sensitivity information results in bad image quality. Therefore, the auto-calibration concept can in many cases provide a more robust parallel MRI reconstruction. In addition, the ACS lines can often be integrated into the final image, thereby additionally improving image quality by reducing residual artifact power and increasing SNR.

However, it is important to note that generally any fully-encoded low-resolution scan with arbitrary image contrast can be used for coil calibration [34], which is beneficial in many cases. It is clear that, when following this strategy, the reference data must not be included in the final image. However, the concept of auto-calibration is not restricted to k-space-related parallel MRI reconstruction methods. In principle, one can use the ACS lines required for a GRAPPA reconstruction as well to derive low-resolution coil sensitivity maps for SENSE reconstructions within every subsequent parallel MRI experiment. This is done, for example, in the mSENSE [29] method.

2.7 Coil Arrangement Considerations

In principle, both commercially available techniques, SENSE and GRAPPA, allow an arbitrary coil configuration around the object. This means that these techniques are not restricted to linear coil configurations or localized sensitivities, such as in SMASH or in PILS. However, sufficient coil sensitivity variations in the phase-encoding direction in which the reduction is performed must be ensured. The geometry factor (g-factor) describes the local noise enhancement in the final SENSE image when using a given coil configuration. Therefore, the g-factor represents an easy and elegant way to estimate the encoding efficiency of a receiver array. In general, to optimize a coil configuration for a specific application, one should simulate g-factors for several coil configurations. Although the g-factor actually represents a quantitative estimation of noise enhancement for SENSE reconstructions, it has been shown that g-factor estimation works qualitatively for GRAPPA as well, since GRAPPA is subject to the same requirements in terms of coil configuration. Recently, quantitative representation of noise enhancement after GRAPPA reconstruction has also been derived, which can be calculated directly from the GRAPPA coil weights [35, 36].

2.8 Open Issues

Four years ago only the image domain based SENSE method proposed by Pruessman *et al.* and the k-space based GRAPPA reconstruction method introduced by Griswold *et al.* provided a robust parallel image reconstruction. However, both techniques allowed only moderate image accelerations ($R = 2-3$) with acceptable image quality. The main reason was that at this time the number of available coils in state-of-the-art receiver arrays were limited to a maximum of 4-6 elements. Only the rapid development of coil arrays providing more elements and the idea to apply the parallel imaging concept in two phase encoding directions in volumetric imaging (2D SENSE) allowed for higher image accelerations. However, this had been only possible for SENSE reconstructions, while at this time GRAPPA was not yet ready for volumetric parallel MRI. Thus, GRAPPA agorithms were needed for a robust reconstruction of accelerated 3D data sets. Additionally, as the sensitivity variation provided by the receiver array is

the crucial point for a successful parallel image reconstruction, strategies were needed for
the efficient utilization of the available sensitivities to further gain imaging speed. While
the autocalibrating approach had been shown to provide robust image reconstructions even
when the coil sensitivities changed during the accelerated experiment, it suffers from a non-
optimized image acceleration because some extra data is required for the coil calibration. This
is a problem particularily in dynamic imaging experiments, because this acquisition scheme
significantly decreases temporal resolution. In the following chapters, strategies and concepts
are provided which address these limitations.

Chapter 3

Dynamic autocalibrated parallel imaging using temporal GRAPPA (TGRAPPA)

3.1 Introduction

In dynamic imaging, a series of images with identical imaging parameters is acquired in order
to track motion of, for example, the beating human heart. For diagnostic purposes, a certain
spatial and temporal resolution is required. ECG gated, segmented CINE imaging [37] of the
human heart provides this resolution by distributing the acquisition over multiple heart cycles,
typically within one breath-hold. However, this technique is restricted to periodic motion, such
as the beating heart, and is extremely vulnerable to arrhythmia or any patient motion which
may occur during the examination, for example, respiratory motion. For applications showing
non-periodic dynamics, such as swallowing or movements of the limbs, a real-time acquisition
is required. Another important application is real-time catheter tracking [38]. With today's
fastest imaging sequences, frame rates of about 5 to 10 frames per second (fps) are feasible
with adequate spatial resolution. However, at such moderate frame rates spatial resolution is
degraded due to motion faster than the frame rate. By applying the parallel imaging concept
the frame rate can potentially be increased by a factor of 3 to 4 without changing spatial
resolution or contrast behaviour, thereby providing frame rates in the order of 20 to 40 *fps*.
For most applications, higher frame rates are not required, because the human eye is not
capable of resolving motion at higher rates. Therefore, further reductions in scan time can
be utilized to increase spatial resolution. The gain in imaging speed could potentially also be
used to make real-time 3D imaging feasable.

In the previous chapter, the parallel imaging reconstruction techniques SENSE [23] and
GRAPPA [27] were introduced. Both techniques require an additional fully-encoded reference

dataset to estimate the spatial coil sensitivity information which is needed for the paral-
lel imaging reconstruction procedure. This calibration scan takes some additional time and
therefore slightly degrades image acceleration. As already mentioned, this information can be
acquired only once during the patient setup and can then be used for every subsequent accel-
erated experiment in the study. This strategy is time-efficient but suffers as soon as the coil
sensitivity information changes in time for example due to patient motion, directly resulting in
severe residual reconstruction artifacts. In contrast, the auto-calibration approach [25] collects
the calibration data directly before, during or directly after the actual undersampled experi-
ment. Following this strategy, possible changes in coil sensitivity information can be tracked
efficiently at the expense of longer overall experiment times. The k-t SENSE [39] method
uses both spatial and temporal correlations provided by the dynamic image series for highly
accelerated dynamic imaging. However, this method uses prior knowledge of the dynamic and
therefore requires some additional training data for image reconstruction. It is clear, that in
case of a mismatch between the real acquisition and the training data this method provides
errorneous reconstruction results. This misregistration can easily occur when significant pa-
tient motion or non-periodic dynamics are present. The k-t GRAPPA [40] approach does not
require additional training data and exploits correlations in k-space and in time to interpolate
the missing data in k-space, however, at the expense of decreased temporal resolution.

In dynamic parallel imaging, a time-interleaved acquisition scheme similar to UNFOLD
[41], TSENSE [42], kt-SENSE [39] and kt-GRAPPA [40] may be exploited in order to obtain
this sensitivity information directly from the actual accelerated dynamic imaging experiment,
thereby realizing the full image acceleration. To this end, directly adjacent time frames can
be merged in k-space to build a fully encoded, full-resolution reference data set which can be
used as the auto-calibration signal (ACS) for an improved GRAPPA reconstruction. With
every acquired time frame in the series, a new set of ACS lines can be generated. This
allows one to update the coil weighting coefficients for the GRAPPA algorithm dynamically,
thereby automatically tracking changes in relative coil sensitivities over time efficiently. In
particular, this method is beneficial whenever coil sensitivity maps, as required for the SENSE
algorithm, are difficult to obtain. This is the case in inhomogeneous regions with low SNR
(e.g. the lung) [15]. In this work, temporal GRAPPA (TGRAPPA) [43] reconstructions
of accelerated (reduction factor two to four) real-time (non-gated), free breathing cardiac
studies are presented. Additionally it is shown that further imaging speed can be achieved by
combining TGRAPPA with the concept of partial Fourier acquisition [44].

3.2   Methods

Several *in vivo* experiments were performed on a Sonata $1.5\,T$ clinical whole body scanner
(Siemens Medical Solutions, Erlangen, Germany) equipped with eight independent receiver

channels. For signal reception, an 8-element receiver coil array (Nova Medical, Wilmington, MA, USA) was used. A trueFISP sequence was chosen for real-time non-breath-hold cardiac imaging. The imaging parameters were as follows: echo time $TE = 1.11\,ms$, repetition time $TR = 2.22\,ms$, $FOV = 36.0\,cm \times 29.2\,cm$, matrixsize $= 128 \times 60$, slice thickness $= 8\,mm$, flip angle $= 50°$. The final image resolution was $2.8\,mm \times 4.8\,mm$. The phase encoding direction was chosen to be in the anterior-posterior (AP) direction in all experiments. Four volunteers were examined and informed consent was obtained before the study. Non-gated dynamic cardiac imaging experiments during different breathing scenarios were performed using the UNFOLD acquisition scheme at frame rates accelerated from approximately 7.5 frames per second (fps) ($R = 1$) to $30\,fps$ ($R = 4$). The experiments were performed during normal breathing, fast breathing and deep breathing conditions. As described in the previous section, the proposed TGRAPPA [43] scheme derives the auto-calibration signals over time directly from the undersampled data itself. The final PPA image reconstructions were performed off-line with the GRAPPA algorithm using the MATLAB programming environment (The Mathworks, Natick, MA.). The GRAPPA coil weighting coefficients were determined by solving a set of linear equations using the ACS lines acquired according to the proposed TGRAPPA scheme. The Matlab reconstruction times, which were not optimized for real time applications, were approximately $2 - 3\,s$ per frame. Optimized software-based reconstruction should be feasible at frame rates of $15 - 30\,fps$.

Fig. 3.1 shows a schematic depiction of the time-interleaved acquisition scheme for an acceleration factor of $R = 4$. In this example, the undersampled k-space data from at least four adjacent time frames must be merged to build a complete set of k-space data for the GRAPPA reconstruction of one time-frame. In general, more neighboring frames can be averaged to increase the signal to noise ratio (SNR) of the ACS data, resulting in a potentially improved GRAPPA reconstruction. With every acquired time-frame in the series, a new set of ACS data may be used to reconstruct the next frame in the time series, thereby tracking changes in relative coil sensitivities over time.

The TGRAPPA reconstruction procedure was set up as follows: By performing a sliding block implementaion, the GRAPPA reconstruction coefficients were dynamically updated by merging 6 ($R = 2$), 9 ($R = 3$), 12 ($R = 4$) neighboring undersampled time frames at a time, as depicted in Fig. 3.1. For the first 4 ($R = 2$), 5 ($R = 3$), and 7 ($R = 4$) time frames of the series the GRAPPA reconstruction coefficients were derived from the first 6 ($R = 2$), 9 ($R = 3$), and 12 ($R = 4$) time frames. The same strategy was used for the last time frames.

In order to demonstrate the feasability of combining TGRAPPA with the partial Fourier concept, the accelerated $R = 2$, $R = 3$ and $R = 4$ data series were additionally reduced by 25% (partial fourier factor $pf = 0.75$) as depicted in Fig. 3.2. This corresponds to increased virtual frame rates of $20\,fps$ ($R = 2$), $30\,fps$ ($R = 3$) and $40\,fps$ ($R = 4$).

In the first reconstruction step the GRAPPA algorithm is applied to the reduced (including
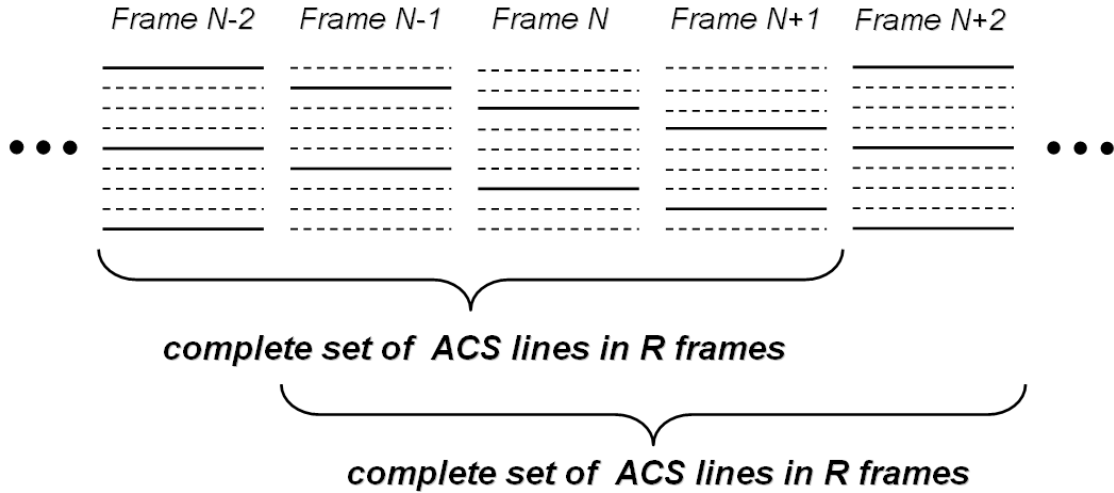
Figure 3.1: Schematic description of the time interleaved acquisition scheme for a reduction factor of $R = 4$. Solid lines represent acquired and dotted lines not acquired k-space lines. At least R adjacent time-frames in k-space must be merged to build a fully-encoded full-resolution reference ACS data set for a GRAPPA reconstruction of frame N. With every acquired time frame in the series, a new set of ACS lines can be derived to reconstruct the next frame in the time series. This figure is reprinted from reference [43].

partial Fourier reduction) k-space. In the second step the POCS (Projection Onto Convex Sets) algorithm is carried out yielding the final fully-encoded full-resolution k-space [45]. In this case, the GRAPPA reconstruction parameters were derived from partial Fourier ($pf = 0.75$) ACS-data achieved by merging neighbouring time-frames as already described in Fig. 3.1. Therefore, the number of ACS-lines available for the GRAPPA reconstruction were reduced from 60 to 45.

3.3 Results

In Fig. 3.3, representative images for acceleration rates of (a) $R = 1$ (unaccelerated) (7.5 fps), (b) $R = 2$ (15 fps), (c) $R = 3$ (22.5 fps) and (d) $R = 4$ (30 fps) under normal breathing conditions are shown. The coil weighting coefficients for the GRAPPA reconstructions were derived from 6 ($R = 2$), 9 ($R = 3$), and 12 ($R = 4$) neighboring time frames, forming a high SNR, fully-encoded, full-resolution set of ACS data, corresponding to a temporal window of $0.4\,s$. This results in a GRAPPA reconstruction with good artifact suppression up to frame rates of 30fps.

Fig. 3.4 illustrates the influence of inaccurate sensitivity information, which may arise due to significant respiratory motion during deep breathing. As an example, two time frames (Frame 5, Frame 151) are shown from an accelerated (R=4) non-gated, non-breath-held dynamic cardiac imaging experiment with a temporal resolution of approximately 30 fps. The im-
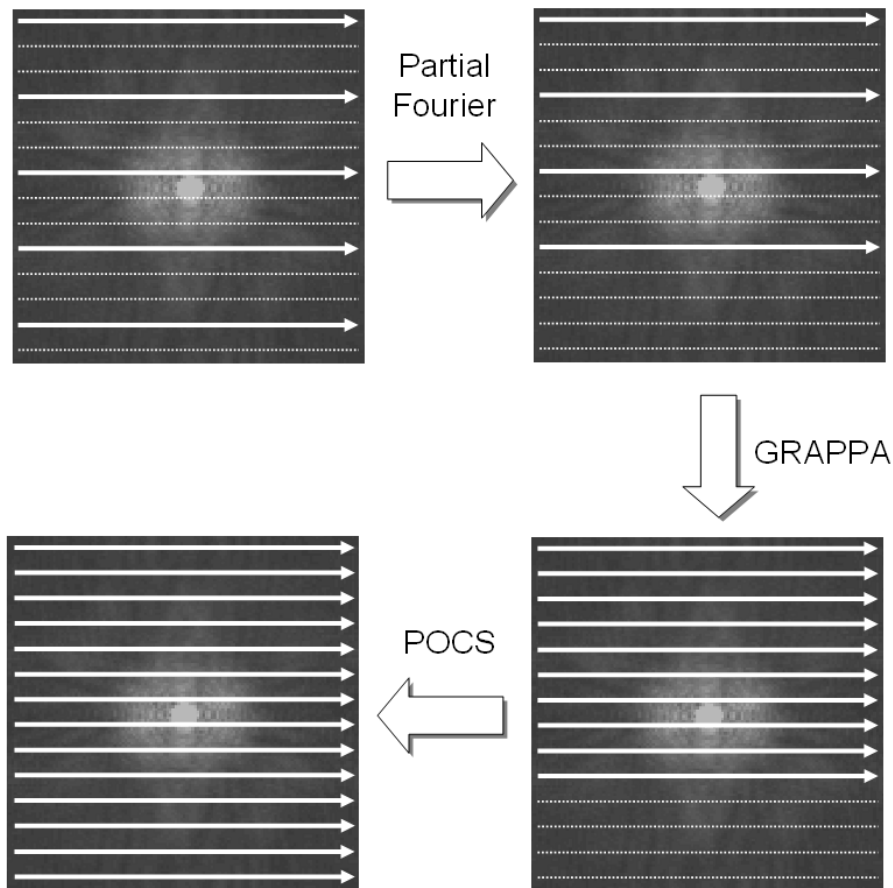
Figure 3.2:   Schematic description of the partial Fourier parallel imaging reconstruction procedure. Starting from conventional accelerated (parallel reduction factor: $R = 3$) acquisition (top left) the k-space is additionally reduced by the partial Fourier factor ($pf = 0.75$) yielding an asymmetric undersampled k-space (top right). In the first reconstruction step GRAPPA is performed yielding a fully sampled asymmetric partial Fourier k-space. In the final iterative reconstruction step the missing data can be calculated by exploiting inherent k-space symmetry and low resolution phase information (POCS) [45].
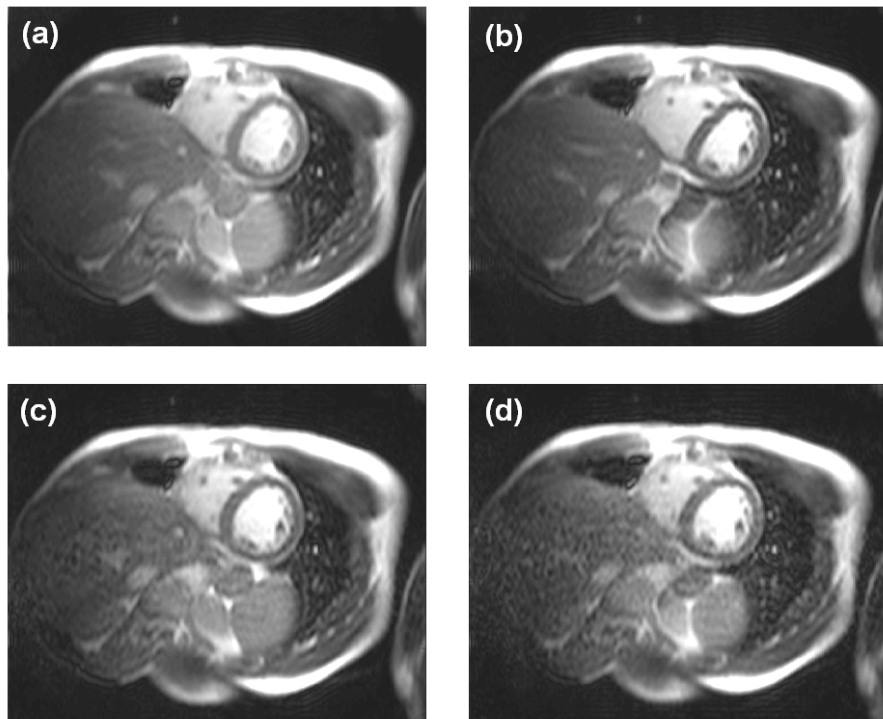
Figure 3.3: Example images after GRAPPA reconstruction for acceleration rates of (a) $R = 1$ (unaccelerated) (7.5 *fps*), (b) $R = 2$ (15 *fps*), (c) $R = 3$ (22.5 *fps*) and (d) $R = 4$ (30 *fps*) under normal breathing conditions are shown. The coil weighting coefficients for the GRAPPA reconstructions were derived from 6 ($R = 2$), 9 ($R = 3$), and 12 ($R = 4$) neighboring time frames. This figure is reprinted from reference [43].
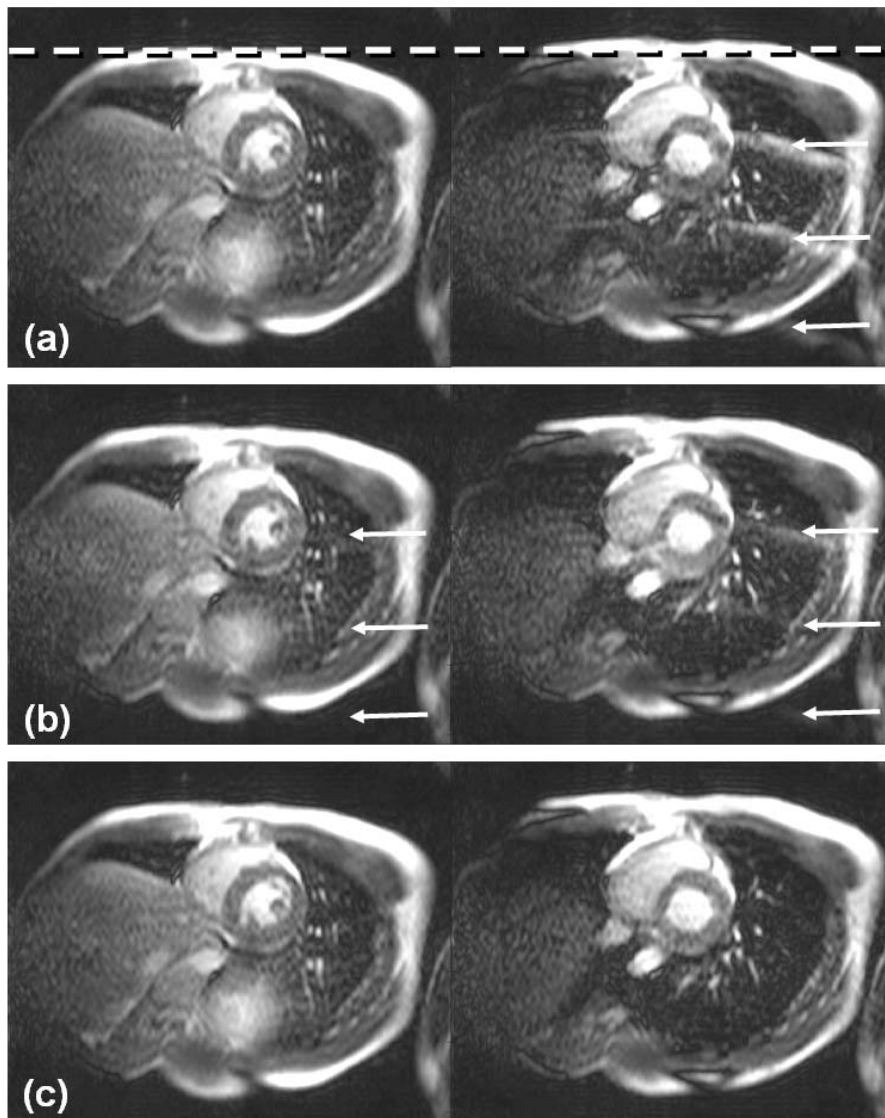
Figure 3.4: Illustration of the influence of inaccurate sensitivity information on a successful PPA reconstruction. For demonstration purposes, two time frames (Frame 5, Frame 151) are shown from an accelerated ($R = 4$) real-time TrueFISP non breath-held dynamic cardiac imaging experiment with a temporal resolution of 30 frames per second. The image reconstructions were performed using the GRAPPA algorithm with reconstruction weights calculated (a) only once at the beginning of the series, (b) only once by integrating all the data acquired during the whole series and (c) dynamically updated during the series. This figure is reprinted from reference [43].

age reconstructions were performed using the GRAPPA algorithm with reconstruction weights calculated (a) only once at the beginning of the series (first 12 frames) (b) only once by integrating all the data acquired during the whole series and (c) dynamically updated during the time series (12 neighboring frames). This example shows that respiratory motion can significantly change the position of the flexible coil array, resulting in residual artifacts in time frames where the reference data for coil calibration do not match the actual coil position. These artifacts disappear if the reconstruction parameters are updated dynamically for each time frame. The benefit of having full-resolution reference data for the normal GRAPPA reconstruction is demonstrated in Fig. 3.5. $R = 4$ undersampled images after a standard GRAPPA reconstruction using different number of ACS lines for coil calibration are shown. The image quality suffers significantly with decreased number of ACS lines. In this case, a block of at least 32 ACS lines is necessary to provide acceptable image quality. Since normal auto-calibrated GRAPPA requires additional ACS lines to be acquired for each frame during an exam where the reconstruction weights must be dynamically updated, the effective acceleration rate for this example would be reduced from rate $R = 4$ to approximately $R = 1.6$. In contrast, the TGRAPPA approach does not require additional reference data, thereby providing full image acceleration.

Fig. 3.6 demonstrates that an additional partial Fourier reduction of 25% (ie partial Fourier factor $pf = 0.75$) can be used to further increase imaging speed from 21 $fps \rightarrow 30\,fps$ at a parallel imaging reduction factor $R = 3$ (a)$\rightarrow$(b) and from 30 $fps \rightarrow 40\,fps$ at $R = 4$ (c)$\rightarrow$(d) without visible degradation of image quality. Comparing reconstruction quality from images (b) and (c) acquired at the same frame rate (30 fps) one can see that it is advantageous to apply the partial Fourier concept, especially when already operating at the limit of parallel imaging reduction.

3.4 Discussion

Temporal GRAPPA (TGRAPPA) is easy to implement and has been presented as an efficient method for improving reconstruction quality in dynamic parallel imaging. TGRAPPA was successfully applied to real-time, non-gated, free-breathing dynamic cardiac imaging. It has been shown that TGRAPPA reconstructions result in excellent image quality without any residual artifacts up to frame rates of $30\,fps$, even when the coil positions change significantly during the acquisition. PPA reconstruction with GRAPPA is particularly beneficial in applications where accurate coil sensitivity maps may be difficult to obtain [15]. For example, a precise estimation of spatial coil sensitivities may be difficult in inhomogeneous regions with low spin density such as the lung and the abdomen. TGRAPPA provides a means of eliminating the overhead required for acquiring additional ACS lines. In this example with 60 phase encode lines and $R = 4$ undersampling, if 32 ACS lines were required, the effective
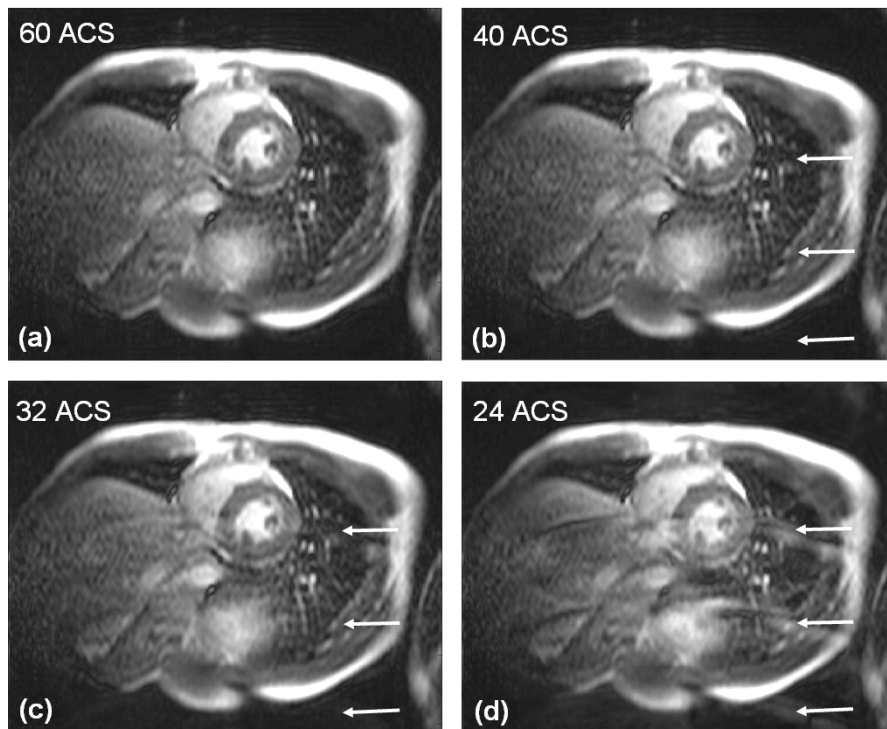
Figure 3.5: $R = 4$ undersampled example images after GRAPPA reconstruction using (a) 60 ACS lines (full spatial resolution), (b) 40 ACS lines (c) 32 ACS lines and (d) 24 ACS lines as reference data. The image quality improves significantly with an increased number of ACS lines. Residual aliasing artifacts are visible even with 40 ACS lines as reference data. This figure is reprinted from reference [43].
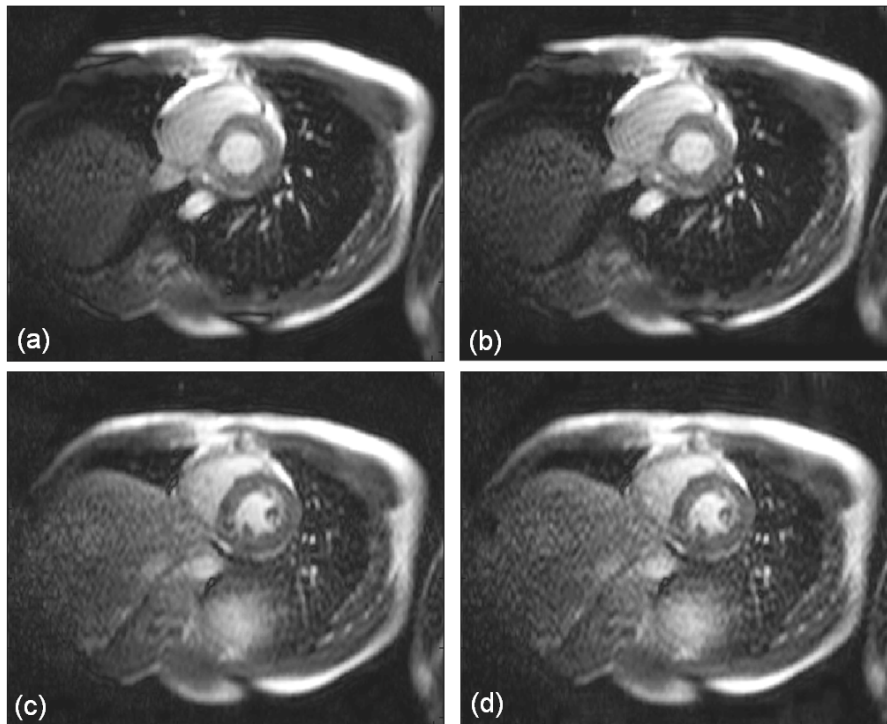
Figure 3.6: TGRAPPA reconstructions without partial Fourier reduction (a) $R = 3$ (21 *fps*) and (c) $R = 4$ (30 *fps*) and with additional $pf = 0.75$ partial Fourier reduction (b) $R = 3$ (30 *fps*) and (d) $R = 4$ (40 *fps*). These reconstruction results demonstrate that the concept of partial Fourier acquisition can be additionally exploited without visible degradation of image quality.

acceleration rate would be reduced from rate $R = 4$ to approximately rate $R = 1.6$. Furthermore, the TGRAPPA approach benefits from having the coil sensitivity maps with full spatial resolution, which offers improved artifact suppression.

A frame-to-frame update of the reconstruction coefficients can require a long total reconstruction time. However, the high frame rate may allow one to update the reconstruction coefficients much less frequently, since coil motion caused by respiration occurs more slowly than the actual frame rate of 30 *fps*. Once the reconstruction coefficients are calculated for one frame, they can be used to reconstruct multiple subsequent frames in the series in a short time. During this time, new coil coefficients can be calculated to reconstruct later frames in the series. This adapted concept results in a significantly improved over-all reconstruction time, without visible degradation of image quality [46]. This concept, in combination with a highly optimized GRAPPA algorithm, would be a promising technique for true real-time on-the-fly image reconstructions. Additionally, as it has been shown, a combination of TGRAPPA and partial Fourier acquisition can further increase imaging speed without significantly degrading image quality or be used to improve image quality at a constant frame rate.

3.5 Summary

TGRAPPA is an efficient method for dynamic parallel imaging. The technique combines a time-interleaved acquisition scheme with auto-calibrated GRAPPA. No additional reference data must be acquired, since the signal from directly adjacent time frames can be merged to form a set of fully-encoded full-resolution reference data for coil calibration, thereby realizing full image acceleration. The coil coefficients for the GRAPPA algorithm can be easily updated dynamically, thereby tracking changes in relative coil sensitivities during the data acquisition which may occur due to respiratory motion. TGRAPPA reconstructions of accelerated ($R = 2$ to $R = 4$) real-time (non-gated), free-breathing cardiac studies were presented with excellent image quality and without any visually apparent residual artifacts up to frame rates of 30fps. This method compensates efficiently for significant changes in coil position due to respiratory motion.

Chapter 4

Controlled Aliasing in Simultaneous Multislice Parallel Imaging (MS CAIPIRINHA)

4.1 Introduction

Introduction to CAIPIRINHA

In Chapter 2, today's most important partially parallel acquisition (PPA) strategies have been introduced. All of them utilize the spatial information inherent in an array of multiple radio frequency (rf) receiver coils positioned around the object of investigation to partially replace time consuming spatial encoding with magnetic field gradients. To speed up acquisition, the number of phase encoding steps is reduced by uniformly increasing the distance between adjacent acquired lines in k-space. As already described, this undersampling of Cartesian k-space leads to distinct aliasing artifacts which can later be removed by the PPA reconstruction process. Since parallel imaging is generally limited to applications with an adequate signal to noise ratio (SNR), it is preferable to combine the parallel imaging concept with imaging techniques which have intrinsically high SNR, such as volumetric imaging methods. Recently, the parallel imaging concept has been successfully extended to such methods [47, 48]. Besides the gain in SNR due to volume excitation, these methods have been shown to further improve image quality because they exploit sensitivity variations in multiple directions, thereby yielding improved geometry factors. However, both parallel imaging approaches are limited by the fact that the performance of these techniques is strongly dependent on the geometry of the coil array. In this chapter, a new concept, Controlled Aliasing In Parallel Imaging Results IN Higher Acceleration (CAIPIRINHA) [49, 50], is presented which modifies the appearance of aliasing artifacts during the data acquisition in order to reduce the dependence of the parallel imaging technique on the underlying array geometry. These modifications are achieved by

exploiting properties of sampling theory as described earlier in Chapter 1. These modifications result in an improved parallel imaging reconstruction procedure because sensitivity variations provided by the underlying coil array are more efficiently exploited. During the last years of my thesis, the concept of CAIPIRINHA has been successfully applied to volumetric imaging methods, such as simultaneous multi-slice imaging [51] and 3D imaging [52]. These techniques are introduced and discussed in the following chapters. In an additional chapter, it will be shown that the concept of CAIPIRINHA can also be applied to the remaining third spatial dimension.

Introduction to MS CAIPIRINHA

In the past, several techniques using simultaneously excited multiple slices which do not use PPA have been shown to improve the SNR per slice by a factor $\sqrt{NS}$, where NS denotes the number of simultaneously excited slices. In general, all of these techniques either require NS-fold more phase encoding steps (e.g. Phase Offset Multi Planar (POMP)) [53] or multiple subsequent excitations [54, 55, 56] to fully differentiate all slices. The previously reported conventional simultaneous multi-slice parallel imaging approach [48] is limited by the fact that it suffers from reduced SNR whenever the coil array sensitivies are substantially similar in the excited slices, which is usally the case for closely spaced slices. In this chapter, MS CAIPIR-INHA is described and how it is more efficient compared to other multi-slice parallel imaging concepts. Multiple slices of arbitrary thickness and distance are excited simultaneously using alternating multi-band RF pulses similar to Hadamard pulses. Simultaneous excitation of multiple slices leads to superimposed slices. However, these slices can be shifted with respect to each other. These shifts are controlled by modulating the phase of the individual slices in the multi-band excitation pulse from echo to echo. Using this shift, coil sensitivity variations in multiple dimensions may be exploited more efficiently compared to conventional multi-slice techniques, resulting in better image quality. This can potentially allow one to use higher acceleration factors compared to techniques that do not employ this excitation scheme. Even superimposed slices which have essentially the same coil sensitivies can be separated with this technique. Image reconstructions are performed with the SENSE [23] algorithm using adapted sensitivity information to account for the shifted slices. However, the flexibility of this approach allows one to use other parallel imaging techniques such as GRAPPA [27] as well.

4.2   Theory

Conventional multi-slice imaging

In order to fully understand the basics of the MS CAIPIRINHA [51] approach and how it is different from previous methods, this chapter starts with a review of the basic parallel imaging

procedures and how they can be applied to multi-slice acquisitions. In principle, the parallel imaging concept provides a way to separate multiple image signals which are aliased into one image pixel by means of the sensitivity information inherent in the receiver array. The SENSE approach uses the knowledge of the spatial sensitivity information of each coil in the receiver array to perform this separation in the image domain using a pixel by pixel matrix inversion (see section 2.4). If one assumes a two-fold scan time reduction ($R = 2$) for a normal single slice acquisition with a two-coil receiver array, each pixel in the component coil images will then be composed of a superposition of two spin densities weighted with their spatial sensitivity information at the corresponding positions. As demonstrated in Chapter 2, these relations can easily be seen in matrix form and can be solved by a simple matrix inversion of the so-called sensitivity matrix $\hat{C}$ (Eq. 2.2 and Eq. 2.3).

In simultaneous multi-slice imaging, a scan-time reduction can also be performed in the slice direction while exploiting the parallel imaging concept ([47]). However, when the scan time is reduced simultaneously in two dimensions, the SENSE algorithm (Eq. 2.2) must be rewritten so that it matches the 2D problem. If an accelerated ($R = 2$) simultaneous two-slice experiment ($NS = 2$) is assumed (where two slices are acquired in the time normally needed to acquire one slice), the normal SENSE equation is extended to the multi-slice SENSE equation by substituting the appropriate component coil pixels (I_1 & I_2), which are now a superposition of spin densities originating from two different slices (ρ_1 & ρ_2) weighted with their spatial sensitivity information (C_{11} & C_{12}, C_{21} & C_{22}). The sensitivity matrix is then composed of the spatial sensitivity information from each coil (first index) and slice (second index) at the in-plane spatial location (x,y).

$$\left(\begin{array}{c} I_1(x,y) \\ I_2(x,y) \end{array} \right) = \left(\begin{array}{cc} C_{11}(x,y) & C_{12}(x,y) \\ C_{21}(x,y) & C_{22}(x,y) \end{array} \right) \cdot \left(\begin{array}{c} \rho_1(x,y) \\ \rho_2(x,y) \end{array} \right) \tag{4.1}$$

Again, this set of linear equations can be solved using a simple matrix inversion. In general, all parallel imaging methods are limited by the fact that aliased pixels must have sufficient sensitivity variations to perform this inversion. This is a crucial point for simultaneous multi-slice imaging in combination with PPA. In multi-slice imaging, insufficient sensitivity variations in slice direction can easily occur due to the inherent coil geometry or because the slices are close together. Mathematically expressed, if the coil sensitivity values of aliased pixels are nearly identical ($C_{11} \approx C_{12}$ and $C_{21} \approx C_{22}$), the linear equation system of Eq. 4.1 cannot be solved even when the individual coils have different sensitivity information in the phase encoding direction.

Controlled aliasing in multi-slice imaging

The central concept of MS CAIPIRINHA is that the situations described above can be avoided by shifting the aliasing patterns of the multiple slices with respect to each other, thereby
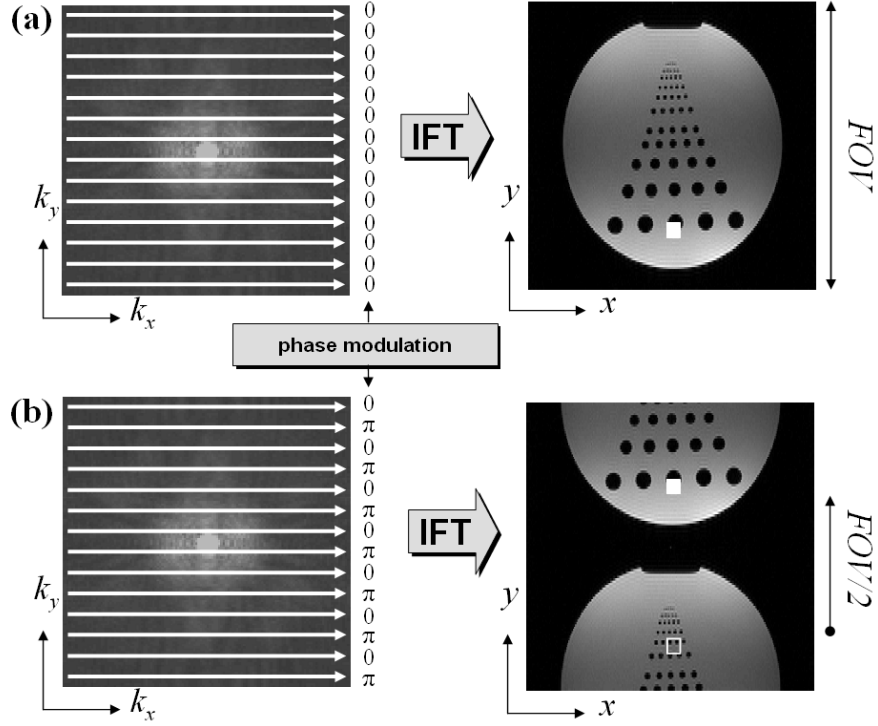
Figure 4.1: Acquisition scheme (left) with (a) no phase modulation in phase encoding direction and the corresponding phantom image after inverse Fourier transformation (IFT) (right). In comparison, the acquisition scheme (b) with phase modulation in phase encoding direction $(0, \pi, 0, \pi, 0, \pi)$ is shown. After IFT (right), the image is shifted (indicated by the arrow) by $FOV/2$ in phase encoding direction according to the phase cycle.

providing a more readily invertible system of equations. The key element of this approach is the modification of aliasing patterns in a controllable way. This can easily be realized by, for example, exploiting the basic Fourier shift theorem (see subsection 1.4.3). A shift in the image domain by Δy can mathematically be realized by multiplying the k-space signal by a Δy-dependent linear phase factor with phase

$$\Phi_m = -m\Delta k \Delta y \quad \text{with} \quad m = -n, -n+1, ..., n-1 \tag{4.2}$$

For example, to shift the image by one single pixel ($\Delta y = FOV/N$), a linearly decreasing phase running from $(+\pi)$ to $(-\pi)$ is required ($\Phi_m = -2\pi\frac{m}{N}$), where $N = 2n$ denotes the number of phase encoding steps. Similarly, a shift of exactly $\Delta y = FOV/2$ requires an alternating phase $(0, \pi, 0, \pi, 0, \pi)$ as a result of the periodicity of the harmonic ($\Phi_m = -\pi m$). In practice, these phase modulations can be realized by an RF excitation with varying pulse phases according to the required phase modulations. Fig. 4.1 depicts a simple example where a shift in the phase encoding direction by $FOV/2$ is performed using RF pulses with alternating pulse phases.

To influence the aliasing conditions in simultaneous multi-slice imaging, this basic idea to shift the individual slices with respect to each other is exploited. This can be accomplished during the excitation using special phase modulated multi-slice RF pulses. For example, a conventional simultaneous two-slice excitation without phase modulation will result in an image composed of two superimposed slices and as a result of the Fourier transformation of the simultaneously received signals (S_1 & S_2) originating from the individual slices.

$$\rho(y) = \sum_{m=-n}^{n-1} (S_1(m\Delta k) + S_2(m\Delta k)) \cdot e^{im\Delta ky} = \rho_1(y) + \rho_2(y) \tag{4.3}$$

In comparison, a simultaneous two-slice excitation with an additional phase modulation applied only to Slice 2 will also result in an image composed of two superimposed slices, but shifted with respect to each other by Δy:

$$\rho(y) = \sum_{m=-n}^{n-1} (S_1(m\Delta k) + S_2(m\Delta k) \cdot e^{-im\Delta k\Delta y}) \cdot e^{im\Delta ky} = \rho_1(y) + \rho_2(y - \Delta y) \tag{4.4}$$

In Fig. 4.2, a simple simultaneous two-slice experiment is shown (a) without phase modulation (identical phase cycles for the individual slices), resulting in a total overlap of both slices and (b) with phase modulation (different phase cycles for individual slices), resulting in slices shifted with respect to each other. In general, this two-slice example can be extended to more slices, where each slice can be shifted independently by an arbitrary amount in the FOV by applying different phase cycles to the individual slices according to the Fourier shift theorem. To shift individual slices in such a way as to distribute them equidistantly in the FOV, the composite signal S at position $m\Delta k$ must be composed of the sum of the signals S_l originating from the individual slices, simultaneously excited. Additionally, each band of the pulse at the phase encoding step m must be excited with a specific phase factor according to the number of simultaneously excited slices NS. This can be performed using, for example, POMP-type phase cycles [53].

$$S(m\Delta k) = \sum_{l=1}^{NS} S_l(m\Delta k) \cdot e^{i(m-1)(l-1)\frac{2\pi}{NS}\Delta k} \tag{4.5}$$

After Fourier transformation, the centers of the simultaneously excited slices are shifted equidistantly in the phase encoding direction with respect to each other by a slice-dependent amount $\Delta y(l)$ for a given FOV:

$$\Delta y(l) = (l-1) \cdot \frac{FOV}{NS} \qquad l = 1, ..., NS \tag{4.6}$$

This relationship is illustrated in Fig. 4.3 for a two-slice experiment, depicting the resulting shifts for different FOVs. To fully differentiate all simultaneously excited NS slices using a
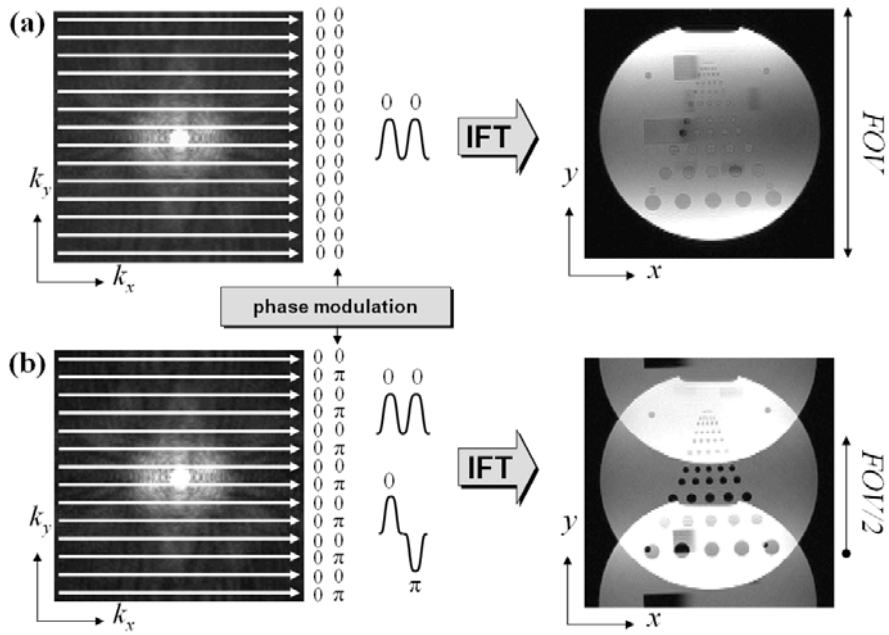
Figure 4.2: Schematic description of a simultaneous two-slice phantom experiment (a) without phase cycling (left) and the corresponding image with totally overlapping slices (right). (b) Simultaneous two-slice experiment with different phase cycles in the phase encoding direction applied to the individual slices (Slice 1: $(0, 0, 0, 0, 0, 0)$, Slice 2: $(0, \pi, 0, \pi, 0, \pi)$). This is performed by means of RF excitation with special alternating dual-band pulses. Odd k-space lines are the result of a dual-band excitation pulse with the same phase for both slices $(0, 0)$. Even k-space lines are the result of a dual-band excitation with different phases for both slices $(0, \pi)$. After inverse Fourier transformation, the individual slices are still superimposed but shifted by $FOV/2$ with respect to each other.
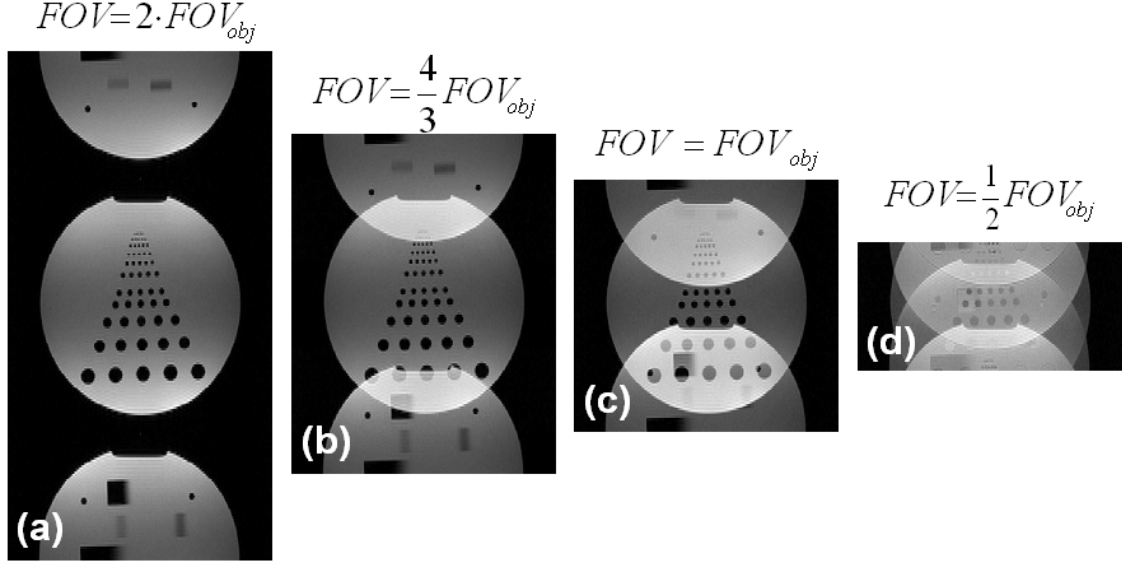
Figure 4.3: Images after simultaneous excitation of two slices employing alternating dual-band pulses as described in Fig.4.2 with (a) $FOV = 2 \cdot FOV_{obj}$ (reduction factor $R = 1$) (POMP), (b) $FOV = \frac{4}{3} \cdot FOV_{obj}$ ($R = 1.5$), (c) $FOV = FOV_{obj}$ ($R = 2$), (d) $FOV = \frac{1}{2} \cdot FOV_{obj}$ ($R = 4$). In all cases Slice 1 appears in the center of the resulting image (FOV-independent), while Slice 2 is shifted by $FOV/2$ with respect to Slice 1. A FOV which is smaller than the object results in an additional in-plane aliasing artifact (d). This figure is reprinted from reference [51].

POMP-type phase cycle without parallel imaging, the FOV in the phase encoding direction must be at least $FOV \geq NS \cdot FOV_{obj}$. This can be seen in Fig. 4.3a. Here, FOV_{obj} specifies the size of the object in the phase encoding direction. A uniformly undersampled k-space with a reduced number of phase encoding steps will result in a reduced FOV_R, which is given by:

$$FOV_R = NS \cdot \frac{FOV_{obj}}{R} \tag{4.7}$$

With an increased reduction factor R, the resulting FOV_R decreases, thereby resulting in a larger overlap of the individual slices.

Considering the effect of the induced shift of $FOV/2$ on the second slice in the two-slice example given above, the SENSE equation can be rewritten for MS CAIPIRINHA reconstructions. The aliased images, and therefore the coil sensitivity map and matrix for the second slice in Eq.4.1, now include a spatial shift in the y-direction due to the phase-modulated RF pulses:

$$\begin{pmatrix} I_1(x,y) \\ I_2(x,y) \end{pmatrix} = \begin{pmatrix} C_{11}(x,y) & C_{12}(x,y+\frac{FOV}{2}) \\ C_{21}(x,y) & C_{22}(x,y+\frac{FOV}{2}) \end{pmatrix} \cdot \begin{pmatrix} \rho_1(x,y) \\ \rho_2(x,y+\frac{FOV}{2}) \end{pmatrix} \tag{4.8}$$

In general, the coil sensitivities will tend to be more different in this situation, since now the
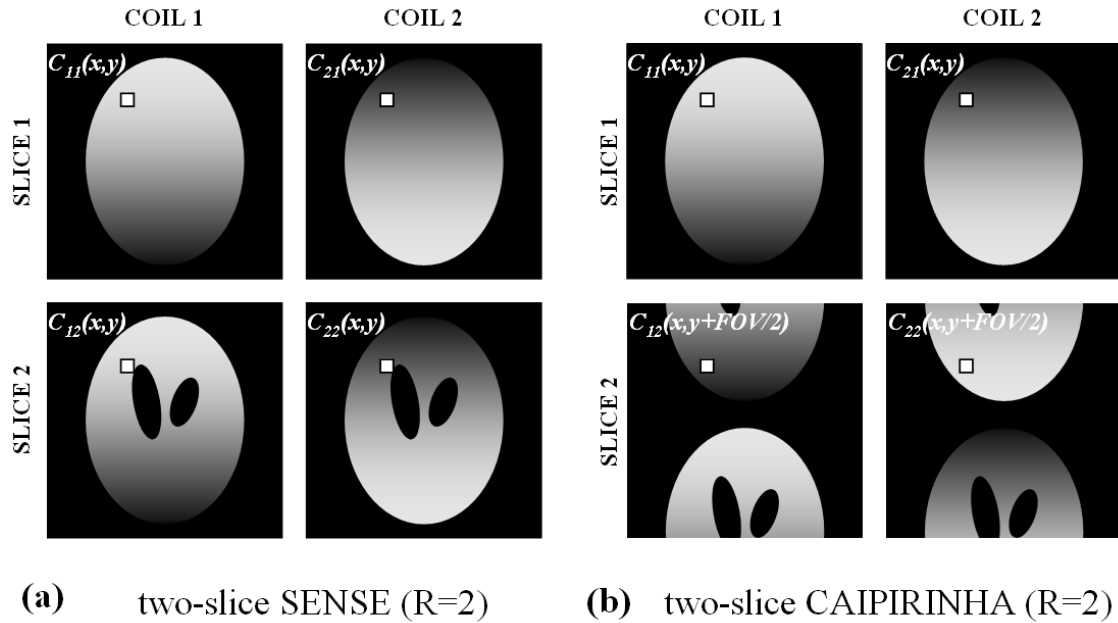
Figure 4.4: Sensitivity maps of two slices provided with identical coil sensitivity profiles. Aliased sensitivity information of an accelerated ($R = 2$) (a) normal two-slice SENSE experiment with $C_{11} = C_{12}$, $C_{21} = C_{22}$ at every position (x,y) and (b) a two-slice CAIPIRINHA experiment with $C_{11} \neq C_{12}$, $C_{21} \neq C_{22}$ at every position (x, y). This figure is reprinted from reference [51].

parallel imaging reconstruction can exploit sensitivity variations in both the phase and slice encoding direction. Thus, in most cases, the inverse of the modified matrix will exist, even in those cases where the coil sensitivities would have been the same at the two slice locations. This extreme case is schematically shown in Fig. 4.4. A normal simultaneous two-slice SENSE acquisition (Fig. 4.4a) will result in this case for aliased pixels which have exactly the same coil sensitivities, while a two-slice CAIPIRINHA-type acquisition (Fig. 4.4b) will guarantee different sensitivities for aliased pixels. As shown below, this can result in improved SNR and better PPA reconstructions as compared to non-CAIPIRINHA acquisitions.

Signal to noise considerations

A measure of how easily the matrix inversion in SENSE can be performed is the geometry factor g, which has been described in Eq. 2.4. As already mentioned, the g-factor describes how well aliased pixels can be separated with a given receiver coil configuration. It has been shown that the g-factor allows one to estimate the local noise enhancement and therefore the final SNR distribution in the SENSE reconstructed image. Using a CAIPIRINHA-type acquisition a potential SNR benefit may be achieved by means of two independent mechanisms:

- The SNR increases with the square-root of the number of simultaneously excited slices as compared to sequential multi-slice imaging.

- The SNR increases due to a decreased geometry related noise enhancement (improved g-factor) compared to MS SENSE.

After taking these mechanisms into account, the final SNR using multi-slice CAIPIRINHA can be expressed as

$$SNR_{CAIPIRINHA} = \sqrt{NS} \cdot \frac{SNR_{full}}{g_{CAIPIRINHA} \cdot \sqrt{R}} \tag{4.9}$$

Eq. 4.9 outlines the key role of the geometry factor in the multi-slice CAIPIRINHA approach. In contrast to conventional multi-slice SENSE, where the g-factor is mainly determined by the arrangement of the element coils, the g-factor may additionally be affected by the phase modulations in CAIPIRINHA.

4.3   Material and Methods

The MS CAIPIRINHA technique was implemented on a $1.5\,T$ whole body MR scanner (Vision, Siemens Medical Solutions, Erlangen, Germany), equipped with a standard four coil body array for signal reception with two anterior elements positioned in the head-foot direction and two posterior elements also positioned in the head-foot direction. Several volunteers were examined and informed consent was obtained before each study. For imaging, a modified FLASH sequence was used with the following parameters: $TR = 10\,ms$, $TE = 4\,ms$, $\alpha = 30°$, $FOV = 37.5\,cm \times 50\,cm$, matrix $= 192 \times 256$, slice thickness $= 10\,mm$, gap $= 5\,mm$. As described above, the conventional excitation pulse was replaced by alternating multi-band RF pulses with varying phase modulations in each phase encoding step in order to provide the individual slices with different phase cycles according to Eq. 4.5. These phase modulated multi-slice RF-pulses were generated based on the Shinnar-Le Roux transformation, involving a phase correction that provided control over the phase of the individual slices, as described by Cunningham et al [57]. In this implementation, two to four slices were excited simultaneously. Acquisitions were performed with reduction factors from $R = 2$ to $R = 4$. Image reconstruction was performed off-line using the Matlab programming environment (The Mathworks, Natick, MA, USA). For comparison, PPA-reconstructions were performed with the SENSE algorithm, using adapted coil sensitivity maps which were derived with an additional, full FOV reference scan.

Additionally, computer simulations were performed to further investigate the properties of MS CAIPIRINHA. To this end, a standard 16-channel receiver head coil which provided sensitivity variations in slice direction was simulated. The array was made up of two cylindrical 8 coil-rings in head-foot direction with $2\,cm$ overlap as shown in Fig. 4.5. The total coil dimensions were $28\,cm$ length and $28\,cm$ diameter. Coil sensitivity maps were calculated at equidistant $1\,cm$ intervals in the slice direction starting in the middle of one ring and ending in the middle of the second ring. The calculations were done in Matlab exploiting analytical

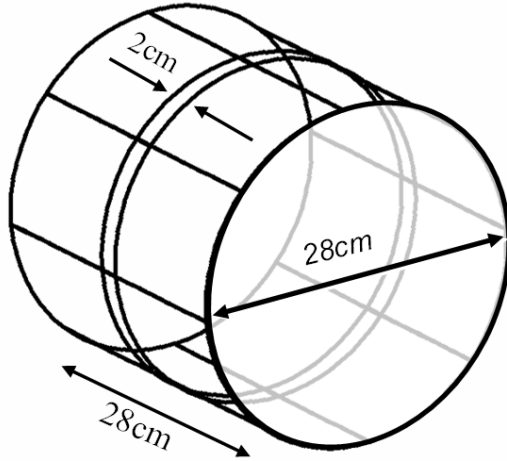Biot Savart integrations to simulate coil sensitivities.

Figure 4.5: Simulated standard 16 channel receiver head coil with sensitivity variations in the slice direction. The array is composed of two cylindrical 8 coil-rings in the head-foot direction with a $2\,cm$ overlap. The total coil dimension was chosen to be $28\,cm$ length and $28\,cm$ diameter. This figure is reprinted from reference [51].

4.4 Results

As a reference, Fig. 4.6a shows the unaccelerated POMP ($R = 1$) images of two simultaneously excited directly adjacent (gap $5\,mm$) slices in the abdomen of a volunteer. Fig. 4.6b shows a conventional (without phase modulation (Fig. 4.2a)) accelerated ($R = 2$) simultaneous two-slice acquisition after inverse Fourier transformation. The result is a total overlap of the two individual slices. In contrast, using an accelerated ($R = 2$) two-slice CAIPIRINHA-type acquisition scheme (with phase modulation (Fig. 4.2b)) the superimposed slices are shifted by $FOV/2$ with respect to each other (Fig. 4.6c). Fig. 4.7a shows the final images after a SENSE reconstruction applied to the conventional reduced data without phase modulation (Fig. 4.6b). As can be seen, the geometry factor approaches infinity, because the coil sensitivities are essentially identical in the two slices, as the gap between the slices is only $5\,mm$. In contrast, Fig. 4.7b depicts the separated images after a two-slice CAIPIRINHA acquisition with phase modulation (Fig. 4.6c) in combination with the SENSE reconstruction using adapted reordered coil sensitivities according to the $FOV/2$ shift of the second slice. In this case, the slices can be more easily resolved due to the additional shift provided by the CAIPIRINHA acquisition scheme. The geometry factor in this case was close to one for all pixels in the image, therefore providing essentially the same SNR twice as fast compared to a normal sequential acquisition without parallel imaging. It is clear that the normal multi-slice SENSE images of Fig. 4.7a represent a worst-case scenario for image reconstruction. In this case, one would have obtained substantially better images using only in-plane acceleration. However, these normal in-plane SENSE images would have at least a factor of $\sqrt{2}$ lower SNR compared to the multi-slice CAIPIRINHA approach.
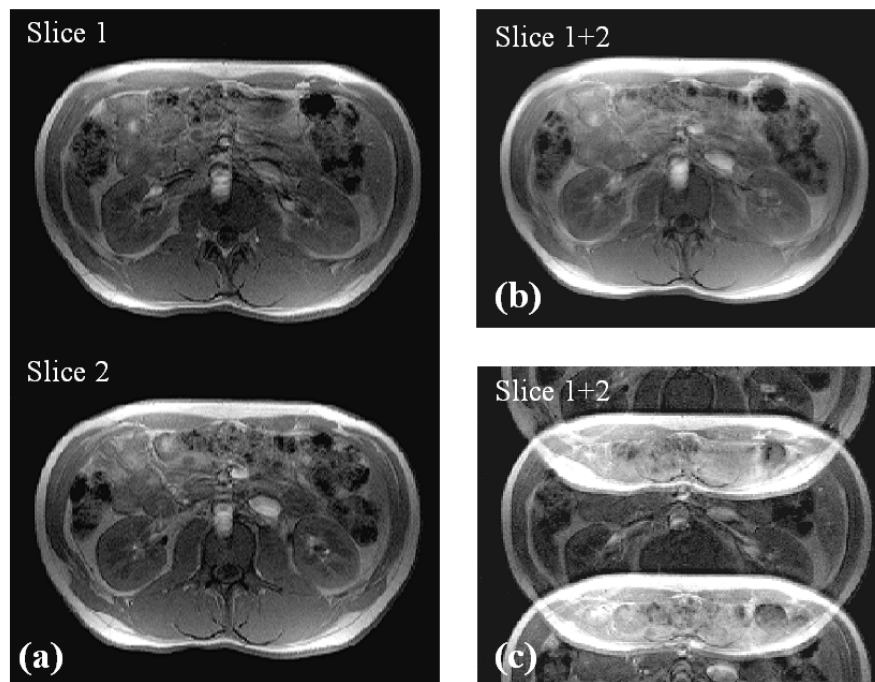
Figure 4.6: (a) Unaccelerated ($R = 1$) POMP reference image of two simultaneously excited directly adjacent (gap $5\,mm$) slices in the abdomen of a volunteer. (b) Conventional two-slice SENSE experiment without phase cycling after inverse Fourier transformation. Two slices are aliased directly on top of each other. (c) Two-slice CAIPIRINHA experiment ($R = 2$) using different phase cycles for the individual slices (Slice 1: $0, 0, 0, 0, 0$ Slice 2: $0, \pi, 0, \pi, 0, \pi$) after inverse Fourier transformation. The individual slices are still superimposed but shifted by $FOV/2$ with respect to each other. This figure is reprinted from reference [51].
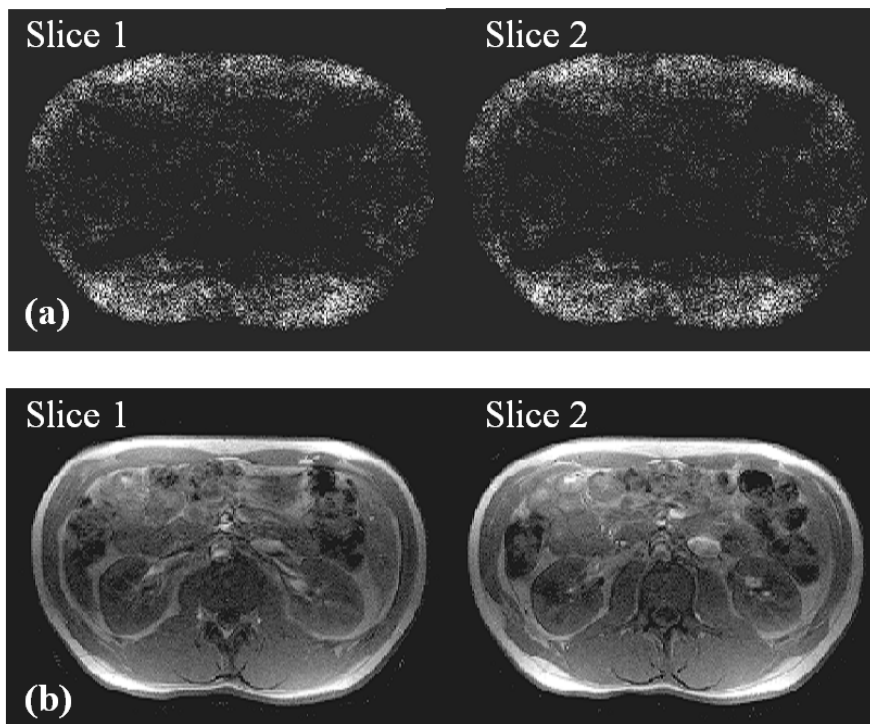
Figure 4.7: Separated images (Slice 1, Slice 2) after SENSE reconstruction of an accelerated ($R = 2$) (a) conventional two-slice experiment without phase cycling and a (b) two-slice CAIPIRINHA experiment ($R = 2$) using different phase cycles for the individual slices (Slice 1: $0, 0, 0, 0, 0$ Slice 2: $0, \pi, 0, \pi, 0, \pi$). This figure is reprinted from reference [51].
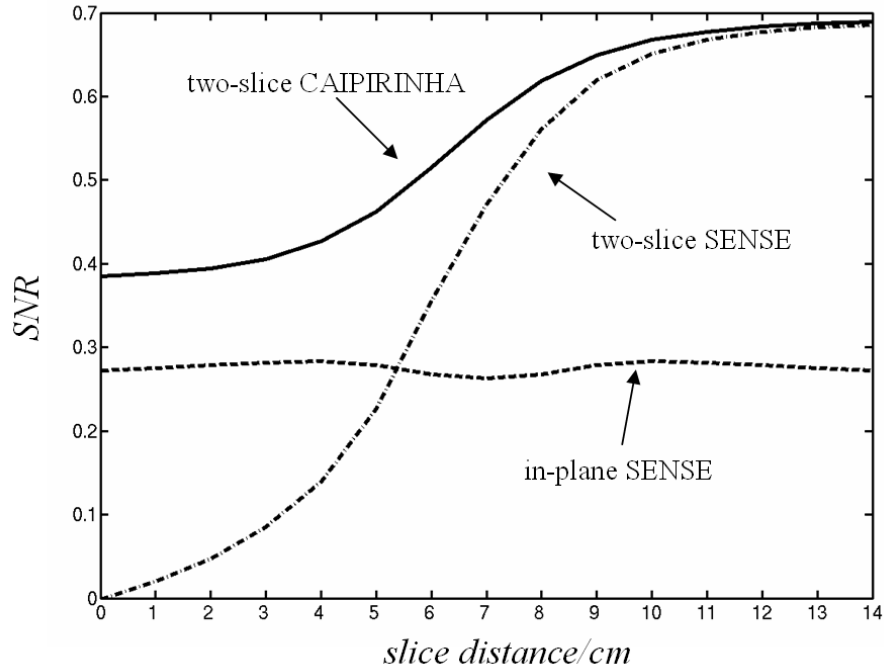
Figure 4.8: SNR performance of accelerated ($R = 4$) normal in-plane SENSE, two-slice SENSE and two-slice CAIPIRINHA as a function of increased distance between the superimposed slices. The SNR is calculated according to Eq. 4.9, which takes the reduction factor R, the number of simultaneously excited slices NS, and the mean geometry-factor g into account. The SNR is given relative to an unaccelerated experiment which would take 4 times longer to acquire. This figure is reprinted from reference [51].

Simulations were performed in order to further demonstrate the advantages of MS CAIPIR-INHA compared to conventional multi-slice SENSE. To this end, the sensitivity characteristics of the simulated 16 channel two-ring head coil were exploited. Accelerated ($R = 4$) two-slice CAIPIRINHA and two-slice SENSE acquisitions were simulated with increasing distance between the two superimposed slices. The position of one slice was held constant in the middle of one ring, while the position of the second slice was moved toward the second ring in $1\,cm$ steps. Additionally, standard in-plane accelerated ($R = 4$) single-slice SENSE experiments were simulated at the same slice positions. For all three scenarios the mean and maximum geometry-factor was calculated at the positions of the second slice. This allows calculation of the SNR performance of all three techniques as a function of increased slice distance (corresponding to increased sensitivity variation in slice direction) as displayed in Fig. 4.8. The mean SNR of each slice was calculated according to Eq. 4.9 accounting for the reduction factor R, the number of simultaneously excited slices NS, and the mean geometry factor g. The SNR is given relative to a single-slice experiment without acceleration. Because there is no substantial sensitivity variation in the slice direction when the distance between the two

slices is small, the g-factor approaches infinity in two-slice SENSE. However, with increasing slice distance (increasing sensitivity variations), the SNR performance improves and reaches a maximum ($g \approx 1$) at large slice separations. Normal in-plane SENSE provides a constant performance for all slice positions, since this method does not exploit any available sensitivity variations in the slice direction. However, the SNR of normal in-plane SENSE is reduced by a factor of $\sqrt{NS}$, as this method is a single-slice excitation technique. In contrast, two-slice CAIPIRINHA starts with a reasonable SNR-performance even when the two superimposed slices are directly adjacent. In this extreme case of essentially no sensitivity variations in slice direction, the g-factor performance of in-plane SENSE and CAIPIRINHA is identical. However, due to the simultaneous two-slice acquisition, CAIPIRINHA provides a factor of $\sqrt{NS}$ better SNR. Similar to two-slice SENSE, the SNR-performance increases rapidly with increasing distance and approaches the same optimal performance at large slice separations.

4.5 Discussion

CAIPIRINHA has been presented as a means of improving the encoding efficiency in multi-slice parallel imaging. The properties of the novel technique were studied using simulations as well as phantom and *in vivo* studies. *In vivo* imaging was successfully performed with a two-fold scan time reduction of two simultaneously excited directly adjacent slices. It has been found that in the existing setup, multi-slice CAIPIRINHA was clearly superior as compared to standard sequential or simultaneous multi-slice parallel imaging techniques. In contrast to a normal sequential multi-slice acquisition, CAIPIRINHA benefits from the SNR gain of multiple simultaneously excited slices. Therefore, in principle, CAIPIRINHA provides a simultaneous acquisition of multiple slices in the same scan time as required for one single slice with the same basic SNR. However, the SNR is also affected by the geometry factor. In the worst case of no sensitivity variation in the slice direction, the resulting geometry factor is equal to the g-factor in normal single slice parallel imaging. However, any sensitivity variation in slice direction will always reduce the resulting g-factor and further improve the SNR performance of the CAIPIRINHA approach. In general, multi-slice CAIPIRINHA has the potential to exploit sensitivity variations along multiple dimensions simultaneously in a more efficient way than standard techniques. This leads to a more flexible and robust image reconstruction without a priori knowledge of the encoding efficiency of the coil array along multiple dimensions.

The multi-slice CAIPIRINHA approach provides a broad range of applications. Dynamic heart applications will directly benefit from the fast and simultaneous acquisition of multiple directly adjacent slices which have an SNR-value comparable to a single-slice acquisition. Multi-slice CAIPIRINHA has already been successfully applied to contrast enhanced heart perfusion and cine imaging [58].

In general, the multi-slice CAIPIRINHA approach is easy to implement, as long as the

specific absorption rate (SAR) and rf high voltage limits are not exceeded. This might limit application, in particular for SSFP-type acquisitions. Furthermore, with an increasing number of simultaneously excited slices, longer excitation times are required to minimize the disruption of slice profiles.

It is noteworthy that the MS CAIPIRINHA concept can be applied to all common imaging techniques (FLASH, RARE, EPI). Even sequences which already require special pulse phase cycles, such as TrueFISP, can be combined with MS CAIPIRINHA [59].

Additionally, parallel imaging reconstruction in MS CAIPIRINHA can be performed with any present PPA reconstruction algorithm (SENSE, SMASH, SPACE RIP, GRAPPA). All these algorithms require a modification of the coil sensitivity information either in image-space or in k-space according to the modified aliasing conditions. This adaptation can be done by either acquiring the required sensitivity information directly or by modifying the sensitivity information in a post-processing step. In a final reconstruction step, the result of the parallel imaging reconstruction procedure must be reordered according to the modified aliasing conditions and separated into the individual slices.

4.6 Summary

In all current parallel imaging techniques, aliasing artifacts resulting from an undersampled acquisition are removed by a specialized image reconstruction algorithm. In this work, a new concept, Controlled Aliasing In Parallel Imaging Results IN Higher Acceleration (CAIPIRINHA), has been presented which modifies the appearance of the aliasing artifacts during the acquisition to improve the following parallel image reconstruction procedure. Specifically, a new parallel multi-slice technique has been presented which is more efficient compared to other multi-slice parallel imaging concepts which use only a pure post-processing approach. In conclusion, CAIPIRINHA provides a new degree of freedom for parallel imaging by modifying aliasing artifacts during data acquisition in a controlled manner.

Chapter 5

Controlled Aliasing in volumetric parallel imaging (2D CAIPIRINHA)

5.1 Introduction

In conventional 2D imaging, parallel imaging is restricted to relatively small scan time reductions due to intrinsic limitations in the coil sensitivity variations along one phase encoding direction (1D parallel imaging) [16, 17]. In volumetric (3D) and simultaneous multi-slice imaging, parallel encoding can be carried out in two encoding directions (2D parallel imaging), thereby exploiting the sensitivity variations in both directions, as in, for example, 2D SENSE [47] and MS SENSE [48]. This concept has been shown to significantly improve the reconstruction conditions at a given acceleration factor. This results in improved image quality and allows one to achieve higher image accelerations. However, both techniques require sufficient sensitivity variations in two encoding directions for successful image reconstruction and therefore strongly depend on the underlying coil array geometry. In the previous chapter, it has been shown that these requirements in simultaneous multi-slice imaging can be partially overcome by shifting the individual slices with respect to each other in a controlled manner (MS CAIPIRINHA [51]). This is performed by excitation with alternating multi-band radio frequency (RF) pulses, similar to Hadamard pulses. In this chapter, an encoding strategy for 2D parallel imaging is presented, where the concept of CAIPIRINHA is applied to volumetric 3D imaging [60].

Besides the standard 2D SENSE sampling patterns, where rectangular undersampling is performed using simple integer reductions in each direction, many other patterns are conceivable where the sampling positions are shifted from their original positions in the 2D phase encoding scheme, as also proposed recently by others [61, 62, 63]. These shifts are attained by applying additional gradient offsets to the phase encoding gradient tables. In this study, 2D CAIPIRINHA [52] is presented, which modifies the appearance of aliasing in 2D parallel imaging by using these modified 2D phase encoding patterns. In the following it will be shown

that by shifting sampling positions in a well-directed manner, aliasing can be shifted in such a way that sensitivity variations provided by the underlying receiver array can be exploited more efficiently. These modified aliasing conditions then result in a further improvement in parallel imaging reconstruction conditions and therefore in better image quality. This is demonstrated in head and abdomen *in vivo* studies and computer simulations. Image reconstructions are performed using adapted SENSE and GRAPPA algorithms. However, other reconstruction algorithms such as SMASH or SPACERIP could be used as well.

With todays trend towards large coil arrays, the problem of determining a maximum acceleration given a specific coil configuration is becoming increasingly relevant. This is especially true in volumetric parallel imaging. For this reason, the concept of principal component analysis (PCA) is introduced, which applied to the coil array sensitivities (or reference data), allows one to estimate the maximum reduction factor. In addition, it will be shown that by applying the PCA in multiple dimensions separately, the maximum possible reduction factor in each dimension can be estimated. This analysis could provide a way to find the optimal CAIPIRINHA sampling pattern in volumetric parallel imaging.

5.2   Theory

A simple example

In order to clarify 2D parallel imaging and in particular to explain how aliasing can be controlled in 2D parallel imaging (2D CAIPIRINHA), a brief review of conventional unaccelerated 3D volume imaging is useful. In Fig. 5.1a, one sagittal partition taken from a fully-encoded 3D volume experiment is shown. The normal phase encoding direction is chosen to be in the anterior-posterior (AP) direction (y), the second phase encoding direction (partition encoding direction) in the left-right (LR) direction (z) and the frequency encoding direction in the head-foot (HF) direction (x). In order to better visualize how undersampling in two dimensions affects the appearance of aliasing, it is useful to switch from the sagittal to the transversal view (Fig. 5.1b). Now both phase encoding directions are displayed simultaneously in one plane. In Fig. 5.1c, a schematic depiction of the corresponding fully-encoded 2D sampling pattern is given, where each dot represents a phase-encoded read-out line. For illustration purposes, it is useful to start with a simple example of a twice undersampled parallel acquisition. In conventional 2D parallel imaging, given a reduction factor of $R = 2$, two different sampling patterns are possible. The reduction can either be performed only in the normal phase encoding direction ($R_y = 2$, $R_z = 1$), or only in the partition encoding direction ($R_y = 1$, $R_z = 2$). The resulting aliasing artifacts naturally appear only in the undersampled dimension.

In Fig. 5.2, both scenarios are shown in more detail. Besides schematics of both undersampled 2D acquisition schemes (Fig. 5.2, left), the corresponding 2D aliasing patterns are illustrated in the yz-plane showing a masked section of the head. Additionally, a single parti-
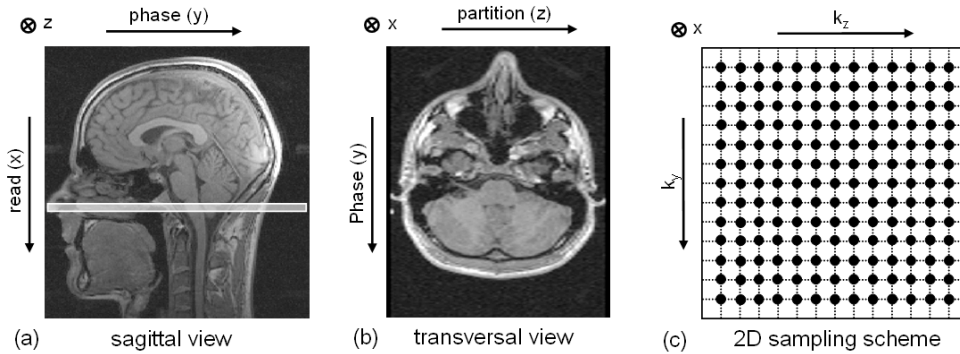
Figure 5.1: (a) One partition of a fully-encoded 3D imaging experiment is displayed in the sagittal view with normal phase encoding (phase) in the AP direction and frequency encoding (read) in the HF direction. The second phase encoding direction (partition) is in-plane in the LR direction. (b) In the transversal view, both phase encoding directions (phase and partition) can be displayed simultaneously in one plane. (c) Additionally, the corresponding fully-encoded 2D sampling pattern is displayed. Each dot represents a phase-encoded read-out line in the HF direction. This figure is reprinted from reference [52].

tion of each aliased data set, indicated by the vertical line, is shown in the sagittal view (Fig. 5.2, right). As can be seen, after a simple reduction by a factor of $R_y = 2$ in the normal phase encoding direction (Fig. 5.2a), each partition is aliased twice in the y-direction. On the other hand, using a simple reduction by $R_z = 2$ in the partition encoding direction (Fig. 5.2b), two partitions are superimposed directly on top of each other. This scenario corresponds to the two times accelerated ($R = 2$) simultaneous two-slice SENSE experiment (see Section 4.2), where both slices are also aliased directly on top of each other. However, another $R = 2$ undersampled sampling pattern is possible. For example, starting from the $R_z = 2$ case given in Fig. 5.2b, a pattern similar to the scheme given in Fig. 5.3 (left) can be generated by applying gradient offsets to every second gradient table in the phase encoding direction in order to shift the sampling positions exactly by Δk_z. The corresponding 2D aliasing (Fig. 5.3, middle) is different from the two former scenarios. In the sagittal view, the difference is obvious; the same partitions are superimposed directly on top of each other, but now they are shifted in the y-direction with respect to each other. This scenario is identical to the two-times accelerated ($R = 2$) simultaneous two-slice CAIPIRINHA experiment, where both slices are superimposed, but shifted with respect to each other in the phase encoding direction.

CAIPIRINHA sampling patterns in volumetric parallel imaging

With higher reduction factors, the number of possible 2D sampling patterns (SP) increases. In the following section, we restrict ourselves to sampling positions on a Cartesian grid. For simplicity, in Fig. 5.4 only an $R \times R$ section of the entire sampling scheme is shown, where R represents the total reduction factor. In order to achieve a periodic R-fold undersampled 2D
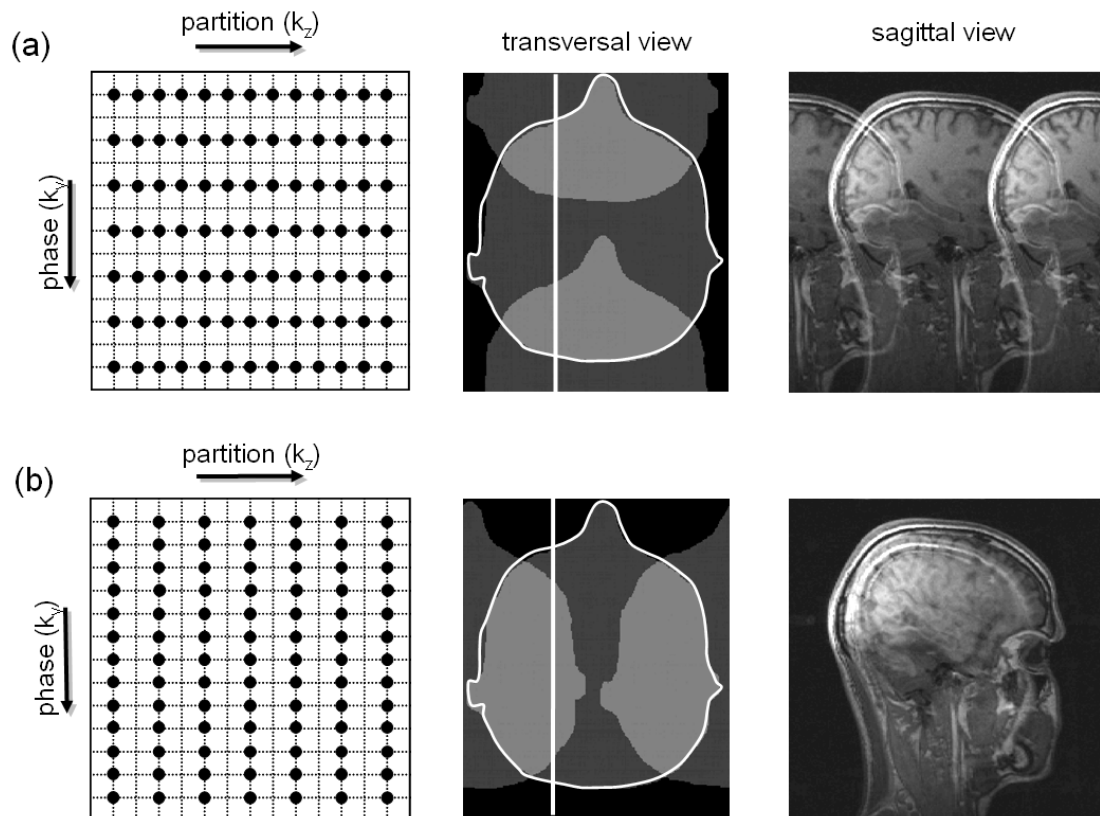
Figure 5.2: Undersampling by a factor R=2 in 3D imaging can be performed either (a) in the normal phase encoding direction or (b) in the partition encoding direction. On the left hand side, the corresponding two-fold undersampled phase encoding schemes are shown. The resulting aliasing conditions are demonstrated for each scenario by means of a masked section of the head in the transversal plane (middle). In addition, one arbitrary section of the reduced data set, indicated by the vertical bar, is displayed in the sagittal view (right). This figure is reprinted from reference [52].
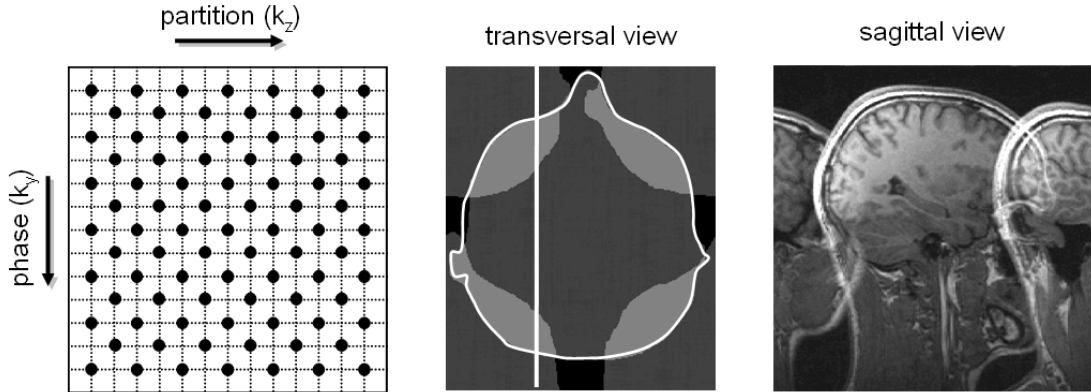
Figure 5.3: 2D CAIPIRINHA-type experiment ($R = 2$). Starting at scenario 1 given in Fig. 5.2a, every second phase encoding value in the k_y direction is shifted by Δk_z in k_z direction. This modification of the sampling pattern directly results in modified aliasing conditions, which are displayed in the transversal and in the sagittal view. This figure is reprinted from reference [52].

acquisition, R sampling points can be arbitrarily distributed in the elementary cell, yielding $\frac{R^2!}{(R^2-R)!}$ possibilities. However, in order to minimize the number of image pixels aliased on top of each other due to undersampling, only sampling positions on so-called sheared grids are considered which form periodic lattices [64, 65]. Thus, as a result of the corresponding two dimensional point spread functions (PSF), a maximum of R pixels are aliased together in one single pixel. Additionally, without loss of generality, only patterns starting at sampling position (1,1) in the binary sampling cell are taken into account. This arrangement leads to a reduced number of acceptable undersampled 2D sampling patterns. In order to find the complete set of patterns given a specific reduction factor R, one arbitrary dimension (e.g. y) can be selected, in which certain degrees of undersampling (e.g. R_y) can be defined.

For example, using a given total reduction factor of $R = 4$, the undersampling rate R_y can take values of $R_y = 1, 2, 4$. For each R_y a certain number of sampling patterns can be created by shifting successive sampling positions in k_y with respect to each other by an amount Δ in the k_z direction (see Fig. 5.4). If a sampling position exceeds R due to the shift, it is wrapped around in the elementary cell. In the end, this strategy leads us to all acceptable 2D sampling patterns. The patterns at a certain undersampling rate R_y are limited to R/R_y, with shifts Δ running from 0 to $R/R_y - 1$. Shifts Δ greater then $R/R_y - 1$ result in repetitive patterns. In Tab. 5.1, all possibilities for R_y are listed for several total reduction factors ($R = 1$ to 16). Furthermore, the corresponding total number of possible sampling patterns given a specific total reduction factor R is shown (last row). The procedure for creating a complete set of possible sampling patterns is illustrated in Fig. 5.4 for a reduction factor of $R = 4$. The first row represents all cases in which $R_y = 1$, with shifts $\Delta = 0, 1, 2, 3$. In the second row, alternative patterns using $R_y = 2$ with shifts $\Delta = 0, 1$ are listed. Finally, the
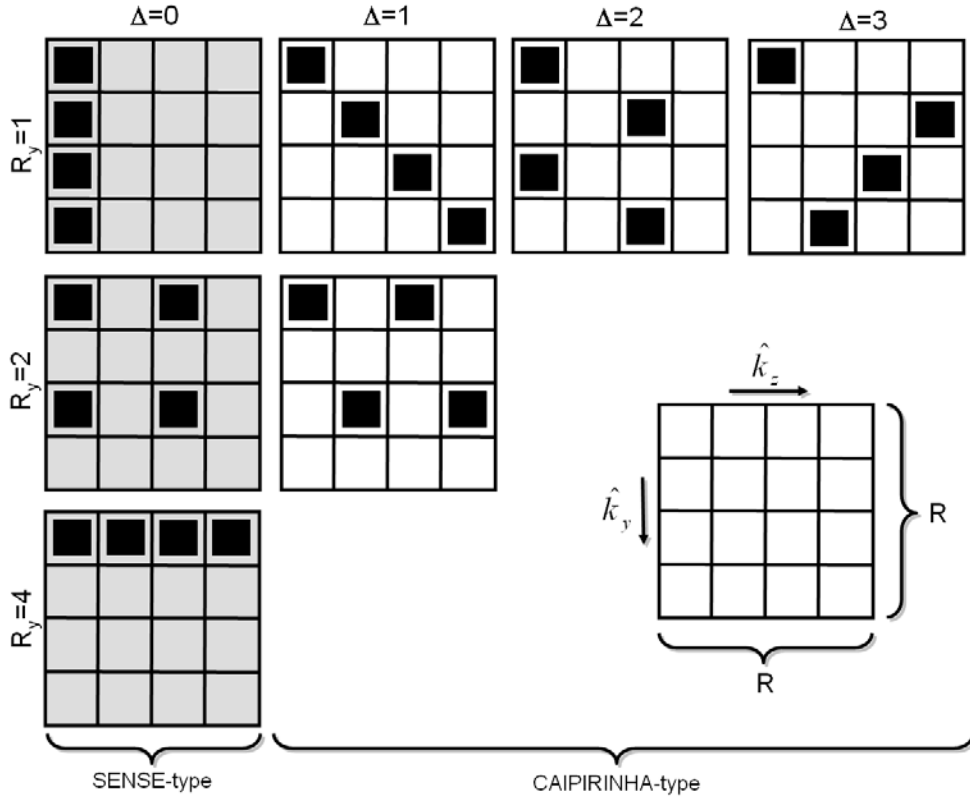
Figure 5.4: Complete set of acceptable sampling patterns given a reduction factor of $R = 4$. The sampling patterns can be represented by an $R \times R$ elementary cell with R sampling positions to fill. For each undersampling rate in the k_y direction (R_y) multiple patterns can be created by shifting sampling positions at row k_y in the k_z direction by a different amount Δ, where Δ runs from 0 to $R_z - 1$, and $R_z = R/R_y$. Sampling patterns with no shift ($\Delta = 0$) are 2D SENSE-type acquisitions, while all the other patterns are represented by 2D CAIPIRINHA-type experiments. This figure is reprinted from reference [52].

R	2	3	4	5	6	7	8	9	10	11	12	13	14	15	16
R_y	1	1	1	1	1	1	1	1	1	1	1	1	1	1	1
	2	3	2	5	2	7	2	3	2	11	2	13	2	3	2
			4		3		4	9	5		3		7	5	4
					6		8		10		4		14	15	8
											6				16
											12				
#SP	3	4	7	6	12	8	15	13	18	12	28	14	24	24	31

Table 5.1: Possible undersampling rates (R_y) are listed for several total reduction factors R. For each R_y, $R_z = R/R_y$ different sampling patterns (SP) are possible, resulting in the total number of acceptable sampling schemes (#SP) given in the last row.

remaining $R_y = 4$ case with $\Delta = 0$ is displayed. In general, rectangular reduced 2D SENSE-type $(R_{SENSE} = R_y \times R_z)$ patterns are listed in the first column without a shift ($\Delta = 0$), while all other sampling schemes are characterized by 2D CAIPIRINHA-type acquisitions including various shifts. For differentiation purposes, 2D CAIPIRINHA-type reduction factors are specified as

$$R_{CAIPIRINHA} = R_y \times R_z^{(\Delta)} \tag{5.1}$$

with Δ representing the applied shift in the k_z direction from one sampling row k_y to the next, and $R_z = R/R_y$.

Reconstruction procedure

2D CAIPIRINHA using SENSE

The first step in 2D CAIPIRINHA reconstruction using SENSE is the creation of a binary matrix, where sampling positions are set to 1 and skipped positions are set to 0. After 2D Fourier transformation of such an R-fold undersampled elementary cell, the corresponding binary 2D point-spread function (see Fig. 5.5) is obtained, which leads directly to the originating spatial locations of the R signals aliased together in one pixel. By means of the R matrix indices $(\hat{y}_l, \hat{z}_l)$ with value 1 in the binary aliasing cell, the R spatial locations (y_l, z_l) in the 2D FOV, and therefore the involved sensitivity values can be determined directly :

$$(y_l, z_l) = \left(y + (\hat{y}_l - 1) \cdot \frac{FOV_y}{R}, z + (\hat{z}_l - 1) \cdot \frac{FOV_z}{R} \right), \qquad l = 1, ..., R \tag{5.2}$$

If the spatial locations y_l or z_l exceed FOV_y or FOV_z, they are simply wrapped around, which can be performed by applying the modulo function in both directions. Using this strategy, an adapted sensitivity map is created, which can be directly provided to the normal SENSE
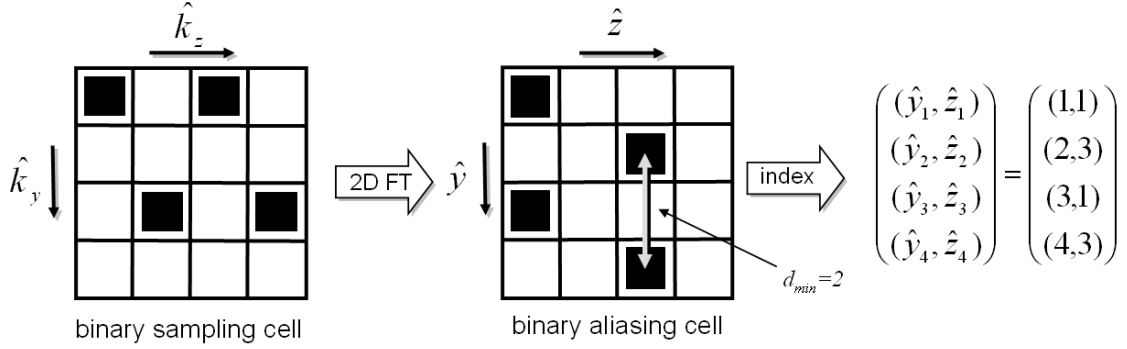
Figure 5.5: Schematic description of a 2D CAIPIRINHA reconstruction procedure. A 2D Fourier transformation of the binary sampling cell directly yields the corresponding 2D point spread function. The minimum distance of points in the aliasing cell d_{min} is a measure of the quality of the point spread function (PSF). The R indices $(\hat{y}_l, \hat{z}_l)$ with value 1 in the resulting elementary aliasing cell allow one to determine the R pixels at the spatial locations (y_l, z_l) which are aliased in one pixel (see Eq. 5.2) and the involved coil sensitivity values which are needed for the following SENSE reconstruction procedure. This figure is reprinted from reference [52].

algorithm. Finally, the output of the SENSE algorithm must be reordered according to the originating spatial locations.

2D CAIPIRINHA using 3D GRAPPA

In principle, the 3D GRAPPA implementation for volumetric PPA [66] is performed according to the conventional 2D GRAPPA reconstruction for two dimensional single-slice PPA with scan time reduction performed only in one phase encoding direction. This reconstruction process has already been described in Section 2.4. Because volumetric parallel imaging involves data reduction along two phase encoding directions, the reconstruction kernel used here is extended to three dimensions (k_x, k_y, k_z). Within such a small three dimensional data block in k-space (see Fig. 5.6a), source points in the k_y- and in the k_z-direction must be chosen according to the reduced sampling pattern for each coil. Similar to conventional 2D GRAPPA for single-slice imaging, multiple source points in the read-direction (k_x) may additionally be exploited to improve the fit procedure. The target points must be selected according to the $R - 1$ missing data points in each coil. The 3D reconstruction kernel is then slid through the ACS data along all three dimensions in order to collect all kernel-replicates available in the ACS data. The repetitions of the source and target data are finally assembled in a source and target matrix. The reconstruction weights are then derived by fitting the source points $\hat{S}_{src}$ to the target points $\hat{S}_{trg}$ as described in Eq. 2.13. This approach is schematically displayed in Fig. 5.6 for a 2D CAIPIRINHA-type reduction of $R = 2 \times 2^{(1)}$. In the actual reconstruction step (Fig. 5.6b), these weights are applied to the acquired data, assembled in a vector $\vec{S}_{acq}$ (right) and used to directly solve for the missing data $\vec{S}_{clc}$ (left). By sliding the 3D pattern through the
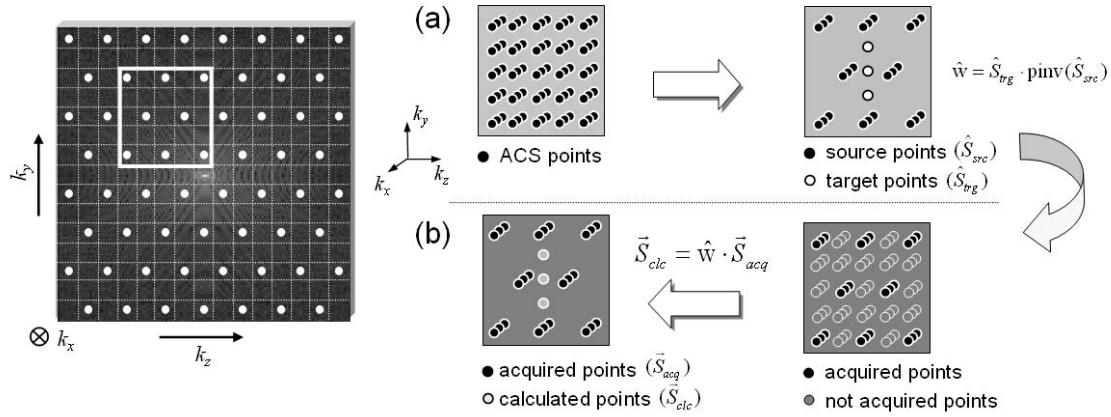
Figure 5.6: Description of the 3D GRAPPA reconstruction procedure for volumetric parallel imging. In the first step (a), the GRAPPA reconstruction weights are derived. A small three dimensional reconstruction kernel (e.g. $k_y \times k_z \times k_x = 5 \times 5 \times 3$) is chosen from the fully-encoded ACS data (left), in which source points in each coil are selected according to the reduced 2D sampling scheme (here CAIPIRINHA-type). For the sake of lucidity in these schematics the coil dimension is omitted. Additionally, the $R-1$ target points must be selected for each coil according to the missing data (right). By sliding the 3D kernel through the 3D ACS data, multiple repetitions of the kernel can be found and assembled in a source $\hat{S}_{src}$ and target $\hat{S}_{trg}$ matrix. By fitting the source matrix to the target matrix via generalized matrix inversion (pinv), three dimensional GRAPPA reconstruction weights $\hat{w}$ are derived. In a second step (b) these weights are applied to the acquired data, assembled in a vector $\vec{S}_{acq}$ (right) and used to directly sove for the missing data $\vec{S}_{clc}$ (left). By sliding the 3D pattern through the undersampled three-dimensional data, all the missing points are calculated. Following this procedure, the data must be reordered according to the correct sampling positions in each coil, thereby arriving at the full 3D k-space in each coil.

undersampled three-dimensional data, all the missing points are calculated. After the data points have been calculated, the data must be reordered according to the correct sampling positions in each coil, thereby arriving at the full 3D k-space in each coil.

By exploiting the convolution theorem, the 3D GRAPPA weights can be transformed into 2D GRAPPA weights (k_y, k_z) for every x position. These 2D weights are then applied to the undersampled 2D k-space for every x position. This implementation results in significantly decreased image reconstruction times, because the matrices involved in the reconstruction process are significantly smaller, which is known to be computationally more efficient.

Principal Component Analysis (PCA)

For choosing the optimal sampling pattern in 2D CAIPIRINHA the mathematical procedure of Principal Component Analysis (PCA) might be useful. The PCA transforms a number of correlated variables into a number of uncorrelated variables called principal components. The PCA basically consists of an eigendecomposition of the covariance matrix $\hat{X}$, which is calculated from, for example, the reference data set for coil calibration. To this end, the data
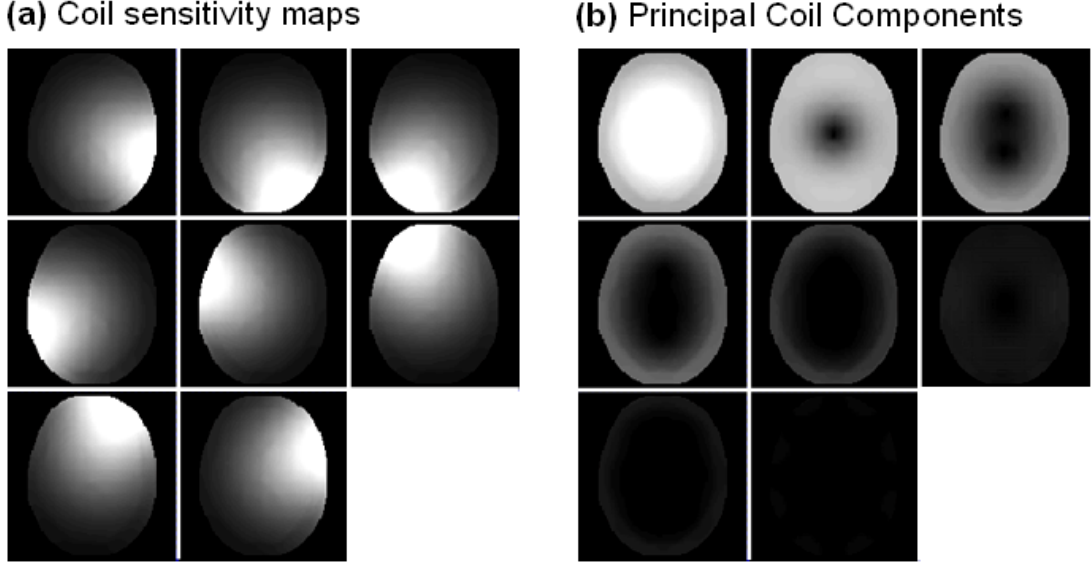
Figure 5.7: (a) Simulated coil sensitivity maps of an cylindrical eight-element coil array and (b) the corresponding Principal Coil Components sorted by their eigenvalues in decreasing order.

are assembled in a $N_C \times N$ matrix $\hat{S}$ where the rows contain the N data samples (in 1, 2 or 3 spatial dimensions) received in the N_C coils.

$$\hat{X} = \hat{S} \cdot \hat{S}^H \tag{5.3}$$

The diagonal elements of the quadratic and symmetric $N_C \times N_C$ covariance matrix $\hat{X}$ represent the variance, the off-diagonal elements the co-varaince between the measurements. High co-variance values correspond to high redundancies. Thus, the smaller the co-variance between measurements, the more uncorrelated is the information among them. Performing an eigenvalue decomposition of the covariance matrix $\hat{X}$ is equivalent to diagonalizing the matrix, which corresponds to reducing redundancy between the data. Thus, after PCA is applied, the data is transformed into linearly independent uncorrelated measurements, the so-called principal components $\hat{S}_{PCA}$.

$$\hat{S}_{PCA} = \hat{V}^H \cdot \hat{S} \tag{5.4}$$

The columns of the matrix $\hat{V}$ contain the N_c linear independent eigenvectors derived by eigenvaluedecomposition. The first principal component accounts for as much of the variability in the data as possible, and each succeeding component accounts for as much of the remaining variability as possible. Fig. 5.7 shows (a) simulated coil sensitivity data from an cylindrical eight-element coil array and (b) the corresponding Principal Coil Components after PCA sorted by their eigenvalues in decreasing order.
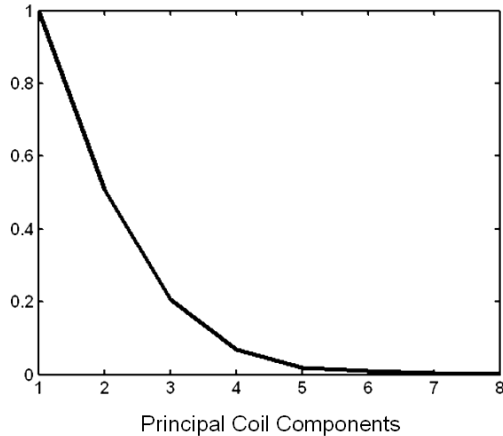
Figure 5.8: Normalized eigenvalues of the Principal Coil Components in decreasing order. Principal Components with low rel. eigenvalues make only little contribution to the over-all sensitivity information.

A plot of the eigenvalue distribution in decreasing order is given in Fig. 5.8. The Principal Coil Component with the highest eigenvalue contributes most to the coil sensitivity information, while the ones with comparatively low eigenvalues have only little impact. Thus, Principal Coil Components with very low relative eigenvalues can be neglected, because they do not carry additional information. This fact allows one to estimate the maximum possible reduction factor for this coil array in this plane. In this case, only 5-6 Principal Coil Components carry uncorrelated spatial sensitivity information. Thus the maximum possible reduction factor in 2D using this coil configuration to $R = 5-6$. Additionally, PCA allows one to reduce data size by removing components with negligible eigenvalues. Especially with today's trend to large coil arrays, PCA can help to significantly reduce the data size, associated with significantly decreased parallel imaging reconstruction times.

5.3   Methods

In vivo experiments were performed on healthy volunteers using a 1.5T clinical whole body scanner (Avanto, Siemens medical solutions, Erlangen, Germany) equipped with 12 independent receiver channels. 2D rectangular and 2D CAIPIRINHA-type acquisitions were performed using the 2D sampling patterns proposed in the theory section (see Fig. 5.4). Starting with a fully-encoded 3D experiment, unwanted phase encoding steps were simply removed from their sampling positions. Sensitivity information was derived from a fully-encoded low-resolution data set for both SENSE and GRAPPA reconstructions.

In vivo head experiments: A 12 channel receiver head coil array composed of two cylindrical 6 coil-rings positioned in the axial direction was used for signal reception. The two phase encoding directions were chosen to be in the AP and the LR direction. Frequency encoding was performed in the HF direction to avoid aliasing from the object outside the FOV. The sequence parameters were as follows: $TE = 4.56ms$, $TR = 12\,ms$, $\alpha = 15°$,

matrix $= 184 \times 192 \times 112$, $FOV = 25.0 \times 26.0 \times 20.0\,cm^3$. Parallel image reconstructions were performed in Matlab (The MathWorks, Natick, Ma.) using SENSE algorithms. The modified aliasing conditions were taken into account as described in the theory section. Geometry factor maps were also calculated as described in the original SENSE paper [23] taking noise correlations into account.

***In vivo* abdomen experiments:** In order to demonstrate the feasibility of GRAPPA in combination with CAIPIRINHA-type acquisitions, volumetric interpolated breath-hold examinations (VIBE) [67, 68] for clinical liver imaging were carried out. A standard 12 channel receiver coil array for abdomen imaging was used for signal reception, consisting of a 3x2 anterior element matrix and a 3x2 posterior element matrix. The matrix had 3 elements running in the LR direction and two elements running in the HF direction. Normal phase encoding was accomplished in the LR direction and partition encoding in the AP direction with excitation slabs (FOV_z) smaller than the actual object size, yielding pre-folding artifacts due to imperfect excitation profiles. In contrast to SENSE, the GRAPPA algorithm can cope with such situations [69]. The frequency encoding was performed in the HF direction to avoid aliasing from the object outside the FOV. The sequence parameters were as follows: $TE = 2.47\,ms$, $TR = 5.62\,ms$, $\alpha = 10°$, matrix $= 128 \times 128 \times 48$ with 6/8 partial Fourier in the partition direction. The experiment was performed with different fields of view, namely $FOV = 40.0 \times 40.0 \times 14.4\,cm^3$ and $FOV = 40.0 \times 40.0 \times 9.6\,cm^3$, corresponding to partitions of $\Delta z = 3mm$ and $\Delta z = 2mm$ thickness. Parallel image reconstructions were performed in Matlab (The MathWorks, Natick, Ma.) using two dimensional GRAPPA algorithms for each section in the x-direction as pictured in the theory section.

Computer simulations: In order to further investigate the properties of 2D CAIPIRINHA, computer simulations were performed. A standard 16-channel receiver head coil array, providing not only sensitivity variations in the radial direction but also in the axial direction, was simulated (see Fig. 4.5). The array was made up of two cylindrical 8 coil-rings positioned in axial direction with $2\,cm$ overlap. The total coil dimensions were $28\,cm$ length and $28\,cm$ diameter. The coil sensitivity characteristics were calculated in Matlab using analytical Biot-Savart integrations.

5.4   Results

In order to demonstrate the benefit of the CAIPIRINHA approach, all 15 feasible 2D acquisition patterns (2D rectangular and 2D CAIPIRINHA-type) given a reduction factor of $R = 8$ (see Tab. 5.1) were generated. Afterwards, image reconstructions were performed using SENSE algorithms as described earlier. Additionally, g-factor maps were calculated in order to compare the reconstruction performance. In Fig. 5.9, parallel image reconstruction of a single transversal plane is shown after standard rectangular 2D SENSE-type accelerated
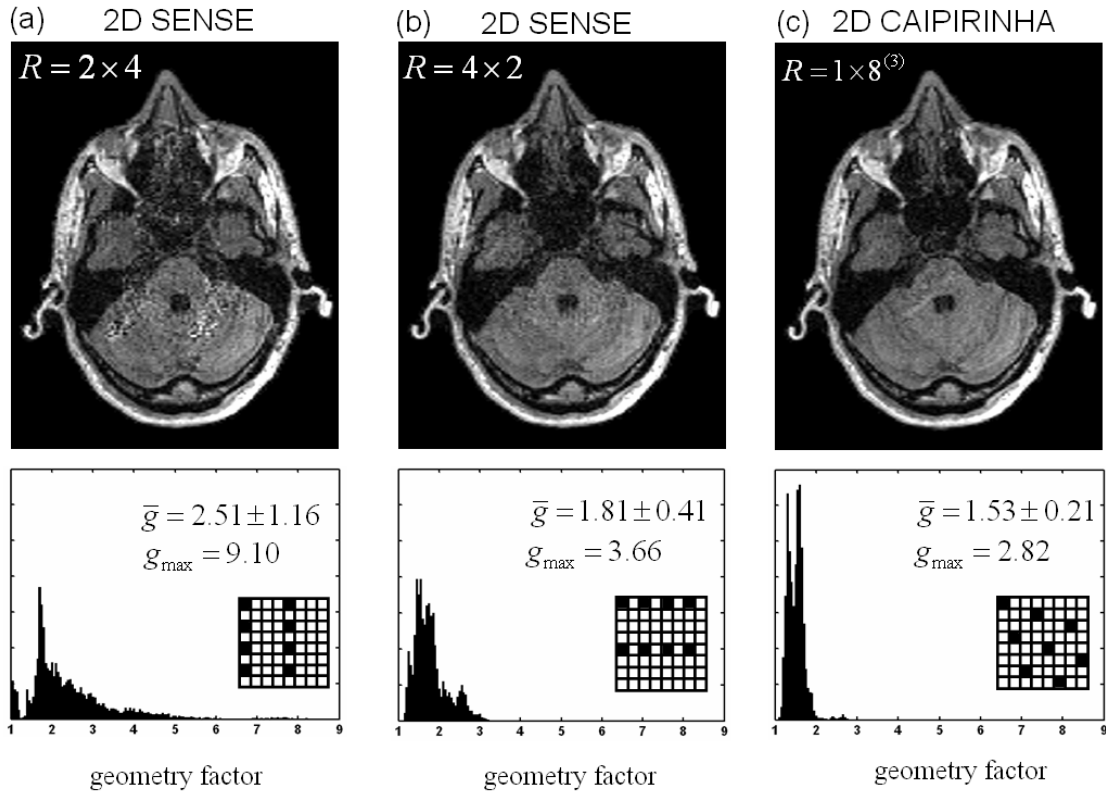
Figure 5.9: *In vivo* results after accelerated ($R = 8$) (a) rectangular 2D SENSE ($R = 2 \times 4$) (b) 2D SENSE ($R = 4 \times 2$) and (c) 2D CAIPIRINHA ($R = 1 \times 8^{(3)}$) experiments of the human head. As an example, image reconstructions of one transversal plane plane in the read-direction are shown for each experiment. Histogram plots of the corresponding g-factor maps are included to demonstrate the reconstruction performance. Additionally, the mean g-factor values and their standard deviations are given for each 2D sampling scheme. This figure is reprinted from reference [52].

in vivo head experiments (a) $R = 4 \times 2$ and (b) $R = 2 \times 4$. Additionally, the 2D CAIPIR-INHA SENSE-type experiment with the lowest mean g-factor and lowest standard deviation $R = 8 \times 1^{(3)}$(c) is displayed. As can be seen, the image quality of the 2D CAIPIRINHA SENSE-type experiment is clearly superior to both rectangular 2D SENSE-type experiments due to a significantly lower geometry-related noise enhancement. This fact is even more obvious when comparing the histogram plots of the corresponding geometry factor maps. Besides a significant improvement in the mean g-factor, the histogram plots indicate a much more homogeneous reconstruction performance, which is illustrated by the narrow distribution of the histogram.

In Tab. 5.2, the mean g-factor with corresponding standard deviation is listed for all 15 possible sampling patterns at a reduction factor of $R = 8$. Additionally, the relative minimum distance d_{min} is given, which is a measure of the quality of the corresponding point spread

R	$\bar{g}$	PSF (rel dist)
$1x8^{(0)}$	25.68 ± 19.21	1
$1x8^{(1)}$	6.36 ± 3.80	1.41
$1x8^{(2)}$	1.66 ± 0.30	2.24
$1x8^{(3)}$	1.53 ± 0.21	2.83
$1x8^{(4)}$	2.51 ± 1.17	2
$1x8^{(5)}$	1.54 ± 0.21	2.83
$1x8^{(6)}$	1.65 ± 0.27	2.24
$1x8^{(7)}$	6.02 ± 3.58	1.41
$2x4^{(0)}$	2.51 ± 1.16	2
$2x4^{(1)}$	1.87 ± 0.51	2.24
$2x4^{(2)}$	1.55 ± 0.21	2.83
$2x4^{(3)}$	1.86 ± 0.46	2.24
$4x2^{(0)}$	1.81 ± 0.41	2
$4x2^{(1)}$	1.80 ± 0.40	2
$8x1^{(0)}$	14.82 ± 10.57	1

Table 5.2: Mean g-factors $\bar{g}$ and corresponding standard deviations for all 15 sampling schemes at a total reduction factor of $R = 8$. Additionally, the relative minimum distances d_{min} of aliased points in the elementary aliasing cell are given, which is a measure for the quality of the point spread function. The greater the distance of aliased points the more sensitivity variations are exploitable.

function (PSF). The value d_{min} is determined by calculating the minimum distance of aliased points in the binary aliasing cell (see Fig. 5.5).

The GRAPPA method features some advantages compared to SENSE. One prominent example are applications where sensitivity maps, as required for SENSE reconstruction, are hard to obtain. This is the case in regions with low SNR, such as the lung [15]. Another example are applications where pre-folding in the full FOV is required for time-efficient imaging [69]. Therefore, additional results are presented which demonstrate the feasibility of performing parallel imaging reconstruction with GRAPPA as well. In Fig. 5.10, GRAPPA reconstructions of accelerated ($R = 4$) VIBE experiments in the abdomen with $\Delta = 3mm$ partition thickness using rectangular $R = 4 \times 1^{(0)}$, $R = 2 \times 2^{(0)}$ and CAIPIRINHA-type $R = 2 \times 2^{(1)}$ reductions are displayed for three different partitions. Additionally, the corresponding unaccelerated image is given as a reference. As demonstrated in Fig. 5.10 the CAIPIRINHA-type acquisition performs significantly better than either of the conventional rectangular reduced acquisitions. For quantification purposes the artifact energy AE was calculated for each partition according to

$$AE = \frac{\sum |I_{Ref} - I_{PPA}|^2}{\sum |I_{Ref}|^2} \tag{5.5}$$

I_{Ref} denotes the sum-of-squares combined reference image and I_{PPA} the sum-of-squares combined image after GRAPPA reconstruction. The sum in Eq. 5.5 is performed along all spatial image pixels. The artifact energy AE is a measure for the reconstruction quality of the parallel
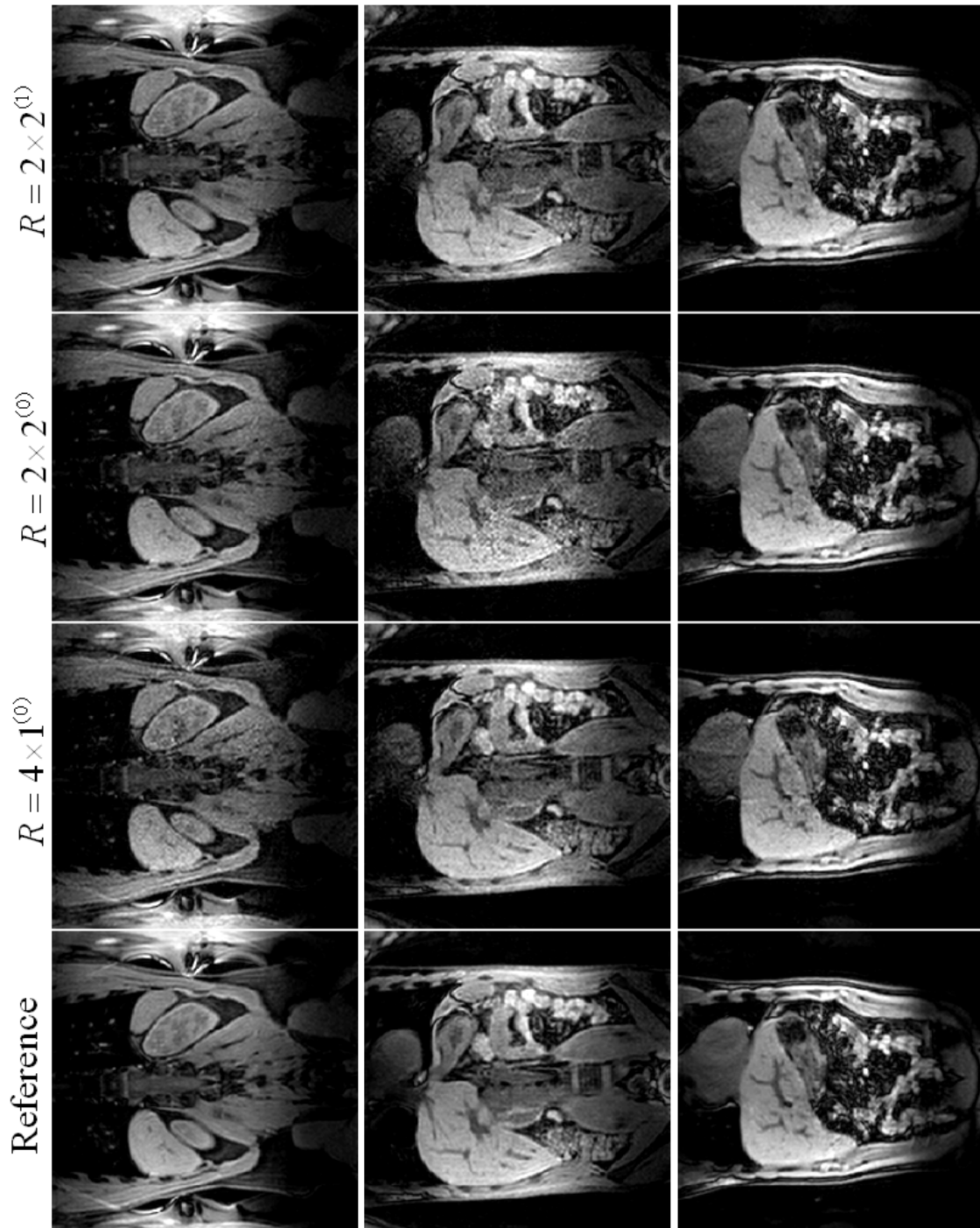
Figure 5.10: Various $R = 4$ accelerated acquisitions after GRAPPA reconstruction are shown for three out of 48 partitions. As a reference, the unaccelerated partitions are displayed (left column). The conventional rectangular reduced experiments ($R = 4 \times 1^{(0)}$ and $R = 2 \times 2^{(0)}$) are compared with the CAIPIRINHA-type experiment ($R = 2 \times 2^{(1)}$). For each partition, the CAIPIRINHA-type experiment provides comparable or even better image quality than either of the conventional reduced acquisitions.
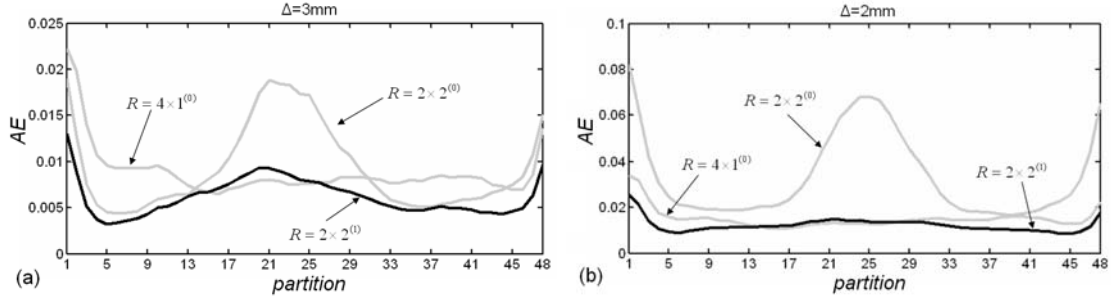
Figure 5.11: Artifact energy AE after GRAPPA reconstruction calculated for various four-fold accelerated sampling scenarios ($R = 4 \times 1^{(0)}$, $R = 2 \times 2^{(0)}$, $R = 2 \times 2^{(1)}$). The artifact energy is plotted for each partition and is given for experiments with partition thickness of (a) $\Delta = 3\,mm$ corresponding to an excitation slab of $14.4\,cm$ and (b) $\Delta = 2$ corresponding to a excitation slab of $9.6\,cm$.

	$R = 4 \times 1^{(0)}$	$R = 2 \times 2^{(0)}$	$R = 2 \times 2^{(1)}$
$\Delta s = 3mm$	0.0089 ± 0.0029	0.0093 ± 0.0046	0.0062 ± 0.0020
$\Delta s = 2mm$	0.0152 ± 0.0044	0.0337 ± 0.0183	0.0123 ± 0.0030

Table 5.3: Mean artifact energy AE and corresponding standard deviation for various four-fold accelerated parallel acquisitions after GRAPPA reconstruction ($R = 4 \times 1^{(0)}$, $R = 2 \times 2^{(0)}$, $R = 2 \times 2^{(1)}$). The 2D CAIPIRINHA-type experiment provides lowest mean artifact energy and lowest standard deviation for both experiments with $\Delta z = 3\,mm$ and $\Delta z = 2\,mm$. It is obvious that the $R = 2 \times 2^{(1)}$ reconstruction performance for a very small excitation slab approaches the $R = 4 \times 1^{(0)}$ performance.

imaging reconstruction, where a low artifact energy value corresponds to good reconstruction quality. The AE was calculated for each partition and for all three reduction scenarios. In Fig. 5.11, the resulting artifact energies are plotted as a function of partition number for two experiments with different FOV_z (or excitation slab thickness), corresponding to partitions of (a) $\Delta z = 3\,mm$ and (b) $\Delta z = 2\,mm$ thickness. It is obvious that 2D CAIPIRINHA provides the best overall performance.

In addition, in Tbl. 5.3 the mean arifact energies AE and the corresponding standard deviations are given for all three acquisition strategies after 3D GRAPPA reconstruction. As can be seen, the 2D CAIPIRINHA-type experiment ($R = 2 \times 2^{(1)}$) provides lowest mean overall artifact energy and lowest standard deviation for both experiments with $\Delta z = 3\,mm$ and $\Delta z = 2\,mm$ compared to the conventional rectangular reduced acquisitions.

Simulation results are presented in Fig. 5.12 for various four-fold accelerated 2D parallel imaging experiments. The simulations were based on the sensitivity characteristics calculated from a cylindrical 16 channel head array, which has been described in the methods section. For all simulated scenarios, the partition encoding was chosen to be in the axial direction
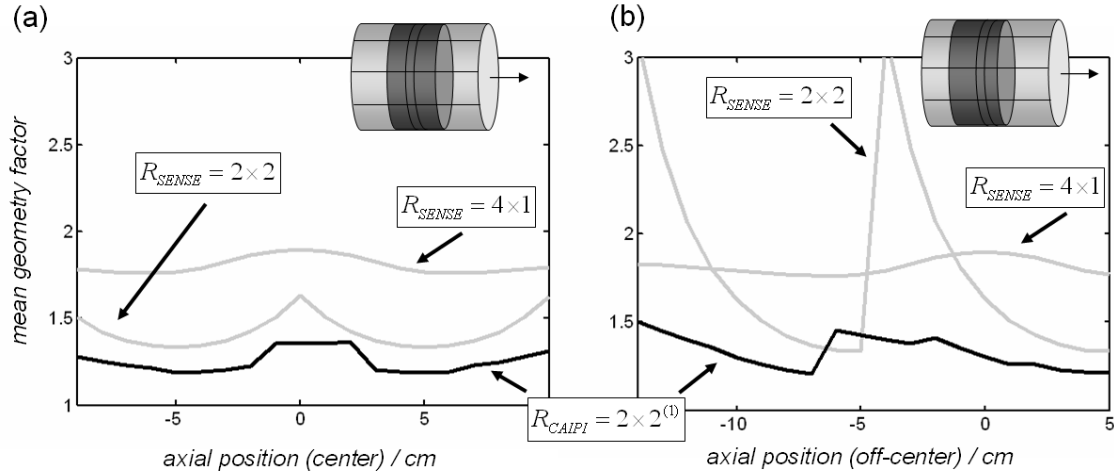
Figure 5.12: Results of several four-fold accelerated 2D parallel imaging experiments, exploiting the sensitivity distribution of a simulated cylindrical 16 channel two ring head array. The mean geometry factor as a function of the axial partition position after rectangular 2D SENSE ($R = 2 \times 2$ and $R = 4 \times 1$) and 2D CAIPIRINHA ($R = 2 \times 2^{(1)}$) is plotted, given a 20 cm slab (a) carefully positioned in the center of the coil and (b) positioned $5cm$ off-center. While the $R_{SENSE} = 4 \times 1$ experiment has a performance which is much more independent of the slab position, the $R_{SENSE} = 2 \times 2$ experiment performs significantly better when the slab is in the center position, as sensitivity variations are exploited in both directions simultaneously. In the off-center position, however, this acquisition strategy provides an inhomogeneous performance, with partitions showing very high geometry factors. In contrast, the 2D CAIPIRINHA-type experiment $R_{CAIPIRINHA} = 2 \times 2^{(1)}$ provides the best reconstruction performance with a more homogeneous characteristic for both scenarios. This figure is reprinted from reference [52].

and an excitation slab 20cm thick was assumed. The resulting mean and maximum geometry factors were calculated for every partition and plotted as a function of the axial partition position after 2D SENSE ($R_{SENSE} = 2 \times 2$ and $R_{SENSE} = 4 \times 1$) and 2D CAIPIRINHA-SENSE ($R_{CAIPI} = 2 \times 2^{(1)}$) experiments. In one case (a), the excitation slab was carefully positioned in the center of the coil, whereas in the other case (b), the slab was moved $5\,cm$ off-center. The $R_{SENSE} = 4 \times 1$ experiment has a performance which is much more independent of the slab position, as sensitivity variations in the axial direction are not exploited. In contrast, the 2D SENSE ($R_{SENSE} = 2 \times 2$) experiment performs significantly better when the slab is positioned in the center of the coil. In this case, sensitivity variations in the partition direction which are provided by the two ring coil geometry can be used. In the off-center position, this acquisition strategy results in an inhomogeneous performance with some partitions showing extremely high geometry factors. However, the 2D CAIPIRINHA-type experiment $R_{CAIPI} = 2 \times 2^{(1)}$ provides the best reconstruction performance and exhibits a very homogeneous g-factor behavior for both scenarios.

The parallel encoding capability of the 12 channel head array in one axial plane was tested by applying the PCA to the 2D reference data needed for coil calibration. In Fig. 5.13 (a)
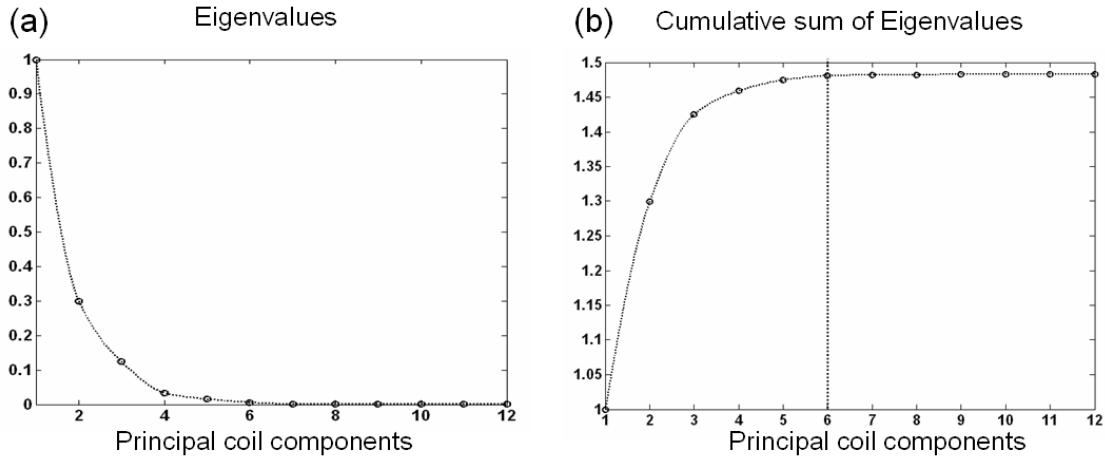
Figure 5.13: (a) Eigenvalues (normalized to one) after PCA applied to 12 channel head data and (b) the cumulative sum of the eigenvalues. Only 6 of the 12 principal coil components are uncorrelated and therefore give contribution to the parallel imaging encoding. This limits the maximum possible reduction factor in two spatial dimensions to R=6 with this coil array.

the resulting eigenvalues (normalized to one) and (b) the cumulative sum of the eigenvalues are plotted. It can be seen that only 6 of the 12 principal coil components are uncorrelated and therefore give significant contribution to the parallel imaging encoding. This limits the maximum possible reduction factor in two spatial dimensions to R=6 in this plane for this coil configuration. In order to investigate the encoding efficiency in the individual spatial directions the PCA was additionally applied separately in the LR and in the AP directions using simple projections. In Fig. 5.14 the (a) normalized eigenvalues of the PCA and (b) the cumulative sum of these eigenvalues are plotted for both projections. This illustration allows one to compare qualitatively the encoding efficiency in these two directions. The position where the curve reaches saturation gives an estimation of the maximum possible reduction factor in this direction. Additionally, the saturation value itself (integral) contains information which can be used to determine the more efficient encoding direction, which in this case is the AP direction.

To emphasize this fact, Fig. 5.15 shows geometry-factor maps and SENSE reconstructions with a reduction factor of R=3 applied (a) only in the AP and (b) only in the LR direction. This analysis allows one to determine the maximum reduction factor in 2D and the adequate reductions in the individual phase encoding directions in rectangular 2D parallel MRI. As already mentioned, given a total reduction factor, a number of CAIPIRINHA-type patterns provide an optimal PSF. PCA applied to projections could help to choose the pattern which exploits the coil sensitivity variations most efficiently.
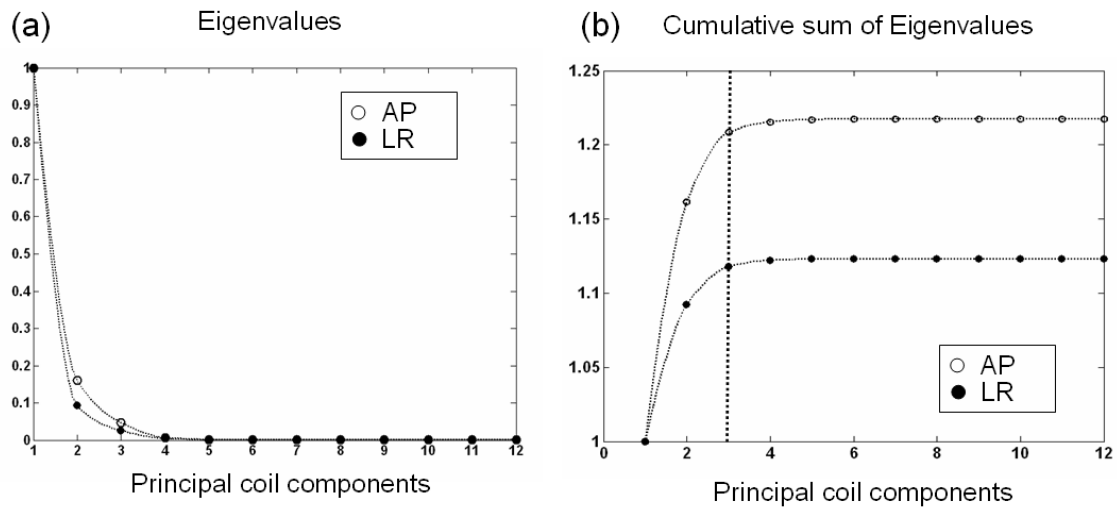
Figure 5.14: (a) normalized eigenvalues of the Principal Coil Components and (b) the cumulative sum of these eigenvalues are plotted for both projections. The Principal Coil Component at which the curve reaches saturation gives an estimation of the maximum possible reduction factor in this direction. Additionally, the saturation value itself (integral) contains information which can be used to determine the more efficient encoding direction.
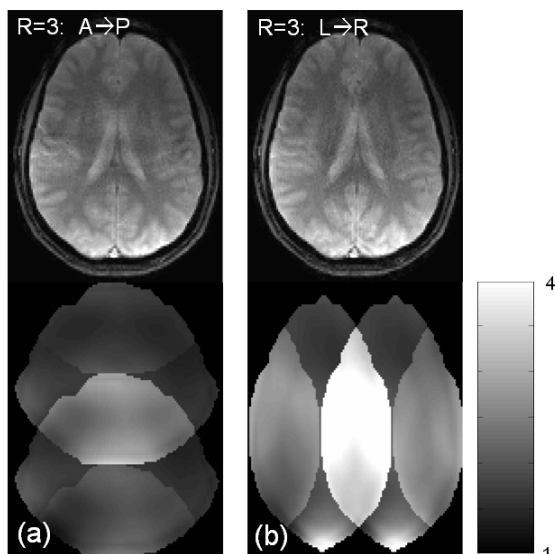

Figure 5.15:   SENSE reconstructions (top) and corresponding g-factor maps (bot) after $R = 3$ -fold acceleration performed (a) only in the AP and (b) only in the LR direction. The g-factor analysis proves the prediction made after PCA has been seperately applied to the projections.

5.5 Discussion

2D CAIPIRINHA has been presented as a means of exploiting sensitivity variations more efficiently in 2D parallel imaging. The properties of this technique were studied using computer simulations as well as *in vivo* studies. 2D CAIPIRINHA-type accelerated *in vivo* head experiments were successfully performed up to reduction rates of $R = 8$ using SENSE algorithms, which still provided an acceptable SNR and image quality compared to conventional parallel imaging strategies. Additionally, the two dimensional GRAPPA method has been extended to volumetric GRAPPA and has been shown to reconstruct 2D CAIPIRINHA-type reduced VIBE abdomen data sets with good image quality. The *in vivo* and simulation results indicate that 2D CAIPIRINHA-type acquisitions have the potential to provide a more robust and homogeneous reconstruction than conventional accelerated rectangular 2D SENSE and 1D SENSE-type acquisitions, even in cases where the setup is not optimized with regard to the sensitivity variations provided by the actual coil configuration.

However, at a specific reduction factor R, only one of the described 2D sampling patterns will be best suited for a given coil array, slab orientation, and object shape. At a given total reduction factor R, multiple patterns have optimal PSFs with maximum distance of aliased points. In the case of a total reduction factor of $R = 8$, 3 of the 15 possible patterns have optimal PSFs. Because sensitivity variations tend to increase with increasing distance, patterns with optimal PSF are generally favourable, and therefore one of these patterns is most likely to be best suited. However, it is clear that even the best PSF is ineffective when aliased signals with insufficient sensitivity variations are present. Since the optimal patterns are basically rotations of each other, one will quite surely exploit sensitivity variations most efficiently. Additionally, as can be seen in Fig. 5.3, the area with signal overlap can potentially be reduced using these optimal patterns by exploiting object-free regions inside the FOV more efficiently. Therefore, the exact sampling pattern used should be optimized beforehand, taking into account the coil array, the expected object, and FOV size. A potential strategy for finding the optimal sampling pattern could be to run a low resolution geometry factor analysis on the few patterns with optimal PSF, which gives the pattern with lowest mean g-factor and standard deviation [70]. An other possible approach is Principal Component Analysis (PCA) applied to the sensitivity information [71], which allows one to estimate the maximum possible total reduction factor R and the maximum possible reduction for a given coil configuration. Additionally, PCA applied to multiple directions separately by using for example simple projections, allows one to determine the spatial direction with the most variations in the array.

Generally, the 2D CAIPIRINHA approach provides a broad range of applications. Especially those applications using relatively thin excitation slabs will directly benefit from this approach, such as Time-Of-Flight (TOF) angiography. Standard rectangular reduction in the partition encoding direction only helps for large excitation slabs with sufficient sensitivity

variations.

2D CAIPIRINHA is easy to implement, as no special demands are made on the hardware or software. Additionally, no special RF pulses are needed to control aliasing artifacts as are required for MS CAIPIRINHA. This eliminates the main limitation of CAIPIRINHA in simultaneous multi-slice imaging, namely the increased specific absorption rate (SAR) when exciting multiple slices simultaneously. Generally, 2D CAIPIRINHA is applicable to all common Cartesian sampled imaging techniques (FLASH, RARE, TrueFISP, EPI,...), and image reconstructions can be carried out using standard PPA reconstruction algorithms such as SENSE or GRAPPA.

5.6   Conclusion

In conventional PPA accelerated 3D imaging, data reduction is performed in two spatial dimensions simultaneously by integer-valued undersampling in each phase encoding direction. Though sensitivity variations can be exploited in two spatial dimensions, this sampling strategy provides suboptimal encoding performance.

In this work, a 2D parallel imaging strategy has been presented which takes advantage of the recently introduced concept of CAIPIRINHA (Controlled Aliasing In Parallel Imaging Results IN Higher Acceleration). Aliasing artifacts in 2D parallel imaging are modified in a controlled manner during the data acquisition by shifting sampling positions in the two dimensional phase encoding scheme with respect to each other (2D CAIPIRINHA). In this way, at certain image acceleration values, an optimal sampling pattern can be found which minimizes signal overlap and at the same time allows one to efficiently exploit the sensitivity variations provided by the coil array. This strategy provides optimal reconstruction performance given a certain coil configuration and object shape, and therefore directly results in optimal image reconstruction quality. This has been shown for both SENSE and GRAPPA reconstructions.

Chapter 6

3D CAIPIRINHA

6.1 Introduction

In the previous chapter, it has been demonstrated that, by modifying the undersampling 2D phase encoding pattern in volumetric parallel imaging, the sensitivity variations provided by the receiver array can be exploited more efficiently (2D CAIPIRINHA). This approach makes use of sensitivity variations in the undersampled phase encoding directions. The coil array, however, might provide some further sensitivity variations in the third remaining spatial dimension, which are generally not used in the parallel imaging reconstruction process. The availability of more and more independent receiver channels allows one to cover the object under investigation more densely with an increased number of small surface coils positioned along all spatial dimensions. Most of the receiver coil arrays, which are supplied with the latest scanner generation provide sensitivity variations in all three dimensions. Prominent examples are the standard 12 channel head coil consisting of two cylindrical 6-coil rings in axial direction, which is part of the Siemens Avanto system, as well as the standard 12 channel body array with a 3x2 anterior element matrix and a 3x2 posterior element matrix.

In conventional volumetric imaging, only two phase encoding directions are available in which scan time reduction can be performed. Therefore, an alternative strategy is required to take advantage of the sensitivity variations in the remaining third dimension. A potential approach is switching rapidly oscillating phase encoding gradients during the actual read-out process, thereby jumping between adjacent lines in the phase encoding direction. This type of sampling modifies the appearance of aliasing in all three dimensions, thereby exploiting some additional sensitivity variations in the read-out direction, which directly results in improved parallel imaging reconstruction conditions [72]. Naturally, this strategy can also be used in conventional single-slice parallel imaging, where image acceleration is limited by the fact that sensitivity variations are only exploited in one dimension. In previous work, such zig-zag sampling has already been implemented on modern scanners and shown to improve image quality in GRASE experiments (vGRASE) [73]. Moriguchi *et al.* have recently proposed

bunched phase encoding, a method which allows one to reduce the number of phase encoding steps by a factor of two by using an oversampled zig-zag read-out trajectory [74]. As this method has shown to allow a two-fold scan time reduction with one receiver coil, further work from the same group has demonstrated that this concept can be combined with parallel imaging to further gain imaging speed [75]. While in these works image reconstruction is (partially) performed using properties of Popoulis' generalized sampling expansion [76], in this approach, image reconstruction is done entirely using the parallel imaging strategy.

Whereas in MRI one spatial dimension is frequency encoded, in spectroscopic Chemical Shift Imaging (CSI) [77] all the spatial dimensions must be phase encoded, because the frequency is used to obtain the spectral information. Thus, the concept of 2D CAIPIRINHA for volumetric parallel MRI can be directly transferred to 2D CSI, because both methods share the same two-dimensional phase encoding concept. However, in 3D CSI a third phase encoding direction is acquired in which undersampling can be performed, which allows one to extend the CAIPIRINHA concept to an additional spatial dimension. Thus, similar to 2D CAIPIRINHA, sampling positions can be shifted with respect to each other in three spatial dimensions, thereby creating 3D CAIPIRINHA-type sampling patterns. Again, one of such sampling patterns will exploit sensitivity variations provided by the receiver array most efficiently. As a proof of principle, the benefit of this approach is demonstrated on phantom experiments.

6.2   Zig-zag Sampling in Parallel MRI

In order to demonstrate the effect of zig-zag read-out trajectories on the aliasing appearance in the image domain, a conventional four-fold accelerated acquisition is displayed in Fig. 6.1a. As can be seen, conventional undersampling results in a four times reduced FOV in the phase encoding direction yielding the well-known undersampling aliasing artifacts in the phase encoding direction. By performing the same experiment with rapidly switched oscillatory phase encoding gradients during the actual read-out process (Fig. 6.1b left), sampling positions can be shifted in the phase encoding direction in an alternating fashion (Fig. 6.1b middle). After inverse Fourier transformation, the modified aliasing conditions can be seen (Fig. 6.1b right). The sampling patterns created with such zig-zag type read-out trajectories differ in part from the 2D CAIPIRINHA sampling patterns described in the previous chapter. The reason is the oscillating trajectory itself, and the limited gradient switching times. In contrast to sampling positions on sheared grids, which provide a minimized number of image pixels which are aliased on top of each other, more image pixels which are differently weighted by the non-uniformly distributed point spread function are aliased on top of each other in this case. While this fact must be considered in SENSE reconstructions, GRAPPA can deal with this situation by choosing the appropriate target points. In the implementation considered
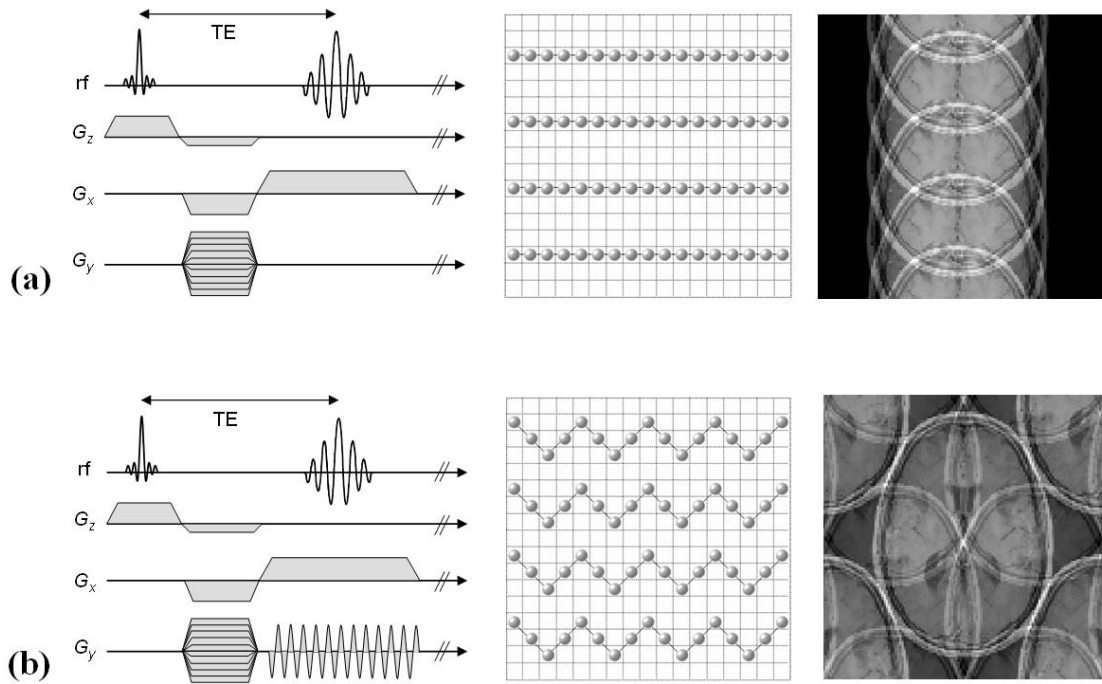
Figure 6.1: (a) On the left, the pulse program of a conventional four-fold accelerated parallel imaging experiment is displayed, showing the reduced phase encoding table and the following read-out process. Additionally, a schematic of the corresponding trajectory in k-space is shown (middle), offering a straight read-out line. On the right, the resulting aliased image is displayed with folding-over artifacts appearing only in the phase encoding direction. (b) In addition to the reduced gradient table, an oscillating gradient is applied during acquisition, resulting in oscillating sampling positions in the phase encoding direction (middle). In contrast to conventional undersampling, blipped sampling results in significantly different aliasing artifacts which appear in both the phase encoding and the frequency encoding direction.

here, the zig-zag trajectories are designed in such a way that the sampling positions lie on a Cartesian grid, although this restriction is not necessary.

To further investigate the properties of zig-zag sampling in combination with parallel imaging, various zig-zag read-out trajectories at a reduction factor of $R = 4$ were simulated. To this end, starting from a fully encoded single-slice head experiment performed on a 1.5T clinical scanner (Avanto, Siemens Medical Solutions, Erlangen, Germany), superflous data points were removed from their sampling positions in k-space (Fig. 6.2 (top row)). While all sampling positions simulated in this work were sampled on a Cartesian grid, other oscillating trajectories using non-Cartesian sampling could be used as well. In such cases, however, advanced parallel imaging reconstruction algorithms including regridding procedures are required.

In Fig. 6.2, the reconstruction performance of various $R = 4$ undersampled sampling patterns showing different zig-zag trajectories are displayed.
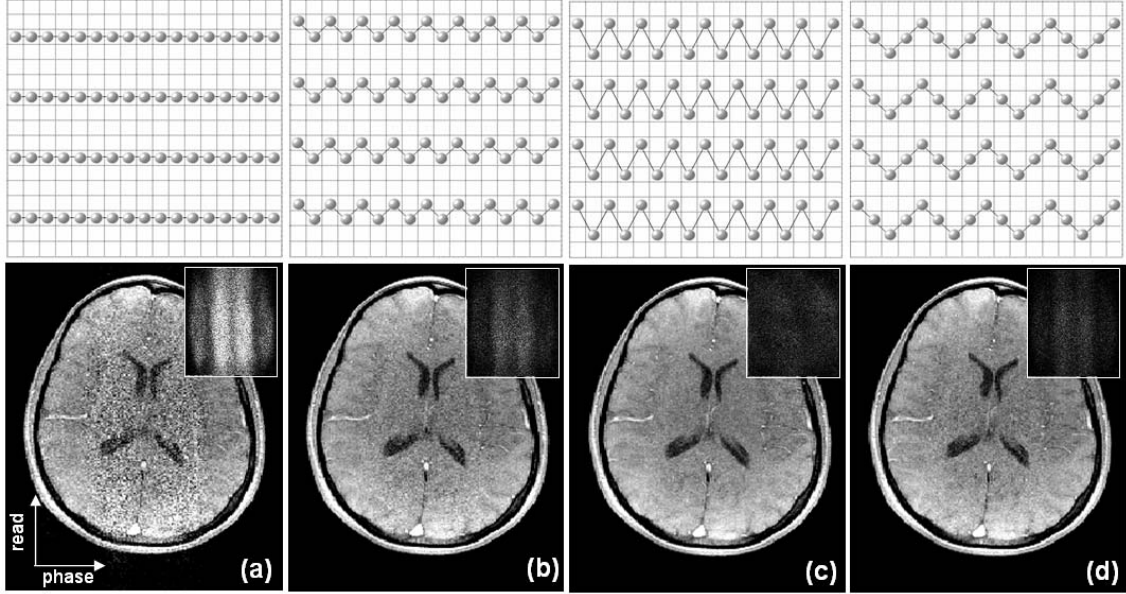
Figure 6.2: GRAPPA reconstructions after accelerated (R=4) experiments using (a) conventional read-out trajectory and (b,c,d) various zig-zag trajectories. The trajectory in (b) is designed in such a way that every second read-out sample is shifted by Δk_y within one dwell-time t_d. In (c) the sampling positions are shifted by $2\Delta k_y$ in the same time requiring two-times higher gradient strength and four-times shorter switching times. The trajectory given in (d) shares the same gradient requirements as in (b) because $2\Delta k_y$ is travelled within two dwell-times $2t_D$. In order to demonstrate reconstruction performance the difference to the fully-encoded reference image is given at the right top corner for each case.

It is obvious that, when shifting sampling positions in the phase encoding direction from their original positions, significantly improved image quality is achieved after parallel imaging reconstruction is performed. All zig-zag trajectories simulated here result in significantly improved image quality compared to the conventional undersampled data. The image in Fig. 6.2c shows the best image quality after specialized GRAPPA reconstructions, but requires highest gradient performance to achieve this trajectory. While the trajectories in (b) and (d) share the same gradient requirements, the latter performs better because the maximum shift achieved is $2\Delta k_y$, resulting in a better PSF, and thus exploiting sensitivity variations more efficiently.

The concept of zig-zag sampling can also be applied to volumetric parallel imaging. To this end, in addition to 2D CAIPIRINHA-type sampling patterns in the k_y,k_z-plane, a zig-zag trajectory was performed in the read-out direction in order to shift the 2D CAIPIRINHA phase encoding patterns with respect to each other for subsequent read-out positions (k_x). In this way, an improved PSF can be achieved, thereby allowing the utilization of potential sensitivity variations in all three spatial dimensions. To demonstrate the benefit of this approach, zig-zag type sampled 3D CAIPIRINHA patterns were simulated from a fully-encoded

3D head experiment performed on a 1.5T clinical scanner (Avanto, Siemens Medical Solutions, Erlangen, Germany). For signal reception, the 12-channel head coil array was used (two cylindrical 6 coil rings in the axial direction). The sequence parameters for the 3D FLASH sequence were as follows: $\alpha = 15°$, $TE/TR = 4.56\,ms/12\,ms$, $FOV = 260 \times 260 \times 216\,mm^3$, matrix size $= 192 \times 192 \times 120$. Similar to previous proceedings unwanted sampling points were removed from the fully encoded 3D k-space. Starting from an adequate $R = 8$ 2D CAIPIRINHA-type reduced sampling scheme $R = 2 \times 4^{(2)}$ a zig-zag read-out trajectory was designed which shifted the 2D CAIPIRINHA sampling pattern by Δk_y in the k_y-direction and Δk_z in the k_z-direction in an alternating fashion for subsequent read-out samples. In practice, such sampling can be realized by applying rapidly oscillating gradients in both phase encoding directions during the read-out process. In Fig. 6.3, various $R = 8$ fold accelerated sampling strategies (2D rectangular, 2D CAIPIRINHA and 3D CAIPIRINHA -type reductions) were compared after 3D GRAPPA reconstructions. Again, the results presented here demonstrate that 2D CAIPIRINHA is clearly superior to conventional rectangular reduction schemes. However, 3D CAIPIRINHA performs even better, because sensitivity variations in the read-direction have been additionally exploited, resulting in significantly improved image quality after parallel imaging reconstruction.

6.3 3D Chemical Shift Imaging

In spectroscopic imaging, or chemical shift imaging (CSI), a spectral dimension is acquired in addition to the spatial dimensions. The spatial dimensions are all encoded using the concept of phase encoding (switching phase encoding gradients in all spatial dimensions prior to acquisition) while the spectral information is achieved by a frequency analysis of the plain NMR signal (free induction decay (FID) or spin echo) acquired without employing a read gradient. Spins in different chemical environments precess at different frequencies (chemical shifts), thereby providing signals at different frequencies in the spectra. Thus, a CSI experiment includes volume selective excitation, followed by phase encoding gradients in two (2D CSI) or three (3D CSI) directions and finally acquisition of the FID or a spin echo in the absence of gradients. Recently, the parallel imaging concept has also been applied to spectroscopic imaging using the SENSE method [78, 79] and the GRAPPA method [80, 81]. Because both conventional 3D imaging and 2D CSI share the same two dimensional phase encoding k-space, the considerations regarding 2D CAIPIRINHA which have been made in the previous chapter can be directly transferred to 2D CSI. However, in 3D CSI, a third phase encoding direction is available, in which reduction and / or modifications of the sampling patterns can be performed. Thus, at a given reduction factor, similar to 2D CAIPIRINHA, a 3D CAIPIRINHA sampling pattern can be found which exploits potential sensitivity variations in all three dimensions most efficiently. In order to investigate the properties of 3D CAIPIRINHA in 3D
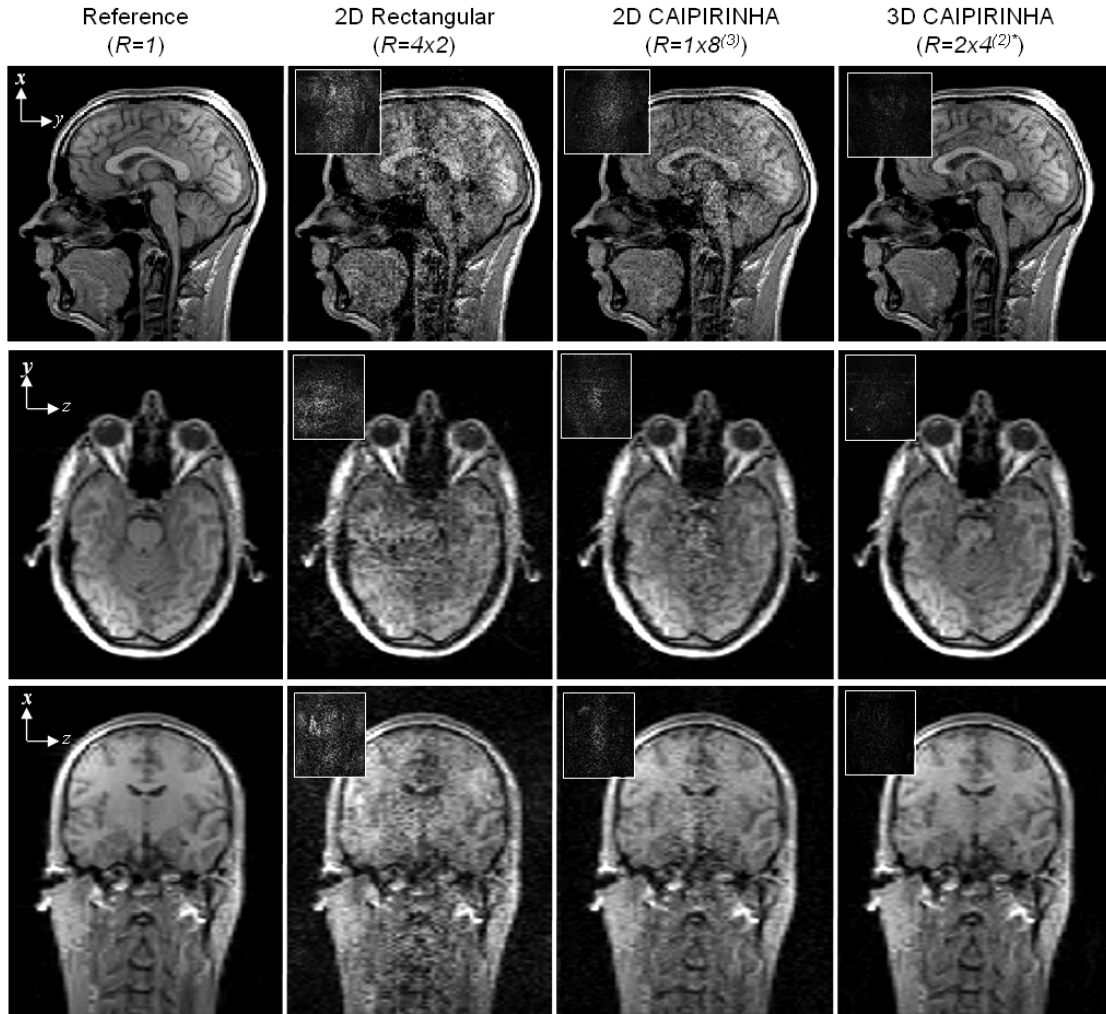
Figure 6.3: Sagittal (top row), transversal (middle row) and coronal (bottom row) view of various $R = 8$-fold accelerated volumetric parallel imaging experiments after 3D GRAPPA reconstruction using different sampling strategies. As a reference, the unaccelerated corresponding images are shown (left column). The reconstruction results after optimal 2D rectangular undersampling ($R = 4 \times 2$), optimal 2D CAIPIRINHA-type sampling ($R = 1 \times 8^{(3)}$), and as a proof of principle one (not the optimal) 3D CAIPIRINHA-type sampling pattern $\left(R = 2 \times 4^{(2)}\right)^{*}$ generated by a zig-zag read-out trajectory are compared. The star indicates that in this case the 2D CAIPIRINHA pattern $R = 2 \times 4^{(2)}$ was additionally shifted by Δk_y in the y-direction and Δk_z in the z-direction for every second read-out sample. In order to demonstrate reconstruction performance, the difference between the reconstructed and the reference image are shown in the left corner for each image.
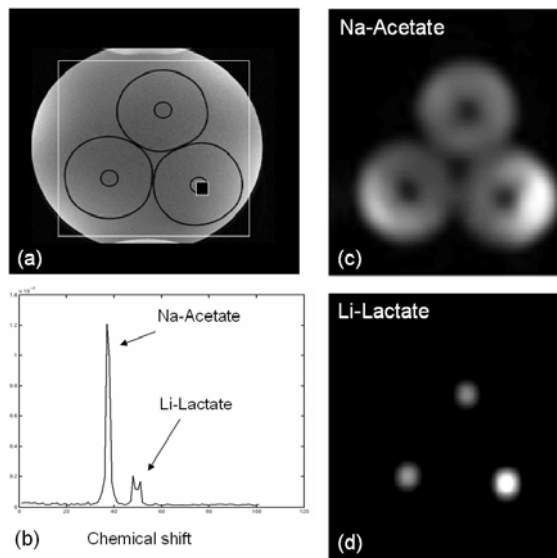
Figure 6.4: (a) Proton image of the phantom (details see text). Unaccelerated reference CSI images are shown for both (c) Na-Acetate and (d) Li-Lactate. The CSI images were generated by calculating the integral over the SOS-combined Li-Lactate and Na-Acetate peaks. (b) Example spectra taken from a partial volume voxel containing both substances.

CSI, a phantom made up of three poly-ethylene bottles of $500\,ml$ volume each was built. The bottles were filled with aqueous Na-acetate ($C_2H_3O_2Na$) solution of $9.6\,g/l$ concentration. A small tube of $1\,cm$ diameter, containing aqueous Li-Lactate ($C_3H_5O_3Li$) solution of $8.2\,g/l$ concentration, was positioned in the center of each bottle. To avoid field inhomogeneities caused by susceptibility-jumps at the bottle-air interface, the bottles were placed in a $NaCl$ solution.

A fully encoded 3D CSI experiment was performed using the phantom on a $1.5\,T$ clinical whole body scanner (Avanto, Siemens Medical Solutions, Erlangen, Germany). For signal reception, a 12 channel two-ring head coil was used. The sequence parameters of the 3D spin-echo CSI experiment were as follows: $TR = 1070\,ms$, $TE = 135\,ms$, matrix $= 16 \times 16 \times 12$, $FOV = 200 \times 175 \times 120\,mm^3$. In the spectroscopic dimension, 1024 data points were acquired at a dwelltime of $312\,\mu s$ corresponding to $3.2\,$kHz acquisition bandwidth. In Fig. 6.4 the middle section of the anatomical 3D MRI phantom experiment is shown including the excitation volume of the CSI experiment (indicated by the big box). In addition, the unaccelerated reference CSI images are shown for both Li-Lactate and Na-Acetate. The CSI images were generated by calculating the integral over the SOS-combined Li-Lactate and Na-Acetate peaks. Besides, as a reference, one example spectra is shown, taken from a partial volume voxel containing both substances (indicated by the small box).

Starting from this fully encoded data set, unwanted phase encoding steps were removed from their sampling positions in order to create 2D rectangular, 2D CAIPIRINHA and 3D CAIPIRINHA-type sampling schemes. Reconstruction weights required for the final GRAPPA reconstruction were derived from an 8x8x8 ACS data block in the center of the 3D k-space. However, an additionally acquired fully-encoded, low-resolution fast 3D FLASH pre-scan experiment could have been used as well [34] as reference data.

In order to demonstrate the benefit of the 3D CAIPIRINHA approach, GRAPPA reconstructions after various accelerated ($R = 6$) 3D CSI experiments using different sampling strategies were performed. In Fig. 6.5 the accelerated CSI images are shown in one partition for both Li-Lactate and Na-Acetate after GRAPPA reconstruction of (b) a conventional rectangular $R = 2 \times 3$ (c) 2D CAIPIRINHA $R = 2 \times 3^{(1)}$ and (d) 3D CAIPIRINHA-type reduction. Additionally, the corresponding unaccelerated ($R = 1$) CSI images are displayed as reference.
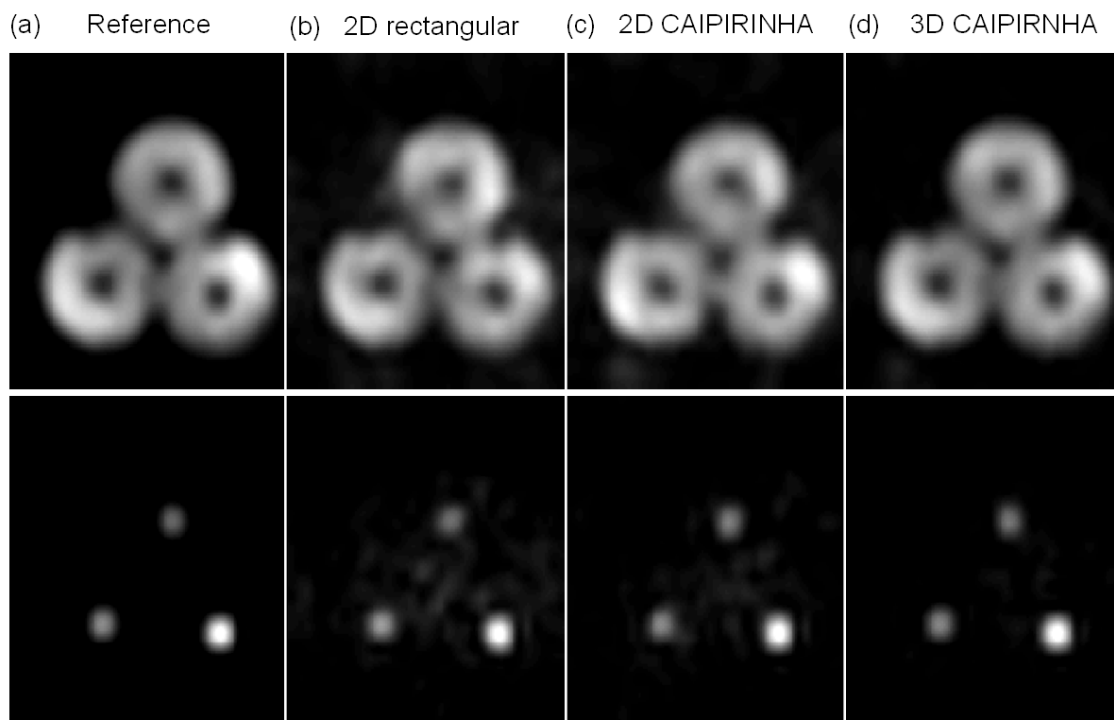

Figure 6.5: Na-Acetate (top row) and Li-Lactate (bottom row) CSI maps after (a) unaccelerated acquisition, six-fold (b) optimal rectangular $R = 2 \times 3$, (c) optimal 2D CAIPIRINHA-type $R = 2 \times 3^{(1)}$ and (d) 3D CAIPIRINHA -type reductions. The CSI images were generated by taking the integral over the SOS-combined Li-Lactate and Na-Acetate spectra after GRAPPA reconstruction.

Furthermore, in Fig. 6.6 example spectra taken from a partial volume voxel, providing peaks for both substances are displayed for each case. Although all three sampling strategies result in reasonable reconstruction quality after GRAPPA, the 3D CAIPIRINHA experiment provides both better spectral and image quality due to lower geometry related noise enhancement and less residual artifacts. Again the images in Fig. 6.5 demonstrate that 2D CAIPIRINHA performs better than 2D rectangular type acquisitions.
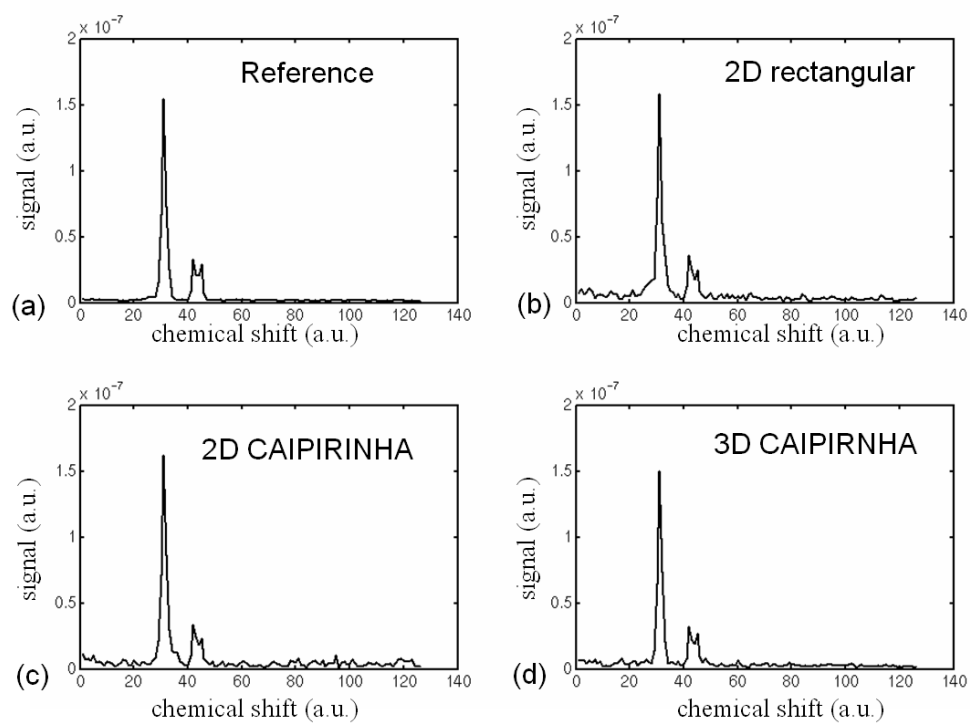
Figure 6.6: Na-Acetate and Li-Lactate spectra taken from a partial volume voxel after (a) unaccelerated acquisition ($R = 1$), six-fold (b) rectangular $R = 2 \times 3$, (c) 2D CAIPIRINHA-type $R = 2 \times 3^{(1)}$and (d) 3D CAIPIRINHA -type reductions.

6.4   Discussion and Conclusion

In this chapter, zig-zag sampling which enables a more efficient exploitation of the sensitivity variations provided by the underlying receiver coil array in the imaging plane (volume) has been described. Thus, sensitivity variations can be exploited in two (compared to one) spatial dimensions in conventional single-slice imaging and in all three dimensions (compared to two) in volumetric parallel imaging. A successful parallel imaging reconstruction process strongly depends on accurate sensitivity variations, especially at high acceleration rates. Therefore, this strategy results in significantly improved reconstruction performance, thereby allowing for higher image acceleration. Unfortunately, no real zig-zag trajectories were acquired, because even in modern scanners with adequate gradient performance it is difficult to generate such sampling trajectories.

However, the simulation results presented here indicate the great benefit of this approach. The zig-zag type sampled experiments shown here share the same number of excitations (phase encoding steps) and read-out samples as the conventional imaging strategy using a straight read-out trajectory and therefore would have the same SNR without parallel imaging. It is clear that in practice, this type of zig-zag sampling requires fast gradient switching times even for sequences with moderate acquisition bandwidths which limits application. However, in previous work, such zig-zag read-out trajectories have already been implemented on modern scanners equipped with accurate gradient systems.

Furthermore, a more straight-forward application of the 3D CAIPIRINHA approach has been presented, namely 3D parallel spectroscopic chemical shift imaging (CSI), which is not limited to low acquisition bandwidths. Because the frequency response without gradients is used to obtain the spectral information in CSI, all spatial dimensions need to be phase encoded. Thus, in accelerated 3D CSI undersampling can be performed in three phase encoding directions. In addition to 2D CAIPIRINHA-type patterns this allows one to modify sampling positions in one further phase encoding direction in 3D k-space in such a way that an optimal utilization of the available sensitivity variations is achieved. However, the intrinsic low SNR in *in vivo* CSI limits the concept to moderate acceleration rates.

Chapter 7

Conclusions and Perspectives

In general, the parallel imaging concept can be applied whenever a receiver coil array is available whose spatial sensitivity distribution allows one to partially accomplish spatial encoding, which normally is performed by applying magnetic field gradients. During the last three years, the major manufacturers, namely Philips, Siemens, GE, and Toshiba, have implemented the parallel imaging feature in their latest scanner generation. Thus, parallel imaging has now become standard procedure and has grown to have a broad clinical impact. However, although the basic parallel imaging framework is well-established, parallel imaging is still subject to steady developments and is expected to have a bright future in MRI. Besides recently held international workshops on parallel MRI [82, 83] a series of review articles has been published, which demonstrate the increasing impact of parallel MRI and summarize the most prominent fields of parallel MRI in clinical applications [84, 85, 86, 87, 88, 89, 90, 91, 92, 93].

In the course of this work, various strategies for efficient parallel imaging were introduced. Based on existing parallel acquisition and reconstruction strategies, such as SENSE and GRAPPA, new concepts have been developed and transferred to potential clinical applications.

Specifically, temporal GRAPPA (TGRAPPA) [43], an efficient method well-suited for dynamic real-time imaging, was presented. TGRAPPA exploits a time-interleaved acquisition scheme which allows one to derive the sensitivity information needed for the parallel imaging reconstruction process directly from the undersampled time series itself. Thus, no additional data must be acquired as normally required for parallel imaging reconstructions, thereby providing optimal image acceleration. Additionally, TGRAPPA provides a frame-to-frame update of the reconstruction parameters, thereby efficiently tracking relative changes of the coil position caused by patient motion. This is particularly relevant for applications with flexible coil arrays, such as cardiac imaging. The TGRAPPA method has been successfully applied to accelerated (reduction factor two to four) real-time (non-gated) free-breathing cardiac studies. Using TGRAPPA, frame rates of up to 30 *fps* have been achieved providing acceptable spatial resolution and image quality. It has also been shown that the concept of partial Fourier

acquisition can be additionally applied in order to further increase the frame rate or spatial resolution. This gain in imaging speed, and the intrinsically high SNR as well as higher acceleration rates achievable in volumetric parallel imaging could potentially be used to make 3D real-time imaging feasible.

The main focus in this work was on CAIPIRINHA (Controlled Aliasing In Parallel Imaging Results IN Higher Acceleration), a novel parallel imaging strategy. CAIPIRINHA can be seen as a new acquisition concept which results in a more robust and improved parallel imaging reconstruction procedure compared to previous proposed strategies. Generally, an accelerated parallel acquisition is associated with aliasing artifacts in the image domain, which normally can be removed by specialized parallel imaging reconstruction methods, such as SENSE or GRAPPA. The basic idea of CAIPIRINHA is to modify the appearance of aliasing in a controlled manner in order to exploit the sensitivity variations provided by the receiver coil array most efficiently, which directly results in improved parallel imaging reconstruction conditions. This leads to a more reliable and robust parallel image reconstruction and significantly reduces the dependence on the coil geometry. In principle, the flexibility of CAIPIRINHA allows one to use any existing parallel imaging reconstruction algorithm, such as SENSE or GRAPPA, to arrive at the final image. However, both algorithms had been limited to rectangular reductions and therefore had to be extended to match the modified aliasing conditions (eg modified acquisition schemes) in CAIPIRINHA. To this end, SENSE and GRAPPA reconstruction algorithms have been developed for single-slice, multi-slice, 2D, and 3D CAIPIRINHA-type experiments for both conventional and spectroscopic imaging (CSI).

During the last three years the CAIPIRINHA concept has been successfully applied to simultaneous multi-slice (MS CAIPIRINHA) [52] and volumetric parallel imaging (2D CAIPIRINHA) [51]. Both techniques have been shown to improve image quality in clinically relevant applications. 2D CAIPIRINHA, in particular, does not demand additional hardware requirements and can therefore be directly employed in any existing application where volumetric parallel imaging is already established. MS CAIPIRINHA, however, requires excitation with special multi-band rf pulses and therefore is limited to applications which do not operate at the SAR (specific absorption rate) limit. However, compared to sequential multi-slice experiments, MS CAIPIRINHA benefits from the SNR gain due to simultaneous slice excitation and therefore, in principle, provides a simultaneous acquisition of multiple slices in the same scan time as required for one single slice with the same basic SNR. However, the SNR is also affected by a coil-geometry-related noise enhancement. In the worst case of no coil sensitivity variations in the slice direction, the geometry-related noise enhancement is equal to that in sequential single-slice parallel imaging. Thus, MS CAIPIRINHA allows, for example, accelerated multi-slice cardiac CINE imaging without significant loss in SNR. Contrast-enhanced heart perfusion will also benefit from this approach, because the contrast agent uptake can be followed in multiple slices simultaneously. The properties of both MS and 2D CAIPIRINHA

have been extensively investigated using computer simulations, phantom studies, and *in vivo* experiments. Both methods are currently implemented in SIEMENS scanners and will probably be available in the next software release. For this reason, CAIPIRINHA is expected to be employed in clinical practice in the near future.

In addition, as a proof of principle, a further strategy has been introduced which extends the concept of CAIPIRINHA to an additional spatial dimension. In conventional parallel MRI, potential sensitivity variations available in the read-direction have not been employed in the parallel imaging reconstruction process. In this work, it has been shown that by replacing the straight read-out line in conventional imaging with a zig-zag sampled trajectory, sensitivity variations in the read-direction can be exploited, thereby achieving significantly improved parallel image reconstruction performance in both single-slice and volumetric parallel imaging (3D CAIPIRINHA).

Although the main focus in this work was parallel MRI, it has been shown that the concept of CAIPIRINHA is also applicable to spectroscopic parallel imaging (CSI). 2D CAIPIRINHA for volumetric parallel MRI can directly be transferred to 2D CSI, because both methods share the same number of phase encoding directions to which 2D CAIPIRINHA sampling patterns can be employed. The additional phase encoding direction in 3D CSI provides a further degree of freedom for distributing the sampling positions in three phase encoding directions in such a way that optimized reconstruction performance is obtained at a given reduction factor.

In connection with the modified acquisition schemes in CAIPIRINHA, adapted GRAPPA algorithms have been developed. The novel GRAPPA algorithms presented here directly solve for the missing points in 2D, 3D, or even 4D (CSI) k-space and therefore work for both rectangular and CAIPIRINHA-type acquisitions. So far, GRAPPA has been limited to reductions performed only in one phase encoding direction. For volumetric parallel imaging either a GRAPPA-SENSE hybrid [94] was required or GRAPPA had to be applied in two subsequent reconstruction steps in each phase encoding direction seperately [95, 96]. However, both reconstruction strategies have been shown to provide suboptimal reconstruction performance compared to the algorithms presented in this work.

Perspectives

The latest scanners provide up to 32 independent receiver channels and coil arrays with 16 elements are already in clinical use. Currently, 32 element coils for head and abdomen applications are in clinical test stage. Further advances have been made at various research sites. For example, Wiggins *et al.* presented a prototype volume head-array with 90 elements which allows for high acceleration factors [97]. McDougall *et al.* introduced a linear array with 64 elements which has been used to spatially encode an entire image with only one echo [98]. Although hampered by significant problems in hardware development due to coil-to-coil

coupling through magnetic and electrical fields, further advances in the development of arrays with even more coils are expected. In general, it is anticipated that all PPA methods will benefit from arrays with a large number of element coils.

This trend towards large coil arrays has led to a new field in parallel imaging, namely massive parallel MRI. In massive parallel MRI, the receiver coil array should perform, in the extreme case, all the spatial encoding normally achieved by employing time-consuming phase encoding gradients. However, it is clear that parallel imaging is not without its limitations. Even in the case of large multi-coil arrays, the maximum achievable acceleration in many clinical applications is restricted to $R = 4$ in 2D and $R = 8$ in 3D MRI, because of the SNR loss associated with the PPA concept.

Besides the development of dedicated large coil arrays, a major topic at many research sites is the combination of the parallel imaging concept with non-Cartesian sampling strategies, such as radial or spiral imaging. In many cases a radial or spiral sampling of k-space is beneficial compared to conventional Cartesian sampling. Additionally, non-Cartesian sampling strategies intrinsically exploit sensitivity variations in multiple dimensions and therefore have the potential to allow for higher reduction factors. Recently, iterative SENSE reconstruction algorithms [99] and advanced GRAPPA algorithms [100, 101, 102, 103, 104, 105] for non-Cartesian trajectories have been introduced. However, these methods require advanced regridding algorithms and suffer from sub-optimal reconstruction performance and/or long reconstruction times, and therefore are not yet established in clinical practice.

In general, further improvements in the existing reconstruction algorithms in terms of reconstruction times and image quality are expected. Additionally, combinations of various parallel imaging strategies with each other or with other efficient non-parallel imaging strategies will be a driving force in the growing field of parallel MRI.

Bibliography

[1] F Bloch, WW Hansen, and M Packard. Nuclear induction. *Physical Review*, 69(3-4):127 – 127, 1946.

[2] EM Purcell, HC Torrey, and RV Pound. Resonance absorption by nuclear magnetic moments in a solid. *Physical Review*, 69(1-2):37 – 38, 1946.

[3] J Pauly, D Nishimura, and A Macovski. A k-space analysis of small-tip-angle excitation. *J Magn Reson*, 81(1):43 – 56, 1989.

[4] D B Twieg. The k-trajectory formulation of the NMR imaging process with applications in analysis and synthesis of imaging methods. *Med Phys*, 10(5):610–21, 1983.

[5] E M Haacke, R W Brown, M R Thompson, and R Venkatesan. *Magnetic Resonance Imaging, Physical Principles and Sequence Design*. A John Wiley and Sons, 1999.

[6] WA Edelstein, JMS Hutchison, G Johnson, and T Redpath. Spin warp NMR imaging and applications to human whole-body imaging. *Physics in Medicine and Biology*, 25(4):751 – 756, 1980.

[7] C H Meyer, B S Hu, D G Nishimura, and A Macovski. Fast spiral coronary artery imaging. *Magn Reson Med*, 28(2):202–13, 1992.

[8] G H Glover and J M Pauly. Projection reconstruction techniques for reduction of motion effects in MRI. *Magn Reson Med*, 28(2):275–89, 1992.

[9] A Haase, J Frahm, D Matthaei, W Hanicke, and K D Merboldt. Flash imaging - rapid nmr imaging using low flip-angle pulses. *J Magn Reson*, 67(2):258 – 266, 1986.

[10] P Mansfield. Multi-planar image-formation using nmr spin echoes. *Journal of Physics C-Solid State Physics*, 10(3):L55 – L58, 1977.

[11] J Hennig, A Nauerth, and H Friedburg. RARE imaging: a fast imaging method for clinical MR. *Magn Reson Med*, 3(6):823–33, 1986.

[12] P B Roemer, W A Edelstein, C E Hayes, S P Souza, and O M Mueller. The NMR phased array. *Magn Reson Med*, 16(2):192–225, 1990.

[13] D O Walsh, A F Gmitro, and M W Marcellin. Adaptive reconstruction of phased array MR imagery. *Magn Reson Med*, 43(5):682–90, 2000.

[14] M A Griswold, P M Jakob, Q Chen, J W Goldfarb, W J Manning, R R Edelman, and D K Sodickson. Resolution enhancement in single-shot imaging using simultaneous acquisition of spatial harmonics (SMASH). *Magn Reson Med*, 41(6):1236–45, 1999.

[15] R M Heidemann, M A Griswold, B Kiefer, M Nittka, J Wang, V Jellus, and P M Jakob. Resolution enhancement in lung 1H imaging using parallel imaging methods. *Magn Reson Med*, 49(2):391–4, 2003.

[16] Florian Wiesinger, Peter Boesiger, and Klaas P Pruessmann. Electrodynamics and ultimate SNR in parallel MR imaging. *Magn Reson Med*, 52(2):376–90, 2004.

[17] Michael A Ohliger, Aaron K Grant, and Daniel K Sodickson. Ultimate intrinsic signal-to-noise ratio for parallel MRI: electromagnetic field considerations. *Magn Reson Med*, 50(5):1018–30, 2003.

[18] J Kelton, R M Magin, and S M Wright. An algorithm for rapid image acquisition using multiple receiver coils. In *Proceedings of the 8th SMRM Annual Meeting, Amsterdam, The Netherlands*, 1989. Page 1172.

[19] J B Ra and C Y Rim. Fast imaging using subencoding data sets from multiple detectors. *Magn Reson Med*, 30(1):142–5, 1993.

[20] J W Carlson and T Minemura. Imaging time reduction through multiple receiver coil data acquisition and image reconstruction. *Magn Reson Med*, 29(5):681–7, 1993.

[21] D K Sodickson and W J Manning. Simultaneous acquisition of spatial harmonics (SMASH): fast imaging with radiofrequency coil arrays. *Magn Reson Med*, 38(4):591–603, 1997.

[22] D K Sodickson, M A Griswold, R R Edelman, and W J Manning. Accelerated spin echo and gradient echo imaging in the abdomen and thorax using simultaneous acquisition of spatial harmonics (SMASH). In *Proceedings of the ISMRM Annual Meeting, Vancouver, Canada*, 1997. Abstract 1818.

[23] K P Pruessmann, M Weiger, M B Scheidegger, and P Boesiger. SENSE: sensitivity encoding for fast MRI. *Magn Reson Med*, 42(5):952–62, 1999.

[24] Mark Bydder, David J Larkman, and Joseph V Hajnal. Generalized SMASH imaging. *Magn Reson Med*, 47(1):160–70, 2002.

[25] P M Jakob, M A Griswold, R R Edelman, and D K Sodickson. AUTO-SMASH: a self-calibrating technique for SMASH imaging. SiMultaneous Acquisition of Spatial Harmonics. *MAGMA*, 7(1):42–54, 1998.

[26] R M Heidemann, M A Griswold, A Haase, and P M Jakob. VD-AUTO-SMASH imaging. *Magn Reson Med*, 45(6):1066–74, 2001.

[27] Mark A Griswold, Peter M Jakob, Robin M Heidemann, Mathias Nittka, Vladimir Jellus, Jianmin Wang, Berthold Kiefer, and Axel Haase. Generalized autocalibrating partially parallel acquisitions (GRAPPA). *Magn Reson Med*, 47(6):1202–10, 2002.

[28] W E Kyriakos, L P Panych, D F Kacher, C F Westin, S M Bao, R V Mulkern, and F A Jolesz. Sensitivity profiles from an array of coils for encoding and reconstruction in parallel (SPACE RIP). *Magn Reson Med*, 44(2):301–8, 2000.

[29] J Wang, T Kluge, M Nittka, V Jellus, B Kühn, and B Kiefer. Parallel Acquisition Techniques with modified SENSE reconstruction mSENSE. In *First international Workshop on parallel MRI, Würzburg, Germany*, 2001. page 398.

[30] M A Griswold, P M Jakob, M Nittka, J W Goldfarb, and A Haase. Partially parallel imaging with localized sensitivities (PILS). *Magn Reson Med*, 44(4):602–9, 2000.

[31] Gilbert Strang. *Linear algebra and its applications*. Harcourt Brace and Company, 1988.

[32] Jacco A de Zwart, Peter van Gelderen, Peter Kellman, and Jeff H Duyn. Application of sensitivity-encoded echo-planar imaging for blood oxygen level-dependent functional brain imaging. *Magn Reson Med*, 48(6):1011–20, 2002.

[33] M Bydder, D J Larkman, and J V Hajnal. Combination of signals from array coils using image-based estimation of coil sensitivity profiles. *Magn Reson Med*, 47(3):539–48, 2002.

[34] F Breuer, M Blaimer, M Mueller, R M Heidemann, M A Griswold, and P M Jakob. Autocalibrated parallel imaging with GRAPPA using a single prescan as reference data. In *Proceedings of the ESMRMB Annual Meeting, Kopenhagen, Denmark*, 2004. Abstract 398.

[35] J Wang, B Zhang, K Zhong, and Y Zhuo. Image Domain Based Fast GRAPPA Reconstruction and relative SNR degradation Factor. In *Proceedings of the ISMRM Annual Meeting, Miami, Florida, USA*, 2005. Abstract 2428.

[36] M A Griswold. Advanced k-space Techniques. In *Second international Workshop on parallel MRI, Zurich, Switzerland*, 2004. page 16.

[37] D J Atkinson and R R Edelman. Cineangiography of the heart in a single breath hold with a segmented turboflash sequence. *Radiology*, 178(2):357–60, 1991.

[38] D R Elgort, E Y Wong, C M Hillenbrand, F K Wacker, J S Lewin, and J L Duerk. Real-time catheter tracking and adaptive imaging. *J Magn Reson Imaging*, 18(5):621–6, 2003.

[39] Jeffrey Tsao, Peter Boesiger, and Klaas P Pruessmann. k-t BLAST and k-t SENSE: dynamic MRI with high frame rate exploiting spatiotemporal correlations. *Magn Reson Med*, 50(5):1031–42, 2003.

[40] Feng Huang, James Akao, Sathya Vijayakumar, George R Duensing, and Mark Limkeman. k-t GRAPPA: a k-space implementation for dynamic MRI with high reduction factor. *Magn Reson Med*, 54(5):1172–84, 2005.

[41] B Madore, G H Glover, and N J Pelc. Unaliasing by fourier-encoding the overlaps using the temporal dimension (UNFOLD), applied to cardiac imaging and fMRI. *Magn Reson Med*, 42(5):813–28, 1999.

[42] P Kellman, F H Epstein, and E R McVeigh. Adaptive sensitivity encoding incorporating temporal filtering (TSENSE). *Magn Reson Med*, 45(5):846–52, 2001.

[43] Felix A Breuer, Peter Kellman, Mark A Griswold, and Peter M Jakob. Dynamic autocalibrated parallel imaging using temporal GRAPPA (TGRAPPA). *Magn Reson Med*, 53(4):981–5, 2005.

[44] Mark Bydder and Matthew D Robson. Partial fourier partially parallel imaging. *Magn Reson Med*, 53(6):1393–401, 2005.

[45] E M Haacke, E D Lindskogj, and W Lin. A fast, iterative, partial-fourier technique capable of local phase recovery. *J Magn Reson*, 92(1):126–45, 1991.

[46] Michael A Guttman, Peter Kellman, Alexander J Dick, Robert J Lederman, and Elliot R McVeigh. Real-time accelerated interactive MRI with adaptive TSENSE and UNFOLD. *Magn Reson Med*, 50(2):315–21, 2003.

[47] Markus Weiger, Klaas P Pruessmann, and Peter Boesiger. 2D SENSE for faster 3D MRI. *MAGMA*, 14(1):10–9, 2002.

[48] D J Larkman, J V Hajnal, A H Herlihy, G A Coutts, I R Young, and G Ehnholm. Use of multicoil arrays for separation of signal from multiple slices simultaneously excited. *J Magn Reson Imaging*, 13(2):313–7, 2001.

[49] Datenacquisitionsverfahren zur beschleunigten Magnet-Resonanz-Bildgebung im Rahmen der parallelen Akquisition von MRT-Daten. Offenlegungsschrift, Deutsches Patent- und Markenamt, November 2004. DE 103 18 682 A1.

[50] Data acquisition method for accelerated magnetic resonance imaging in framework of the parallel acquisition of MRT data. Patent Application Publication, United States, November 2004. US 2004/0222794.

[51] Felix A Breuer, Martin Blaimer, Robin M Heidemann, Matthias F Mueller, Mark A Griswold, and Peter M Jakob. Controlled aliasing in parallel imaging results in higher acceleration (CAIPIRINHA) for multi-slice imaging. *Magn Reson Med*, 53(3):684–91, 2005.

[52] Felix A Breuer, Martin Blaimer, Matthias F Mueller, Nicole Seiberlich, Robin M Heidemann, Mark A Griswold, and Peter M Jakob. Controlled aliasing in volumetric parallel imaging (2d CAIPIRINHA). *Magn Reson Med*, 2006. Epub ahead of print.

[53] G H Glover. Phase-offset multiplanar (POMP) volume imaging: a new technique. *J Magn Reson Imaging*, 1(4):457–61, 1991.

[54] S Muller. Simultaneous multislice imaging (SIMUSIM) for improved cardiac imaging. *Magn Reson Med*, 10(1):145–55, 1989.

[55] S Muller. Multislice snapshot FLASH using SIMUSIM. *Magn Reson Med*, 15(3):497–500, 1990.

[56] S P Souza, J Szumowski, C L Dumoulin, D P Plewes, and G Glover. SIMA: simultaneous multislice acquisition of MR images by Hadamard-encoded excitation. *J Comput Assist Tomogr*, 12(6):1026–30, 1988.

[57] C H Cunningham and M L Wood. Method for improved multiband excitation profiles using the Shinnar-Le Roux transform. *Magn Reson Med*, 42(3):577–84, 1999.

[58] M Blaimer, F Breuer, M Mueller, R M Heidemann, M A Griswold, and P M Jakob. Multi-slice cardiac MRI using Controlled Aliasing In Parallel Imaging Results IN Higher Acceleration (CAIPIRINHA). In *Proceedings of the ESMRMB Annual Meeting, Rotterdam, Netherlands*, 2003. Abstract 109.

[59] C Bretschneider, F Breuer, M Blaimer, P Schmitt, M Mueller, M A Griswold, and P M Jakob. CAIPIRINHA-TrueFisp for accelerated multi-slice parallel imaging. In *Proceedings of the ESMRMB Annual Meeting, Kopenhagen, Denmark*, 2004. Abstract 272.

[60] F Breuer, M Blaimer, M Mueller, R M Heidemann, M A Griswold, and P M Jakob. Controlled Aliasing In Parallel Imaging Results IN Higher Acceleration (CAIPIRINHA). In *Proceedings of the ESMRMB Annual Meeting, Rotterdam, Netherlands*, 2003. Abstract 40.

[61] F Breuer, M Blaimer, M Mueller, R M Heidemann, M A Griswold, and P M Jakob. Controlled Aliasing In 3D Parallel Imaging (2D CAIPIRINHA). In *Proceedings of the ISMRM Annual Meeting, Kyoto, Japan*, 2004. Abstract 326.

[62] M Jurrissen, M Fuderer, and J van den Brink. Diamond-SENSE: undersampling on a crystographic grid. In *Proceedings of the ISMRM Annual Meeting, Kyoto,Japan*, 2004. Abstract 2643.

[63] J Tsao, S Kozerke, M S Hansen, P Boesiger, and K P Pruessmann. Optimized canonical sampling patterns in k-t space with two and three spatial dimensions for k-t BLAST and k-t SENSE. In *Proceedings of the ISMRM Annual Meeting, Kyoto,Japan*, 2004. Abstract 326.

[64] Jeffrey Tsao, Sebastian Kozerke, Peter Boesiger, and Klaas P Pruessmann. Optimizing spatiotemporal sampling for k-t BLAST and k-t SENSE: application to high-resolution real-time cardiac steady-state free precession. *Magn Reson Med*, 53(6):1372–82, 2005.

[65] N P Willis and Y Bresler. Optimal scan design for time varying tomographic imaging II: Efficient design and experimental validation. *IEEE Trans. Image Processing*, 4:654–666, 1995.

[66] F A Breuer, M Blaimer, N Seiberlich, M A Griswold, and P M Jakob. A 3D GRAPPA algorithm for volumetric parallel imaging. In *Proceedings of the ISMRM Annual Meeting, Seattle, Washington, USA*, 2006. accepted.

[67] N M Rofsky, V S Lee, G Laub, M A Pollack, G A Krinsky, D Thomasson, M M Ambrosino, and J C Weinreb. Abdominal MR imaging with a volumetric interpolated breath-hold examination. *Radiology*, 212(3):876–84, 1999.

[68] M Dobritz, T Radkow, M Nittka, W Bautz, and F A Fellner. VIBE with parallel acquisition technique - a novel approach to dynamic contrast-enhanced MR imaging of the liver. *Rofo*, 174(6):738–41, 2002.

[69] Mark A Griswold, Stephan Kannengiesser, Robin M Heidemann, Jianmin Wang, and Peter M Jakob. Field-of-view limitations in parallel imaging. *Magn Reson Med*, 52(5):1118–26, 2004.

[70] F A Breuer, M Blaimer, M F Mueller, R M Heidemann, M A Griswold, and P M Jakob. Finding the Optimal Sampling Pattern in 2D Parallel Imaging for a Given Receiver Coil Configuration. In *Proceedings of the ISMRM Annual Meeting, Miami, Florida, USA*, 2005. Abstract 2665.

[71] F A Breuer, M Blaimer, M F Mueller, R M Heidemann, M A Griswold, and P M Jakob. The Use of Principal Component Analysis (PCA) for Estimation of the Maximum

Reduction Factor in 2D Parallel Imaging. In *Proceedings of the ISMRM Annual Meeting, Miami, Florida, USA*, 2005. Abstract 2668.

[72] F A Breuer, M Blaimer, N Seiberlich, M A Griswold, and P M Jakob. The use of coil sensitivity variations in the read-direction for improved parallel imaging. In *Proceedings of the ISMRM Annual Meeting, Seattle, Washington, USA*, 2006. accepted.

[73] K Oshio. vGRASE: separating phase and T(2) modulations in 2D. *Magn Reson Med*, 44(3):383–6, 2000.

[74] H Moriguchi, J L Sunshine, and J L Duerk. Detailed description of Bunched Phase Encoding. In *Proceedings of the RSNA Annual Meeting, Chicago, Illinois, USA*, 2004.

[75] H Moriguchi, J L Sunshine, and J L Duerk. Further Scan Time Reduction of Bunched Phase Encoding Using Sensitivity Encoding. In *Proceedings of ISMRM Annual Meeting, Miami, Florida, USA*, 2005. Abstract 287.

[76] A Papoulis. Generalized sampling expansion. *IEEE Transactions on circuit and systems*, 24(11):652–4, 1977.

[77] D N Guilfoyle and P Mansfield. Chemical-shift imaging. *Magn Reson Med*, 2(5):479–89, 1985.

[78] U Dydak, M Weiger, K P Pruessmann, D Meier, and P Boesiger. Sensitivity-encoded spectroscopic imaging. *Magn Reson Med*, 46(4):713–22, 2001.

[79] Ulrike Dydak, Klaas P Pruessmann, Markus Weiger, Jeffrey Tsao, Dieter Meier, and Peter Boesiger. Parallel spectroscopic imaging with spin-echo trains. *Magn Reson Med*, 50(1):196–200, 2003.

[80] F A Breuer, D Ebel, M Blaimer, J Ruff, N Seiberlich, M A Griswold, and P M Jakob. Parallel 2D and 3D spectroscopic imaging using GRAPPA. In *Proceedings of the ISMRM Annual Meeting, Seattle, Washington, USA*, 2006. accepted.

[81] Dieter Ebel. Parallele spektroskopische NMR-Bildgebung, 2005.

[82] *First international Workshop on parallel MRI, Würzburg, Germany*, 2001.

[83] *Second international Workshop on parallel MRI, Zurich, Switzerland*, 2004.

[84] David J Larkman, David Atkinson, and Jo V Hajnal. Artifact reduction using parallel imaging methods. *Top Magn Reson Imaging*, 15(4):267–75, 2004.

[85] Michael Augustin, Franz Fazekas, and Roland Bammer. Fast patient workup in acute stroke using parallel imaging. *Top Magn Reson Imaging*, 15(3):207–19, 2004.

[86] Roland Bammer. Parallel Imaging: (Part II). *Top Magn Reson Imaging*, 15(4):221, 2004.

[87] Martin Blaimer, Felix Breuer, Matthias Mueller, Robin M Heidemann, Mark A Griswold, and Peter M Jakob. SMASH, SENSE, PILS, GRAPPA: how to choose the optimal method. *Top Magn Reson Imaging*, 15(4):223–36, 2004.

[88] Taylor Chung and Raja Muthupillai. Application of SENSE in clinical pediatric body MR imaging. *Top Magn Reson Imaging*, 15(3):187–96, 2004.

[89] Xavier Golay, Jacco A de Zwart, Yi-Ching Lynn Ho, and Yih-Yian Sitoh. Parallel imaging techniques in functional MRI. *Top Magn Reson Imaging*, 15(4):255–65, 2004.

[90] Daniel Jason Aaron Margolis, Roland Bammer, and Lawrence C Chow. Parallel imaging of the abdomen. *Top Magn Reson Imaging*, 15(3):197–206, 2004.

[91] Klaas P Pruessmann. Parallel imaging at high field strength: synergies and joint potential. *Top Magn Reson Imaging*, 15(4):237–44, 2004.

[92] Rudolf Stollberger and Franz Fazekas. Improved perfusion and tracer kinetic imaging using parallel imaging. *Top Magn Reson Imaging*, 15(4):245–54, 2004.

[93] Sebastian Kozerke and Jeffrey Tsao. Reduced data acquisition methods in cardiac imaging. *Top Magn Reson Imaging*, 15(3):161–8, 2004.

[94] M Blaimer, F A Breuer, M Müller, R Heidemann, M A Griswold, and P M Jakob. Schnelle Volumenbildgebung mit einem SENSE / GRAPPA Hybrid. In *Proceedings of the 6th DS ISMRM Annual Meeting, Heidelberg, Germany*, page 51, 2003.

[95] Martin Blaimer. *Selbstkalibrierende Verfahren in der parallelen Magnetresonanztomographie*. PhD thesis, University of Würzburg, 2006.

[96] M Blaimer, F A Breuer, M F Mueller, R M Heidemann, M A Griswold, and P M Jakob. The 2D-GRAPPA-Operator for 3D MRI. In *Proceedings of the ISMRM Annual Meeting, Miami, Florida, USA*, 2005. Abstract 2673.

[97] G C Wiggins, A Potthast, C Triantafylllou, F Lin, T Benner, C J Wiggins, and L Wald. A 96-channel MRI System with23- and 90-channel Phased Array Head Coils at 1.5 Tesla. In *Proceedings of ISMRM Annual Meeting, Miami, Florida, USA*, 2005. Abstract 671.

[98] Mary Preston McDougall and Steven M Wright. 64-channel array coil for single echo acquisition magnetic resonance imaging. *Magn Reson Med*, 54(2):386–92, 2005.

[99] K P Pruessmann, M Weiger, P Bornert, and P Boesiger. Advances in sensitivity encoding with arbitrary k-space trajectories. *Magn Reson Med*, 46(4):638–51, 2001.

[100] K A Heberlein and X Hu. Fast Self-Calibrated Parallel Imaging using Dual-Density Spirals. In *Proceedings of ISMRM Annual Meeting, Miami, Florida, USA*, 2005. Abstract 2425.

[101] K A Heberlein, Y Kadah, and X Hu. Segmented Spiral Parallel Imaging using GRAPPA. In *Proceedings of ISMRM Annual Meeting, Kyoto, Japan*, 2004. Abstract 328.

[102] R M Heidemann, M A Griswold, G Krueger, S Kannengiesser, B Kiefer, and P M Jakob. Fast Parallel Image Reconstruction for Spiral Trajectories. In *Second international Workshop on parallel MRI, Zurich, Switzerland*, 2004. page 27.

[103] M A Griswold, R M Heidemann, and P M Jakob. Direct parallel imaging reconstruction of radially sampled data using GRAPPA with relative shifts. In *Proceedings of ISMRM Annual Meeting, Toronta, Canada*, 2003. Abstract 2349.

[104] N Seiberlich, R Heidemann, F A Breuer, M Blaimer, M A Griswold, and P M Jakob. Pseudo-Cartesian GRAPPA Reconstruction of Undersampled Non-Cartesian Data. In *Proceedings of the ISMRM Annual Meeting, Seattle, Washington, USA*, 2006. accepted.

[105] N Seiberlich, F A Breuer, M Blaimer, P Speier, M A Griswold, and P M Jakob. 3D Cylindrical GRAPPA. In *Proceedings of the ISMRM Annual Meeting, Seattle, Washington, USA*, 2006. accepted.

Summary

Virtually all existing MRI applications require both a high spatial and high temporal resolution for optimum detection and classification of the state of disease. The main strategy to meet the increasing demands of advanced diagnostic imaging applications has been the steady improvement of gradient systems, which provide increased gradient strengths and faster switching times. Rapid imaging techniques and the advances in gradient performance have significantly reduced acquisition times from about an hour to several minutes or seconds. In order to further increase imaging speed, much higher gradient strengths and much faster switching times are required which are technically challenging to provide. In addition to significant hardware costs, peripheral neuro-stimulations and the surpassing of admissable acoustic noise levels may occur. Today's whole body gradient systems already operate just below the allowed safety levels. For these reasons, alternative strategies are needed to bypass these limitations. The greatest progress in further increasing imaging speed has been the development of multi-coil arrays and the advent of partially parallel acquisition (PPA) techniques in the late 1990's.

Within the last years, parallel imaging methods have become commercially available, and are therefore ready for broad clinical use. The basic feature of parallel imaging is a scan time reduction, applicable to nearly any available MRI method, while maintaining the contrast behavior without requiring higher gradient system performance. PPA operates by allowing an array of receiver surface coils, positioned around the object under investigation, to partially replace time-consuming spatial encoding which normally is performed by switching magnetic field gradients. Using this strategy, spatial resolution can be improved given a specific imaging time, or scan times can be reduced at a given spatial resolution. Furthermore, in some cases, PPA can even be used to reduce image artifacts. Unfortunately, parallel imaging is associated with a loss in signal-to-noise ratio (SNR) and therefore is limited to applications which do not already operate at the SNR limit. An additional limitation is the fact that the coil array must provide sufficient sensitivity variations throughout the object under investigation in order to offer enough spatial encoding capacity.

This doctoral thesis exhibits an overview of my research on the topic of efficient parallel imaging strategies. Based on existing parallel acquisition and reconstruction strategies, such as SENSE and GRAPPA, new concepts have been developed and transferred to potential clinical applications.

Specifically, temporal GRAPPA (TGRAPPA), an efficient method well-suited for dynamic real-time imaging, has been presented. TGRAPPA exploits a time-interleaved acquisition scheme which allows one to derive the sensitivity information needed for the parallel imaging reconstruction process directly from the undersampled time series itself. Thus, no additional data must be acquired as normally required for parallel imaging reconstructions, thereby providing optimal image acceleration. Additionally, TGRAPPA provides a frame-to-frame update of the reconstruction parameters, thereby efficiently tracking relative changes of the coil position caused by patient motion. This is particularly relevant for applications with flexible coil arrays, such as cardiac imaging. The TGRAPPA method has been successfully applied to accelerated (reduction factor two to four) real-time (non-gated) free-breathing cardiac studies. Using TGRAPPA, frame rates of up to 30 *fps* have been achieved providing acceptable spatial resolution and image quality. It has also been shown that the concept of partial Fourier acquisition can be additionally applied in order to further increase the frame rate or spatial resolution. This gain in imaging speed, and the intrinsically high SNR as well as higher acceleration rates achievable in volumetric parallel imaging could potentially be used to make 3D real-time imaging feasible.

The main focus in this work was on CAIPIRINHA (Controlled Aliasing In Parallel Imaging Results IN Higher Acceleration), a novel parallel imaging strategy. CAIPIRINHA can be seen as a new acquisition concept which results in a more robust and improved parallel imaging reconstruction procedure compared to previous proposed strategies. Generally, an accelerated parallel acquisition is associated with aliasing artifacts in the image domain, which normally can be removed by specialized parallel imaging reconstruction methods, such as SENSE or GRAPPA. The basic idea of CAIPIRINHA is to modify the appearance of aliasing in a controlled manner in order to exploit the sensitivity variations provided by the receiver coil array most efficiently, which directly results in improved parallel imaging reconstruction conditions. This leads to a more reliable and robust parallel image reconstruction and significantly reduces the dependence on the coil geometry. In principle, the flexibility of CAIPIRINHA allows one to use any existing parallel imaging reconstruction algorithm, such as SENSE or GRAPPA, to arrive at the final image. However, both algorithms had been limited to rectangular reductions and therefore had to be extended to match the modified aliasing conditions (eg modified acquisition schemes) in CAIPIRINHA. To this end, SENSE and GRAPPA reconstruction algorithms have been developed for single-slice, multi-slice, 2D, and 3D CAIPIRINHA-type experiments for both conventional and spectroscopic imaging (CSI).

During the last three years the CAIPIRINHA concept has been successfully applied to simultaneous multi-slice (MS CAIPIRINHA) and volumetric parallel imaging (2D CAIPIRINHA). Both techniques have been shown to improve image quality in clinically relevant applications. 2D CAIPIRINHA, in particular, does not demand additional hardware requirements and can therefore be directly employed in any existing application where volumetric

parallel imaging is already established. MS CAIPIRINHA, however, requires excitation with special multi-band rf pulses and therefore is limited to applications which do not operate at the SAR (specific absorption rate) limit. However, compared to sequential multi-slice experiments, MS CAIPIRINHA benefits from the SNR gain due to simultaneous slice excitation and therefore, in principle, provides a simultaneous acquisition of multiple slices in the same scan time as required for one single slice with the same basic SNR. However, the SNR is also affected by a coil-geometry-related noise enhancement. In the worst case of no coil sensitivity variations in the slice direction, the geometry-related noise enhancement is equal to that in sequential single-slice parallel imaging. The properties of both MS and 2D CAIPIRINHA have been extensively investigated using computer simulations, phantom studies, and *in vivo* experiments. Both methods are currently implemented in SIEMENS scanners and will probably be available in the next software release. For this reason, CAIPIRINHA is expected to be employed in clinical practice in the near future.

In addition, as a proof of principle, a further strategy has been introduced which extends the concept of CAIPIRINHA to an additional spatial dimension. All previously proposed parallel imaging strategies could not employ sensitivity variations potentially available in the read-direction in the reconstruction process. In this work, a novel approach has been presented, which for the first time allows for exploitation of sensitivity variations in the read direction, thereby providing significantly improved parallel image reconstruction performance in both single-slice and volumetric parallel imaging (3D CAIPIRINHA). This is done by replacing the straight read-out line in conventional imaging with a zig-zag sampled trajectory.

Although the main focus in this work was parallel MRI, it has been shown that the concept of CAIPIRINHA is also applicable to spectroscopic parallel imaging (CSI). 2D CAIPIRINHA for volumetric parallel MRI can directly be transferred to 2D CSI, because both methods share the same number of phase encoding directions to which 2D CAIPIRINHA sampling patterns can be employed. The additional phase encoding direction in 3D CSI provides a further degree of freedom for distributing the sampling positions in three phase encoding directions in such a way that optimized reconstruction performance is obtained at a given reduction factor.

Zusammenfassung

In den späten 80er Jahren entwickelte sich die Magnetresonanz-Tomographie (MRT), die bis dato lediglich in Forschungseinrichtungen etabliert war, zu einem der wichtigsten Verfahren in der klinischen Diagnostik. Allerdings erfordern nahezu alle bestehenden klinischen Anwendungsgebiete sowohl eine hohe räumliche als auch eine hohe zeitliche Auflösung für eine optimale Detektion und Klassifizierung von Krankheitsbildern. Der bisherige Ansatz, diesen zunehmenden Anforderungen an die klinische MRT gerecht zu werden, bestand vor allem in der stetigen Verbesserung von Gradientensystemen die mit immer höheren Gradientenstärken und schnelleren Schaltzeiten aufwarteten. Die technischen Fortschritte, sowie schnelle Bildgebungsmethoden erlaubten es, Messzeiten von etwa einer Stunde auf nur wenige Minuten oder sogar Sekunden zu reduzieren. Eine weitere Verkürzung der Experimentdauer mittels noch leistungsfähigeren Gradientensystemen ist jedoch technisch schwierig zu realisieren. Ausserdem gehen enorm hohe Entwicklungs und Materialkosten mit den erhöhten Anforderungen einher. Es kommt hinzu, dass noch stärkere Gradienten und noch schnellere Schaltzeiten zu peripheren Neurostimulationen und zur Überschreitung von zulässigen akustischen Grenzwerten führen können. Heutige Gradientensysteme arbeiten schon sehr nahe an den Grenzen der zulässigen Sicherheitsbestimmungen. Deshalb werden alternative Strategien benötigt, um weitere Messzeitverkürzungen realisieren zu können. Der bisher erfolgreichste Ansatz bestand in der Entwicklung von Mehr-Kanal-Spulen-Anordnungen und damit verknüpft der darauffolgenden Einführung der parallellen Bildgebung in den späten 90er Jahren.

In den letzten 5 Jahren haben sich parallele Bildgebungsmethoden an den klinischen Tomographen etabliert und nahezu alle Herstellerfirmen stellen diese Technik kommerziell zur Verfügung. Die parallele Bildgebung ermöglicht eine Messzeitverkürzung, die prinzipiell auf jede bestehende Bildgebungsmethode angewendet werden kann, ohne dabei das Kontrastverhalten zu verändern und ohne höhere Gradientenleistung zu beanspruchen. In der parallellen Bildgebung übernimmt die Mehr-Kanal-Spulen-Anordnung teilwiese die Ortskodierung, die normalerweise durch zeitaufwendiges Schalten von Magnetfelgradienten erzeugt wird. Mit dieser Strategie kann bei gleicher Messzeit die örtliche Auflösung verbessert, oder bei gleicher Auflösung die Messzeit verkürzt werden. Ausserdem können mit hilfe der parallelen MRT in manchen Fällen Bildartefakte signifikant reduziert werden. Allerdings ist mit der parallelen Bildgebung immer ein Signal zu Rausch (SNR) Verlust verbunden, der diese Methode auf kli-

nische Anwendungen begrenzt, die nicht bereits am SNR-Limit betrieben werden. Ausserdem muß die Spulenanordnung genug Sensitivitätsvariationen über das zu untersuchende Objekt bereitstellen, um ausreichende Kodierfunktion zu gewährleisten.

Diese Dissertationsarbeit liefert einen Überblick über meine Forschungsarbeit zum Thema "Entwicklung und Anwendung von effizienten Strategien in der parallelen MRT". Basierend auf bestehenden parallelen Akquisitions und Rekonstruktionstechniken, wie beispielsweise SENSE und GRAPPA, wurden neue Konzepte entwickelt und auf mögliche klinische Fragestellungen angewandt.

Im speziellen wurde temporal GRAPPA (TGRAPPA) vorgestellt, eine Technik, die sich hervorragend für effiziente dynamische Echtzeit-Bildgebung eignet. TGRAPPA verwendet ein zeitlich versetztes Akquisitionsschema, welches es ermöglicht die Spulensensitivitätsinformation, die für die parallele Bildrekonstruktion benötigt wird, direkt aus einer Zeitserie von reduzierten Datensätzen zu gewinnen. Hierdurch wird eine optimale Bildbeschleunigung erzielt, da keine zusätzlichen Referenzdaten zur Sensitivitätsbestimmung akquiriert werden müssen. Ausserdem ermöglicht TGRAPPA eine kontinuierliche Aktualisierung der Spuleninformation, was dazu führt, dass Änderungen der Sensitivitätsinformationen, beispielseise durch Bewegung, sehr effizient abgefangen werden können. Dies ist besonders relevant für Anwendungen, bei denen flexible Spulenanordnungen verwendet werden, wie es beispielsweise bei der dynamischen Herzbildgebung der Fall ist. TGRAPPA wurde erfolgreich am schlagenden menschlichen Herzen bei freier Atmung eingesetzt, wobei bis zu vierfache Bildbeschleunigung erzielt werden konnte. Mit dieser Technik wurden, bei akzeptabler räumlicher Auflösung und Bildqualität, Bildraten von bis zu 30 Bildern pro Sekunde erreicht. Es wurde ausserdem gezeigt, dass ein weiterer Messzeitgewinn möglich ist, wenn TGRAPPA mit der sogenanten partial-Fourier Technik kombiniert wird. Diese zusätzliche Beschleunigung, sowie das intrinsisch hohe SNR und die verbesserten Kodiereigenschaften in der parallelen Volumenbildgebung, könnten dazu beitragen, dynamische 3D Echtzeit-Bildgebung am menschlichen Herzen zu realisieren.

Der Fokus dieser Arbeit lag darin, das Konzept der kontrollierten Einfaltungen, CAIPIRINHA (engl. *Controlled Aliasing In Parallel Imaging Results IN Higher Acceleration*) in der parallelen MRT zu untersuchen und zu etablieren. CAIPIRINHA kann als neue Akquisitionsstrategie betrachtet werden, die, verglichen mit bestehenden Konzepten, eine robustere und bessere parallele Bildrekonstruktion ermöglicht. Eine beschleunigte parallele Datenaufnahme ist generell mit Einfaltungsartefakten im Bild verbunden, die durch spezielle parallele Bildgebungs-Rekonstruktionsverfahren wie SENSE oder GRAPPA beseitigt werden können. Die grundlegende Idee von CAIPIRINHA besteht darin, diese Einfaltungsartefakte gezielt zu verändern, so dass Sensitivitätsvariationen, die die verwendete Spulenanordnung bereit stellt, möglichst effizient genutzt werden, was direkt eine robustere und verbesserte parallele Bildrekonstruktion zur Folge hat, wobei die Abhängigkeit der Rekonstruktion von den Gegebenheiten der geometrischen Spulenanordnung signifikant reduziert wird. Zusätzlich erlaubt es die Fle-

xibilität von CAIPIRINHA, jegliche bestehende parallele Bildgebungstechnik, wie zB. SENSE oder GRAPPA zur Bildrekonstruktion heranzuziehen. Beide Techniken waren bisher jedoch auf konventionell reduzierte Datensätze beschränkt und mussten deshalb an die CAIPIRINHA typischen, veränderten Einfaltungsbedingungen (veränderte Datenakquisition) angepasst werden.

In den letzten drei Jahren konnte das CAIPIRINHA-Konzept erfolgreich in der parallelen simultanen Mehrschicht- (MS CAIPIRINHA) und Volumenbildgebung (2D CAIPIRINHA) eingesetzt werden. Es konnte mit beiden Techniken die Bildqualität in klinisch relevanten Fragestellungen verbessert werden. 2D CAIPIRINHA hat den Vorzug, dass keine speziellen zusätzlichen Anforderungen an das System gestellt werden und kann deshalb direkt in den klinischen Gebieten eingesetzt werden, in denen die parallele Volumenbildgebung bereits etabliert ist. MS CAIPIRINHA allerdings benötigt spezielle Multischicht-Anregungspulse und ist deshalb auf Anwendungen beschränkt, die nicht bereits an der Grenze der zulässigen spezifischen Absorbtionsrate (SAR) betrieben werden. Verglichen mit sequentiellen Mehrschichtexperimenten profitiert MS CAIPIRINHA vom SNR-Gewinn mehrerer gleichzeitig angeregter Schichten und erlaubt deshalb prinzipiell, mehrere Schichten in der gleichen Zeit und mit gleichem SNR aufzunehmen, wie normalerweise für eine Schicht benötigt wird. Allerdings wird durch die parallele Bildrekonstruktion eine zusätzliche, von der Spulengeometrie abhängige Rauscherhöhung erzeugt. Im Extremfall von nur äusserst wenig Sensitivitätsvariationen in Schichtrichtung sind die geometrieabhängigen Rauscherhöhungen identisch mit denen in beschleunigten sequentiellen Akquisitionen. Die Eigenschaften von MS und 2D CAIPIRINHA wurden mittels Simulationen, Phantom und *in vivo* Experimenten ausgiebig untersucht. Beide Methoden werden momentan in den neuen SIEMENS Tomographen implementiert und werden deshalb vorraussichtlich schon bald in vielen klinischen Fragestellungen eingesetzt werden.

Weiterhin wurde erstmals eine Strategie beschrieben, die das CAIPIRINHA Konzept auf eine weitere räumliche Dimension erweitert. In der konventionellen parallelen Bildgebung konnten mögliche Sensitivitätsvariationen in der Lese-Richtung bisher nicht zur Bildrekonstruktion genutzt werden. In dieser Arbeit wurde gezeigt, dass durch Ersetzen der üblichen geraden Lesetrajektorie mit einer Zick-Zack-Trajektorie Sensitivitätsvariationen in Leserichtung zusätzlich im parallelen Rekonstruktionsprozess verwendet werden können, was zur deutlich verbesserten Bildqualität in Einzelschicht und auch in Volumenexperimenten (3D CAIPIRINHA) führte. Die Verbesserten Rekonstruktionsbedingungen können auch dazu genutzt werden noch höhere Bildbeschleunugung zu erzielen.

Obgleich der Hauptaugenmerk dieser Arbeit auf der konventionellen parallelen Bildgebung lag, wurde in Auszügen gezeigt, dass sich das CAIPIRINHA-Konzept entsprechend auf die spektroskopische Bildgebung (CSI) anwenden lässt. So konnte beispielsweise 2D CAIPIRINHA für die parallele Volumenbildgebung "eins zu eins" auf beschleunigte 2D CSI Experimente übertragen werden, da beide Methoden die gleiche Anzahl von Phasenkodierrichtungen auf-

weisen auf welche 2D CAIPIRINHA - Akquisitionsmuster angewendet werden können. Die zusätzliche Phasenkodierrichtung in 3D CSI ermöglicht es, CAIPIRINHA -typische Akquisitionsmuster in eine dritte Dimension zu erweitern, so dass optimale Bedingungen für die parallele Datenrekonstruktion bei einem vorgegebenen Reduktionsfaktor gewährleistet sind.

Publications

Papers:

Griswold MA, Blaimer M, **Breuer F**, Heidemann RM, Mueller M, Jakob PM. Parallel magnetic resonance imaging using the GRAPPA operator formalism. *Magn Reson Med.* 2005 Oct 27.

Breuer FA, Kellman P, Griswold MA, Jakob PM. Dynamic autocalibrated parallel imaging using temporal GRAPPA (TGRAPPA). *Magn Reson Med.* 2005 Apr;53(4):981-5.

Breuer FA, Blaimer M, Heidemann RM, Mueller MF, Griswold MA, Jakob PM. Controlled aliasing in parallel imaging results in higher acceleration (CAIPIRINHA) for multi-slice imaging. *Magn Reson Med.* 2005 Mar;53(3):684-91.

Breuer FA, Blaimer M, Mueller MF , Seiberlich N, Heidemann RM, Griswold MA, Jakob PM. Controlled aliasing in volumetric parallel imaging (2D CAIPIRINHA). *Magn Reson Med.* 2006 Jan; 11; [Epub, ahead of print]

Blaimer M, **Breuer FA**, Seiberlich N, Mueller MF, Heidemann RM, Jellus V, Wiggins G, Wald LL, Griswold MA, Jakob PM. Accelerated Volumetric MRI with a SENSE/GRAPPA-Combination. *J Magn Reson Imaging* 2006 [in process]

Blaimer M, **Breuer FA**, Seiberlich N, D. Ebel, Heidemann RM, Griswold MA, Jakob PM. A comparison of k-space domain parallel imaging approaches for faster 3D MRI. *Magn Reson Med* 2006 [in process]

Review Articles:

Heidemann RM, Ozsarlak O, Parizel PM, Michiels J, Kiefer B, Jellus V, Muller M, **Breuer F**, Blaimer M, Griswold M, Jakob PM A brief review of parallel magnetic resonance imaging. *Eur Radiol.* 2003 Oct;13(10):2323-37. Epub 2003 Aug 27. Review.

Blaimer M, **Breuer F**, Mueller M, Heidemann RM, Griswold MA, Jakob PM. SMASH SENSE, PILS, GRAPPA: how to choose the optimal method. *Top Magn Reson Imaging.* 2004 Aug;15(4):223-36.

Heidemann RM, Griswold MA, Muller M, **Breuer F**, Blaimer M, Kiefer B, Schmitt M, Jakob PM. Feasibilities and limitations of high field parallel MRI. *Radiologe.* 2004 Jan;44(1):49-55. Germany.

Abstracts:

Blaimer M, **Breuer F**, Müller M, Griswold M, Jakob P. Verfahren der Parallelen Datenakquisition und Bildrekonstruktionen in der MRT. *In Proceedings, DS ISMRM 2002, 5th annual meeting, Hamburg, Germany.*

F. Breuer, M. Blaimer, M. Müller, R. Heidemann, M. Griswold, P. Jakob Controlled aliasing in parallel imaging (CAIPI) applied to multi-slice imaging. *In Proceedings, ISMRM 2003, 11th annual meeting, #18, Toronto, Ontario, Canada.*

F. Breuer, P. Kellman, M. Griswold, P. Jakob Dynamic Autocalibrated Parallel Imaging using TGRAPPA. *In Proceedings, ISMRM 2003, 11th annual meeting, #2330, Toronto, Ontario, Canada.*

F. Breuer, M. Blaimer, M. Müller, R. Heidemann, M. Griswold, P. Jakob Controlled aliasing in parallel imaging results in higher acceleration (CAIPIRINHA). *In Proceedings, ESMRMB 2003, 20th annual meeting, #42, Rotterdam, Netherlands.*

F. Breuer, P. Kellman, M. Blaimer, M. Müller, R. Heidemann, M. Griswold, P. Jakob Dynamische "Echtzeitbildgebung" am menschlichen Herzen mittels TGRAPPA. *In Proceedings, DS ISMRM 2003, 6th annual meeting, Heidelberg, Germany.*

F. Breuer, M. Blaimer, M. Müller, R. Heidemann, M. Griswold, P. Jakob Kontrollierte Einfaltungen in der parallelen Bildgebung (CAIPIRINHA). *In Proceedings, DS ISMRM 2003, 6th annual meeting, Heidelberg, Germany.*

Blaimer M, **Breuer F**, Müller M, Heidemann RM, Griswold MA, Jakob PM. Schnelle Volumenbildgebung mit einem SENSE / GRAPPA Hybrid. *In Proceedings, DS ISMRM 2003, 6th annual meeting, Heidelberg, Germany.*

Blaimer M, **Breuer F**, Heidemann RM, Mueller M, Griswold MA, Jakob PM. Is parallel MRI without a priori information possible? *In Proceedings, ISMRM 2004, 12th Scientific Meeting, # 2417, Kyoto, Japan.*

Breuer F, Blaimer M, Mueller M, Heidemann RM, Griswold MA, Jakob PM. Controlled Aliasing in 3D Parallel Imaging (2D CAIPIRINHA). *In Proceedings, ISMRM 2004, 12th Scientific Meeting, # 326, Kyoto, Japan.*

Griswold MA, Blaimer M, Heidemann RM, Speier P, Kannengeisser S, Nittka M, **Breuer F**, Mueller M, Jakob PM. Rapid Evaluation of Cardiac Function Using Undersampled Radial TrueFISP with GRAPPA. *In Proceedings, ISMRM 2004, 12th Scientific Meeting, # 637, Kyoto, Japan.*

Mueller M, Lanz T, Blaimer M, **Breuer F**, Heidemann R, Webb A, Griswold M, Jakob P. Considerations for Enhanced SNR Performance of a Spiral Array Coil with Many Elements using a Common End Ring Design. *In Proceedings, ISMRM 2004, 12th Scientific Meeting, # 1592, Kyoto, Japan.*

Mueller M, **Breuer F**, Blaimer M, Heidemann R, Webb A, Griswold M, Jakob P. 8 Channel Double Spiral Head Array Coil for Enhanced 3D Parallel MRI at 1.5T. *In Proceedings, ISMRM 2004, 12th Scientific Meeting, # 2391, Kyoto, Japan.*

F. Breuer, M. Blaimer, M. Müller, R. Heidemann, M. Griswold, P. Jakob Autocalibrated parallel imaging with GRAPPA using a single prescan as reference data. *In Proceedings, ESMRMB 2004, 21th annual meeting, #398, Copenhagen, Denmark.*

M. Blaimer, **F. Breuer**, M. Müller, R. Heidemann, M. Griswold, P. Jakob Parallel MRI without apriori information using the GRAPPA-Operator formalism and correlation statistics. *In Proceedings, ESMRMB 2004, 21th annual meeting, #273, Copenhagen, Denmark.*

C. Bretschneider, **F. Breuer**, M. Blaimer, P. Schmitt, M. Müller, M. Griswold, P. Jakob CAIPIRINH-TrueFISP for accelerated multi-slice parallel imaging. *In Proceedings, ESMRMB 2004, 21th annual meeting, #272, Copenhagen, Denmark.*

M. Müller, **F. Breuer**, M. Blaimer, R. Heidemann, M. Griswold, P. Jakob Considerations for a Double Spiral 16 Channel Routine Head Array Coil With a Common End Ring for Enhanced 3D Parallel Imaging at 1.5T. *In Proceedings, ESMRMB 2004, 21th annual meeting, #275, Copenhagen, Denmark.*

Blaimer M, **Breuer F**, Mueller M, Heidemann RM, Griswold MA, Jakob PM. On the GRAPPA-Operator. *Second International Workshop on Parallel MRI, Zürich, Schweiz; 2004: # 26.*

Mueller M, **Breuer F**, Blaimer M, Heidemann R, Webb A, Griswold M, Jakob P. Promising Double Spiral Design for Volume Array Head Coils. Second International Workshop on Parallel MRI, Zürich, Schweiz; 2004: # 39.

Breuer FA, Blaimer M, Mueller MF, Heidemann RM, Griswold MA, Jakob PM. Controlled Aliasing In Parallel Imaging. *Second International Workshop on Parallel, MRI, Zürich, Schweiz; 2004: # 54.*

M. Blaimer, **F. Breuer**, M. Mueller, R. M. Heidemann, M. A. Griswold, P. M. Jakob The 2D-GRAPPA-Operator for 3D MRI. *In Proceedings, ISMRM 2005, 13th Scientific Meeting, # 2673, Miami Beach, Florida, USA.*

F. A. Breuer, M. Blaimer, M. F. Mueller, R. M. Heidemann, M. A. Griswold, P. M. Jakob Finding the optimal sampling pattern in 2D parallel imaging for a given receiver coil configuration. *In Proceedings, ISMRM 2005, 13th Scientific Meeting, # 2665, Miami Beach, Florida, USA.*

F. A. Breuer, M. Blaimer, M. F. Mueller, R. M. Heidemann, M. A. Griswold, P. M. Jakob. The use of principal component analysis (PCA) for estimation of the maximum reduction factor in 2D parallel imaging. *In Proceedings, ISMRM 2005, 13th Scientific Meeting, # 2668, Miami Beach, Florida, USA.*

F. A. Breuer, M. Blaimer, N. Seiberlich, M. A. Griswold, P. M. Jakob. 3D GRAPPA Algorithm for Volumetric Parallel Imaging. *In Proceedings, ISMRM 2006, 14th Scientific Meeting, Seattle, Washington, USA.* [accepted]

F. A. Breuer, M. Blaimer, N. Seiberlich, M. A. Griswold, P. M. Jakob. The Use of Coil Sensitivity Variations in the read-direction for improved Parallel Imaging. *In Proceedings, ISMRM 2006, 14th Scientific Meeting, Seattle, Washington, USA.* [accepted]

F. A. Breuer, D. Ebel, M. Blaimer, J. Ruff, N. Seiberlich, M. A. Griswold, P. M. Jakob. *Parallel 2D and 3D Spectroscopic Imaging using GRAPPA. In Proceedings, ISMRM 2006, 14th Scientific Meeting, Seattle, Washington, USA.* [accepted]

M. Blaimer**,** K. Barkauskas, S. Kannengiesser, **F. A. Breuer**, P. M. Jakob, M. A. Griswold. Artifact Reduction in Undersampled BLADE/PROPELLER MRI by k-Space Extrapolation using Parallel Imaging. *In Proceedings, ISMRM 2006, 14th Scientific Meeting, Seattle, Washington, USA.* [accepted]

N. Seiberlich, **F. A. Breuer**, M. Blaimer, P. Speier , M. A. Griswold, P. M. Jakob. 3D Cylindrical GRAPPA*. In Proceedings, ISMRM 2006, 14th Scientific Meeting, Seattle, Washington, USA.* [accepted]

N. Seiberlich, R. Heidemann, **F. A. Breuer**, M. Blaimer, M. A. Griswold, P. M. Jakob. Pseudo-Cartesian GRAPPA Reconstruction of Undersampled Non-Cartesian Data. *In Proceedings, ISMRM 2006, 14th Scientific Meeting, Seattle, Washington, USA.* [accepted]

D. Gareis, V. C. Behr, **F. Breuer**, M. Griswold, P. Jakob. Multipurpose 4+4 Channel Array Setup for Parallel Imaging in 3D. *In Proceedings, ISMRM 2006, 14th Scientific Meeting, Seattle, Washington, USA.* [accepted]

S. Köhler, P. Ullmann, S. Junge, M. Wick, F. Hennel, **F. Breuer**, P. M. Jakob, W. Ruhm. High-Field Parallel NMR-Microscopy in Small Animals. *In Proceedings, ISMRM 2006, 14th Scientific Meeting, Seattle, Washington, USA.* [accepted]

Acknowledgements

This thesis would not have been possible without the support of many people. In particular, I like to thank

.... **Prof. Dr. Peter M Jakob** who has established Parallel Imaging at the University of Würzburg and has offered me the possibility to do my PhD on a more than interesting topic in his lab. His great interest in my research activities and his many helpful suggestions made him an excellent supervisor.

.... **Prof. Dr. Axel Haase** who has fathered the department and provided an ideal environment for my research.

.... **Prof. Dr. Mark Griswold** who has also supervised my work and always helped with many good ideas. I learned a lot from him and I am looking forward to working together with him in the future.

.... **Dr. Peter Kellman** for providing the TGRAPPA data and for his contribution to the paper.

.... **Martin Blaimer** who accompanied me already during my physic studies and with whom I did a lot of research work together during the last four years. Thank you Martin for your great ideas, helpful discussions and friendship.

.... the **PPA group** consisting of **Robin Heidemann**, **Martin Blaimer**, **Matthias Müller**, **Nicole Seiberlich**, **Daniel Gareis**, **Marcos Lopez**, **David Balla**, **Christian Bretschneider**, and **Dimitri Ebel** for a great team-work.

.... **Siemens Medical Solutions** in Erlangen, in particular **Berthold Kiefer**, **Mathias Nittka**, **Stephan Kannengiesser**, **Vladimir Jellus**, **Jan Ruff** and **Sonia Nielles-Vallespin** for a very productive collaboration.

Curriculum Vitae

Felix Breuer

Home Address:	Keesburgstrasse 9d, 97074 Würzburg, Germany
Date of Birth:	21.08.1975
Place of Birth:	Würzburg, Germany
Nationality:	German

School Education

Sep. 1986 – Jun. 1995   Röntgen Gymnasium, Würzburg, Germany
Degree: Abitur

Undergraduate Education

Oct. 1996 – Nov. 2001   University of Würzburg, Germany
Degree: Master of Science in Physics (Diplom Univ.)

Oct. 2000 – Nov. 2001   Dept. of Experimental Physics 5
Thesis: Non-invasive monitoring of oxygenation
and perfusion changes with MRI

Graduate Education

Dez. 2001 – present   University of Würzburg
Dept. of Experimental Physics 5
Topic: parallel MRI

Würzburg, 16.02.2006

Erklärung